QUANTITATIVE ANALYSIS OF MINERAL/MATRIX TO EVALUATE GENETICALLY ALTERED BONE WITH INFRARED SPECTROSCOPY AND X-RAY SPECTRAL IMAGING

by

SUNIL BALASAHEB YADAV

Presented to the Faculty of the Graduate School of

The University of Texas at Arlington in Partial Fulfillment

of the Requirements

for the Degree of

MASTER OF SCIENCE IN MATERIALS SCIENCE AND ENGINEERING

THE UNIVERSITY OF TEXAS AT ARLINGTON

MAY 2018

Acknowledgments

With great pleasure, I want to thank Dr. Harry Tibbals, Research Professor, whose guidance and support from the beginning through each step of my master's journey was huge and is just not limited to this study.

Dr. Efstathios Meletis's, Chair of MSE Department, channeling us throughout the research was of really great help.

I am grateful to Dr. Jonathan Rios, Scientist, and Mr. Bill Pierce, Chief Engineer, from Texas Scottish Rite Children's Hospital for providing me with the samples and a bone saw.

Dr. Jiechao Jiang, Manager, and Mr. David Yan, Technician, of CCMB LAB, allowed us to use the lab for storing samples and trained me to use different instruments which played a key role in this study.

I extend my gratitude to Dr. Roy McDougald, Senior Scientist in the Chemistry and Biochemistry Department, as he contributed to this study by making his department's FTIR instrument available.

I am also grateful for the help from my colleagues Mr. Meet Shah, Mr. Ninad Khadse and Mr. Shaunak Joshi.

April 13, 2018

Abstract

QUANTITATIVE ANALYSIS OF MINERAL/MATRIX TO EVALUATE
GENETICALLY ALTERED BONE
WITH INFRARED SPECTROSCOPY AND
X-RAY SPECTRAL IMAGING

Sunil Balasaheb Yadav, MS
The University of Texas at Arlington, 2018

Supervising Professor: Harry Fred Tibbals

This thesis focuses on the characterization of bone with the help of Fourier Transform Infrared Spectroscopy and Energy Dispersive Spectroscopy. Such analysis of the physics and chemistry of biomaterials is vital to resolve problems in life science of bone-related diseases and disorders. Material characterization can help in the understanding of disease mechanisms and lead to useful drugs and other treatments. In this thesis, I have used bone materials produced by groundbreaking research at UT Southwestern Research Center and Texas Scottish Rite Children's Hospital to establish that idiopathic clubfoot (Talipes equinovarus) is associated with the Follistatin 5 gene. We studied healthy wild-type laboratory rats in comparison with genetically modified rats, called knock-out type, in which function of the Follistatin 5 gene was controlled with genetic engineering. We were able to identify significant differences in mineral and matrix composition of bone despite considerable variability in the samples. For mid-diaphysis of bone, matrix content was reduced in the knockout compared to the wild-type, leading to the increased mineral to matrix ratio in the knockout.

Table of Contents

List of Illustrations

List of Tables

Chapter 1 Introduction

1.1.1 Bone Diseases and Disorders

In this study, I analyzed normal bone, referred to as wild-type (WT), and abnormal bone, referred to as knock out type (KO). Knock outs have genetically modified tissues in which the function of the Follistatin (fstl) 5 gene is disabled. To examine the modification occurring in the KO, one should have a sound understanding of various components in healthy bone and their distribution. Abnormal distribution can result in disorders such as Talipes Equinovarus (TEV) or clubfoot. University of Texas Arlington, UT Southwestern Research Center (UTSRC), and Texas Scottish Rite Children's Hospital worked in collaboration for this study.

Bone diseases and disorders such as TEV are often related to the change in and function of mineral and matrix compositions. Mineral and matrix disruption in the bone can be metabolic or genetic. Metabolism bone disorders include those associated with abnormalities in minerals (i.e., calcium and phosphorous), collectively called hydroxyapatite. Fourier Transformed Infrared Spectroscopy (FTIR) helps to determine Bone Mineral Density (BMD), which is a useful unit of measurement for mineral and matrix in many diseases. Changes in mineral and matrix composition can also be related to genetic alterations.

Bone and marrow contribute to the same organ in which bone and hematopoietic cells coexist and interact. Marrow and skeletal tissue influence each other, and a variety of genetic disorders directly target both, which may result in combined hematopoietic failure and skeletal malformations [(1)]. For instance, various forms of congenital anemias reduce bone mass and induce osteoporosis, while osteoclast failure in osteoporosis prevents marrow development, mitigating medullary cavities and causing anemia and pancytopenia. Diagnosis and management can be facilitated by understanding the pathophysiology of these conditions [(2)]. These diseases and disorders affect bone formation and resorption.

Despite recent progress, it is still unclear why and how these bone pathologies arise, raising uncertainty regarding optimal treatment. This thesis mainly focuses on how these modifications affect the mineral and matrix quality and quantity.

FTIR is an ideal technique to understand quality and quantity of mineral and matrix, which affect the porosity and fragility of bone. Widely used technologies like Digital X-ray Radiogrammetry, Computed Tomography, and Ultrasound analyze bone parameters. Radiation, cost and space availability drove researchers to utilize new options such as FTIR and Raman Spectroscopy. These analysis methods are nondestructive, quick and do not require sample preparation.

1.1.2 Bone Parameters

Evaluation of bone quality and quantity is completed based on the following parameters [3]:

1. Mineral (Mn) to Matrix ratio (Mx) (=Mn/Mx): Distribution of minerals over matrix contained is a useful measure of bone quality.
2. Mineral Maturity: Morphology of minerals is dependent upon the age of crystal rather than the age of the species.
3. Collagen maturity and collagen crosslinks: Collagen crosslinks provide nucleation site for the crystal growth.

This study focused on the Mineral/Matrix (Mn/Mx) parameter to discriminate between WT and KO. Initially, I examined the composition of bone, which is a function of gene and animal age, as illustrated in Figure 1-1. Thus, gene and animal age are the controlling factors of change in the bone composition.

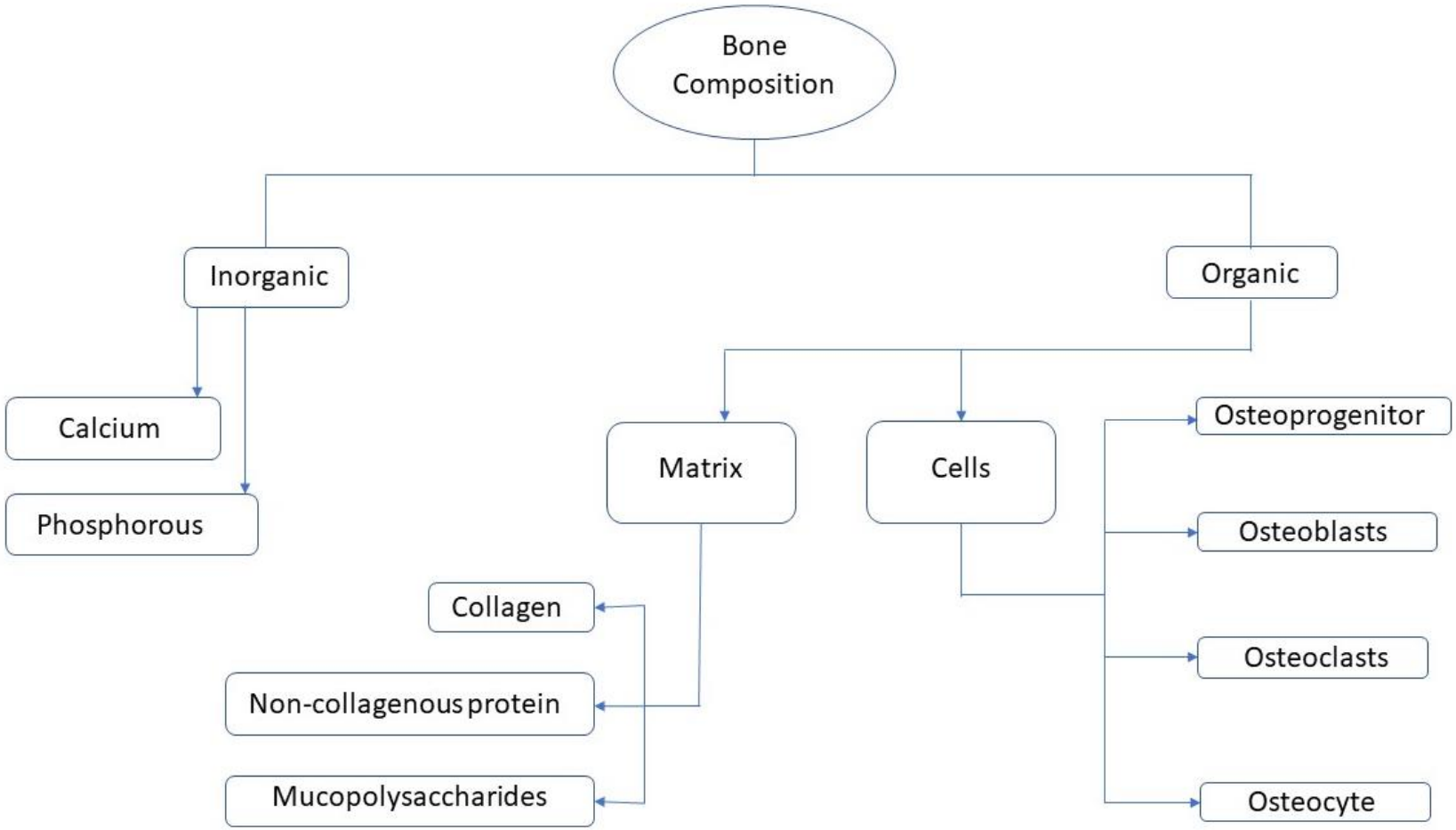

Figure 1-1 Bone composition

Organic constituents are about 30% of the total bone composition, whereas inorganic constituents contribute 60% and the remaining 10% is water. The organic constituents, which are related to the bone formation and tensile strength, are called cells and matrix respectively. The inorganic constituents, which provide the compressive strength of bone, are calcium and phosphorous. These elements are in the form of hydroxyapatite.

Bone composition varies with age and gender. Figure 1-2 depicts the hierarchical structure of bone, which illustrates heterogeneous and anisotropic structure within a bone.

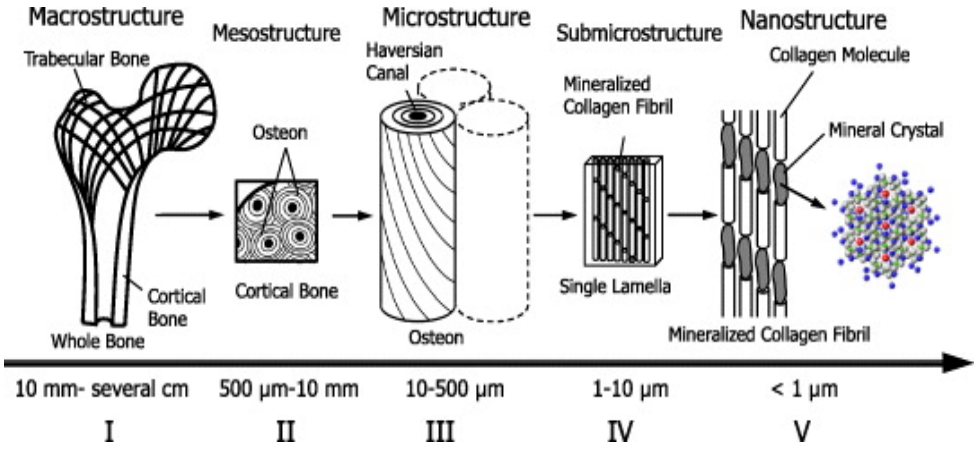

Figure 1-2 Hierarchical structure of bone

Collagen, a matrix, has a triple helix fibril structure, and hydroxyapatites are crystalline in structure. The triple helix structure of collagen fibril provides a nucleation site for the hydroxyapatite crystals. This composite structure of bone works concurrently to provide toughness and strength.

1.2.1 FTIR Bone Characterization Technique

The principle of FTIR includes the interaction of infrared light with molecules. Each molecule has a unique vibration frequency depending upon its bond strength [(4)]. If the resonant frequency of light is incident on a molecule, the molecule would absorb the energy according to the bond strength. The absorbance will help to obtain the spectrum related to the wavelength of light. This absorbance spectrum used in FTIR is more intense than

scattering spectra used in Raman spectroscopy. Also, the reflectance mode in FTIR can make light travel transversely several times resulting in multiple absorptions.

There are two ways to obtain absorbance with FTIR: transmission through sample and reflectance from the sample. Bone is not highly transparent, so I used the reflectance mode. Use of the transmission mode can obtain spectra from the poorly transparent material, but this method requires grinding the sample and mixing it with salt. The transmission mode is not suitable for examining intact microstructure of bone. I was careful to note that many of the spectra reported in the literature are from the transmission mode as distinguished from reflectance spectra that we used here. A typical spectrum of bone is presented in Figure 1-3, which illustrates different peaks associated with different compounds in the bone sample.

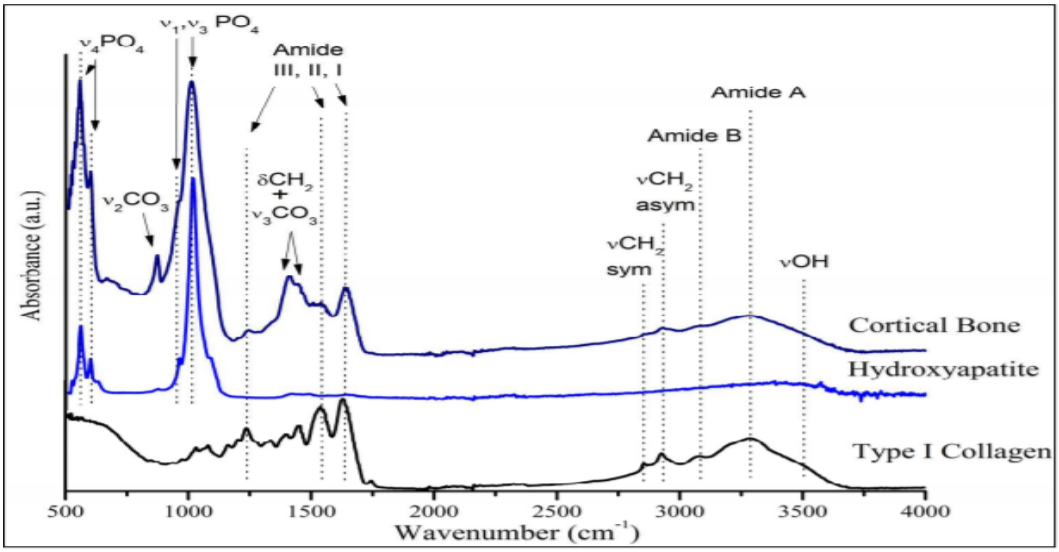

Figure 1-3 Typical FTIR spectrum of bone [3]

The area under a peak is related to the amount of a particular compound. Samples containing proteins show fluorescence in the spectrum. As discussed earlier, I was interested in the phosphate and amide I peak at the wavenumber of 1020 and 1640 cm^{-1}, respectively. [3]

If the incident light frequency matches the natural frequency of a molecule, it will start to vibrate [5]. Infrared (IR) spectroscopy involves a one-photon absorption effect (Figure 1-4).

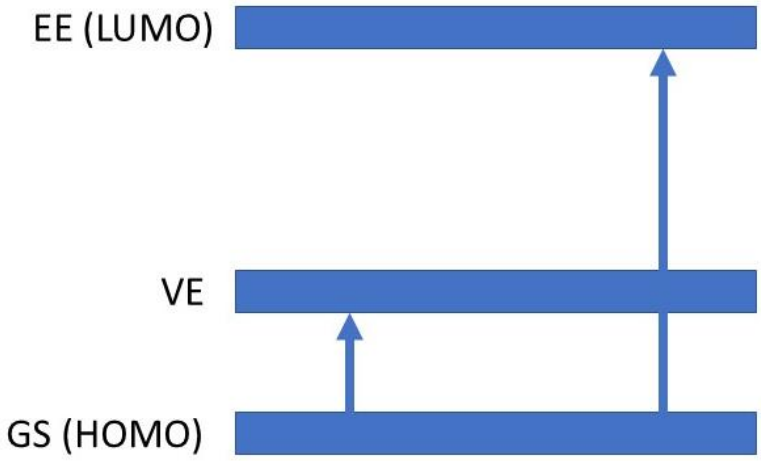

Figure 1-4 Absorption of electromagnetic vibration; GS-Ground State VE-Vibrational Excitation EE-Electronic Excitation HOMO-High Occupied Molecule Orbital LUMO-Low Occupied Molecule Orbital

The molecule in which electronegativity distribution among the atoms is unequal gives rise to a dipole moment. The molecule with a dipole moment will respond to IR. Symmetric vibrations are not observed in IR as they cancel each other out. A part of the incident energy is transferred to the vibrations, and remaining energy is scattered in the form of a photon.

1.2.2 Vibrational Modes

The number of vibration modes is determined by internal degrees of freedom in a molecule. Only those degrees of freedom in which the length and angle between atoms changed were considered. Internal degrees of freedom are defined as follows: for 'N' number of atoms in a molecule

3N-5, if atoms are bonded linearly; 3N-6, if atoms are bonded nonlinearly [(6)].

A molecule has different kinds of vibrations. They are as follows:

- Stretching: change in the length of a bond
- Bending: change in the angle between two bonds
- Rocking: change in angle between a group of atoms

- Wagging: change in angle between the plane of a group of atoms
- Twisting: change in the angle between the planes of two groups of atoms
- Out-of-plane: change in the angle between any one of the bonds and the plane defined by the remaining atoms of the molecule

With the help of FTIR, I analyzed the samples in a condensed phase (solid and liquid) in which $E_{vibrational}$ was taken into account, whereas for the gas phase both $E_{vibrational}$ + $E_{rotational}$ would be considered [6].

1.2.3 Instrumentation

FTIR uses polychromatic light sources. The light that passes through the sample is transmitted to the wavelength sorting device, called the interferometer. The Michelson interferometer in the Fourier transform instrument is an underlying component (Figure 1-5).

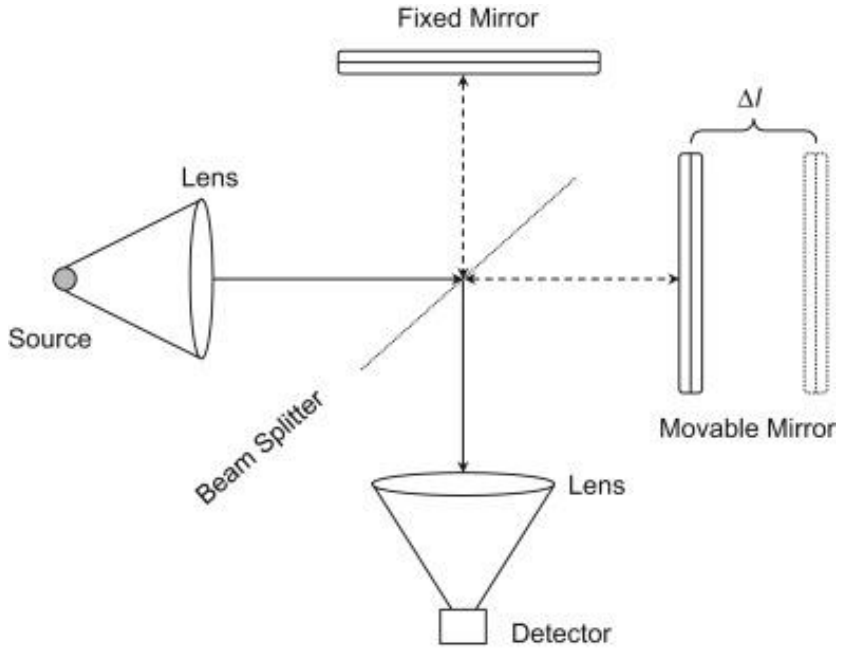

Figure 1-5 Michelson interferometer

The components in a Michelson interferometer include a beam splitter along with a fixed and moving mirror. An ideal beam splitter will divide the collimated light from the source incident into two equal intensity beams where 50% is transmitted to the moving mirror, and the other 50% is reflected to the fixed mirror, illustrated in Figure 1-5. The light

is then reflected off both mirrors back to the beam splitter where 50% is sent to the detector, and the other 50% is lost to the source. As the moving mirror scans, the path difference between the two beams, called the optical retardation, is varied and is two times the distance traveled by the moving mirror. The interferometer records interferograms caused by phase dependent interference of light with different optical retardation.

The instrument used for this study is Bruker Alpha with Attenuated Total Reflection (ATR) attachment. ATR-FTIR is ideal for determining composition, for both the solids and liquids. Bruker Alpha's diamond crystal is brazed into tungsten carbide providing high pressure so that even tough samples can be measured [9].

Bruker's well-proven, permanently aligned RockSolid™ interferometer incorporates dual retro-reflecting gold-coated cube corner mirrors in an inverted double pendulum arrangement (Figure 1-6) and a durable diode laser for maximum efficiency and sensitivity.

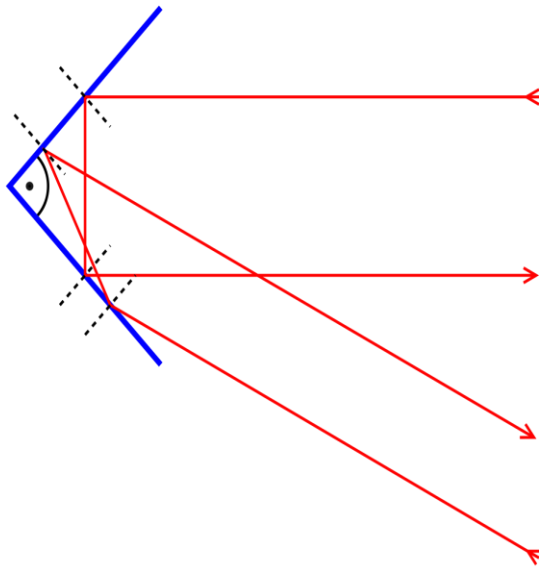

Figure 1-6 Retro reflecting mirror arrangement in RockSolid™ interferometer

I used the Mid-IR region (wavenumber 4000-400 cm^{-1}) for this study. The diagram in Figure 1-7 is useful to understand Attenuated Total Reflection method. The light we obtain from the interferometer is in the form of an evanescent wave, and this wave is made

incident on the sample through an ATR crystal, which has a higher refractive index than the sample.

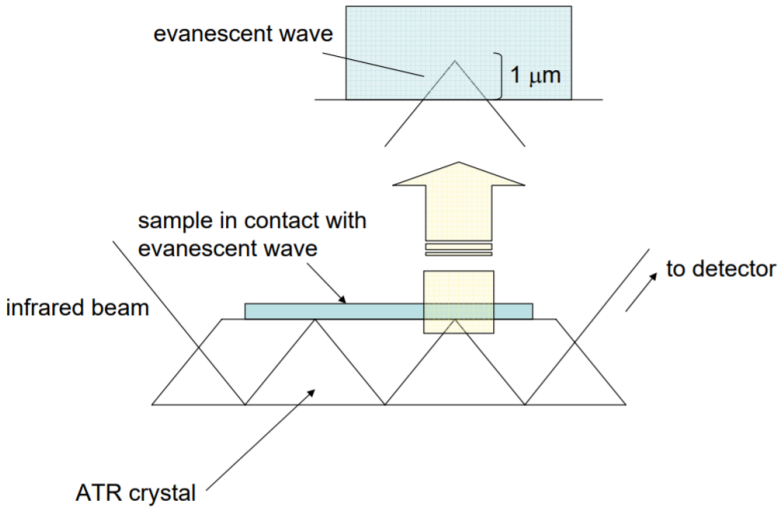

Figure 1-7 Interaction of evanescent wave with sample

Depending upon the composition of the sample, wavelengths are absorbed. A computer was used to perform the fast Fourier transform to generate the spectrum from the absorption of an evanescent wave. The absorption coefficient is a constant for the specific material to a particular wavelength. The analytical method used in IR spectroscopy uses the area under a peak as a quantitative measure.

To obtain the vibrational frequency, the Wilson GF matrix method was used [7]. A matrix G, associated with kinetic energy, was calculated from the atomic masses and molecular geometry whereas matrix F, related to potential energy, was calculated based on the set of force constants. A set was created that could give information about the displacement. Typically, a molecule was constructed in the Cartesian coordinate space and then transferred to the internal coordinate basis set system, which consists of changes in the bond length and bond angle. The product matrix GF was calculated and used in obtaining fundamental frequencies and normal coordinates.

Accurate vibrational analysis requires optimizing the molecular structure and wave functions to obtain the minimum energy state of the molecule. In practice, this involves the

selection of a suitable basis set method for the electron correlation. The selection of the basis set is essential in acquiring acceptable calculated vibrational data necessary to assign experimental IR spectra [8].

The Lambert-Beer law for quantitative analysis in vibrational spectroscopy is stated as follows:

$$A = \log \frac{I_0}{I}$$

Where I_0 is an incident light, I is light passed through the sample, and A is absorbance.

1.3.1 Scanning Electron Microscopy – Bone Characterization Technique

I used the Scanning Electron Microscopy (SEM) method for additional insights into our observations from FTIR. This method provides information about the sample based on electron interaction from beam and sample (Figure 1-8). We covered different aspects of SEM in this section.

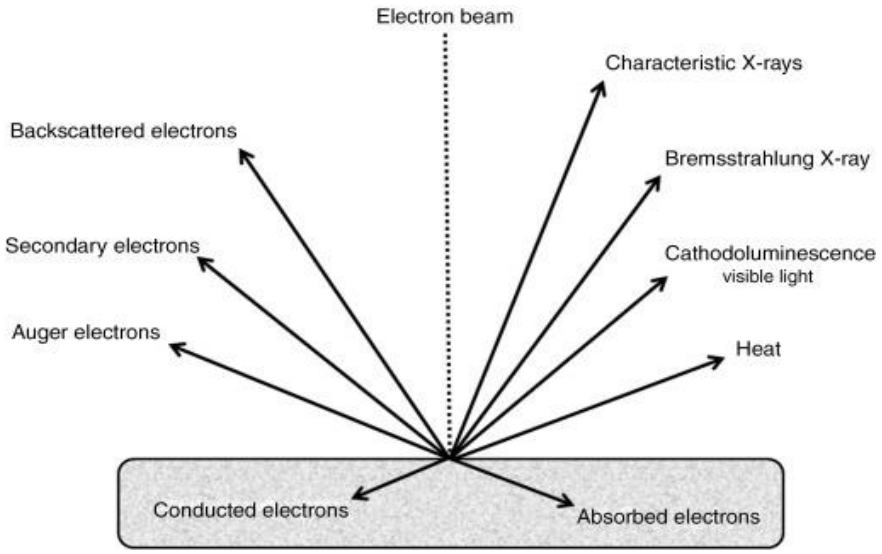

Figure 1-8 Interaction of electron beam with the sample

Electrons travel a longer distance in a vacuum than in the air. Mechanical pumps were used to generate vacuum. In this process, an electron gun was utilized to bombard the electron beam on the sample. Interaction of the electron beam with the sample made electrons scatter from the depth, as well as from the surface, of the sample. The electron

gun has three parts [10]: (1) a cathode consisting of a filament that emits the electron and creates a cloud of an electron around itself; (2) a cylinder containing the aperture to minimize the area of electron cloud with negatively applied voltage; and (3) an anode, a disc containing the aperture, that accelerates the electrons 0.5 to 30 kV.

Two types of filaments are typically used: a thermionic emission filament (e.g., tungsten) and a gun field emission filament. Most commonly, tungsten was used and had surface work function of 4.5 eV. Tungsten's temperature was raised to 2700 K. This increase in temperature provided the kinetic energy to the electron to overcome the surface energy barrier and leave the filament.

The electron column consists of condenser lenses, objective lenses and scanning lenses. The lenses, located immediately after the disc aperture, are the condenser lens; the objective lens is near the sample. The condenser lens helps to concentrate the electron cloud to 5 to 50 nm in diameter.

I obtained the compositional and topographical nature of the sample. An electron beam was scanned in raster scan pattern, providing the image from interaction with atoms. We ran the sample analysis in the high vacuum or the low vacuum. Scattered electrons from the surface are called as Secondary Electrons (SE) and are generally within few nanometers of the surface, whereas Back Scattered Electrons (BSE) are deep down in the material. Secondary Electron Imaging (SEI) uses SE and provides topographic contrast. Back Scattered Imaging (BSI) provides compositional contrast by using BSE. Factors affecting the image are beam current, working distance, surface morphology and composition of the sample.

In the high vacuum, a conductive sample surface is necessary to analyze with SE. Conductance avoids charge buildup on the sample caused by the electron beam [10]. During imaging, electrons are bombarded on the sample, producing a negative charge that builds up in areas of the sample under the beam. This negative charge, when sufficiently large, can deflect the incident and emitted electrons, thus ruining the image. Each sample

must be electrically conductive to prevent such effect so that the current deposited by the electron beam on the sample can pass through the sample stage to the electrical ground.

If a sample is not conductive, one can analyze the sample with BSE in a low vacuum condition. In this method, positive ions are led toward the surface where electrons interact with these positive ions and charging effect is neutralized. The air molecules introduced in the vacuum chamber react with primary electrons leading to disturbance in informative image formation. However, the resolution of BSE images is less than the SE images at higher magnification.

For biological samples, some work was completed with SE to increase the bulk conductivity of the material by impregnation with osmium using variants of the OTO staining method (O-osmium tetroxide, T-thiocarbohydrazide, O-osmium) [(12)].

1.3.2 X-ray Energy Dispersive Spectroscopy

In X-ray Energy Dispersive Spectroscopy (EDS), information can be obtained about the elemental composition of a sample. After the interaction of electron beam with the sample, electrons are removed from the shell of the sample, creating a vacancy (Figure 1-9).

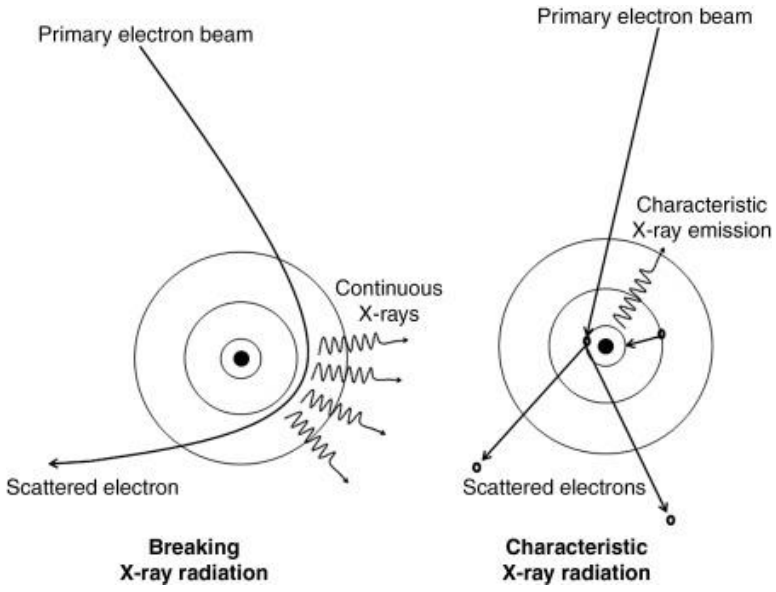

Figure 1-9 X-ray energy dispersive spectroscopy with characteristic X-ray generation

The electron jumps from a higher orbital to the lower orbital creating a vacancy in the previous orbital. Because electrons have discrete energy along their orbitals, jumping from a high energy orbital to low energy orbital releases the characteristic x-ray radiation equaling the difference between the orbits.

The depth range of the chemical microanalysis depends on the energy of the beam that reaches the sample. Therefore, samples that are homogeneous throughout their depth can be analyzed without concern for the beam's energy [13].

We used the HITACHI S3000n for the microscopy of bone. Since bone is non-conductive, we implemented the low vacuum silver (Ag) sputter coat to make bone surface conductive.

1.4 Sample Preparation for SEM with Sputtering

Because high vacuum is an optimal working condition for this experiment, the sample surface is supposed to be conductive and I facilitated this conductivity with a silver coating by the sputtering process. A conductive layer avoids charging effect by creating a channel to remove charging electrons from the sample. The coating achieved with the sputtering had a thickness ranging from angstroms to microns.

The sputtering process involves inert gas, in this case, argon. The target material, silver, acted as a cathode. The sample was placed in the anode. The cathode was kept cold, and the anode could be heated or cooled (Figure 1-10).

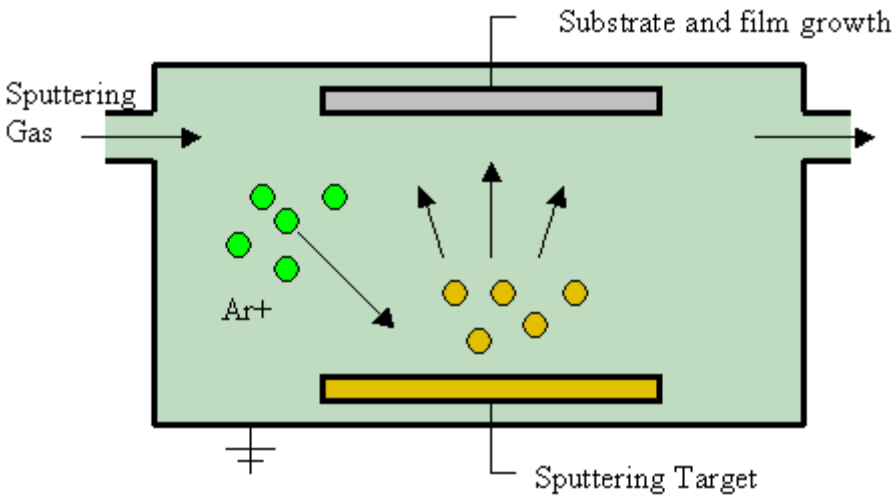

Figure 1-10 Principle of the sputtering process

The electrically energized cathode was used to establish a self-sustaining plasma of argon gas. These ions are attracted to the cathode. To definite the target area. a magnet was used under the silver cathode. These argon ions sputtered the silver cathode releasing the silver ions. Then, sputtered silver ions were deposited on the sample material. Pressure played an essential role in this process. Pressure should be high enough to reduce the mean free path and was maintained at 5 to 10 millitorr in this process.

The following are the advantages of the sputtering process:

- Makes the sample surface conductive by reducing sample charging
- Improves secondary electron emission
- Reduces electron beam damage
- Coats parameters
- Increases in thermal conduction and protection of the sample, which is beam sensitive

Chapter 2 Experiments

2.1 Motivation

Clubfoot is associated with fstl 5 gene alteration. Clubfoot (scientific name Talipes Equinovarus (TEV)) is a deformity of the leg, ankle, and foot (Figure 2-1) and results from a structural defect of several tissues in the leg and foot, leading to the abnormal growth of the foot and ankle joints.

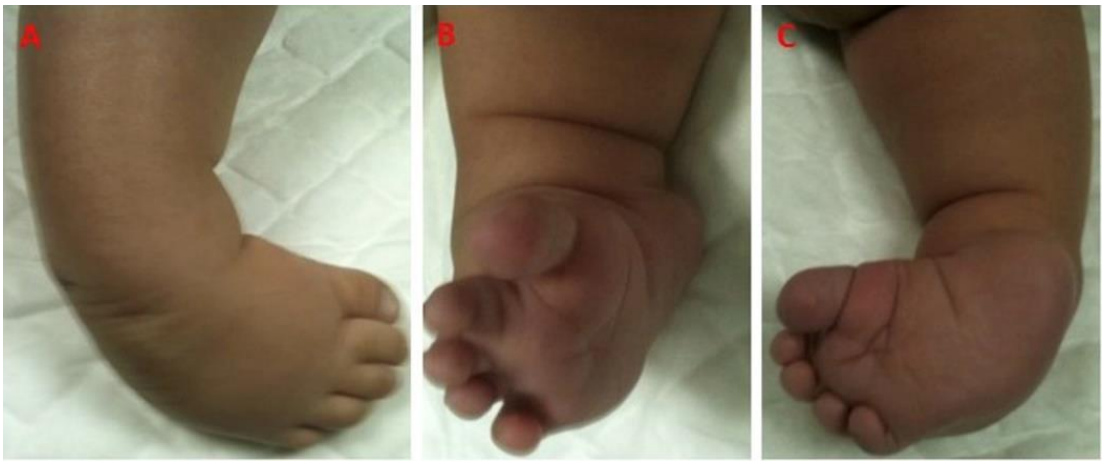

Figure 2-1 Clinical photographs of an individual with clubfoot: a) dorsal view, b) and c) plantar view [16]

Diagnosis of clubfoot can be made at birth or before birth during the ultrasound test. Researchers at UTSRC indicated that fstl 5 gene is associated with clubfoot disorder. They analyzed 399 human clubfoot subjects and 7,820 ethnicity matched controls by conducting genome-wide genotyping imputation and association. To prepare the samples, UTSRC researchers disabled the pathway of the fstl 5 gene in Sprague Dawley Rats.

Rat bone samples, received from UTSRI, were from females of different age groups. Each age group had a combination of WT and KO rat bone. Bone has different sections along its length (Figure 2-2): epiphyses, metaphysis, and diaphysis. The epiphysis is related to the cancellous bone, whereas diaphysis is related to the cortical bone. In the characterization of bone, both sections were considered.

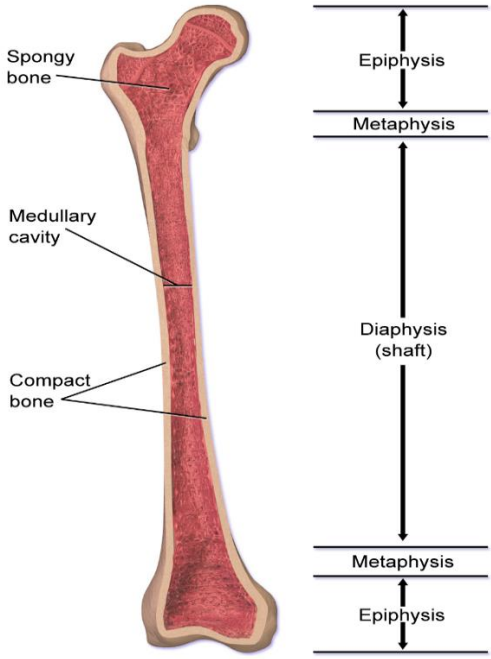

Figure 2-2 Longitudinal section of bone

Bone samples were cut longitudinally in half with a diamond saw and were cleaned inside out (Figure 2-3(a)). For the FTIR experiment, it was necessary to have flat contact between the sample and stage. I decided to cut the longitudinal section into small pieces with an area around 28 mm^2 to keep track of position-wise spectrum (Figure 2-3(b)).

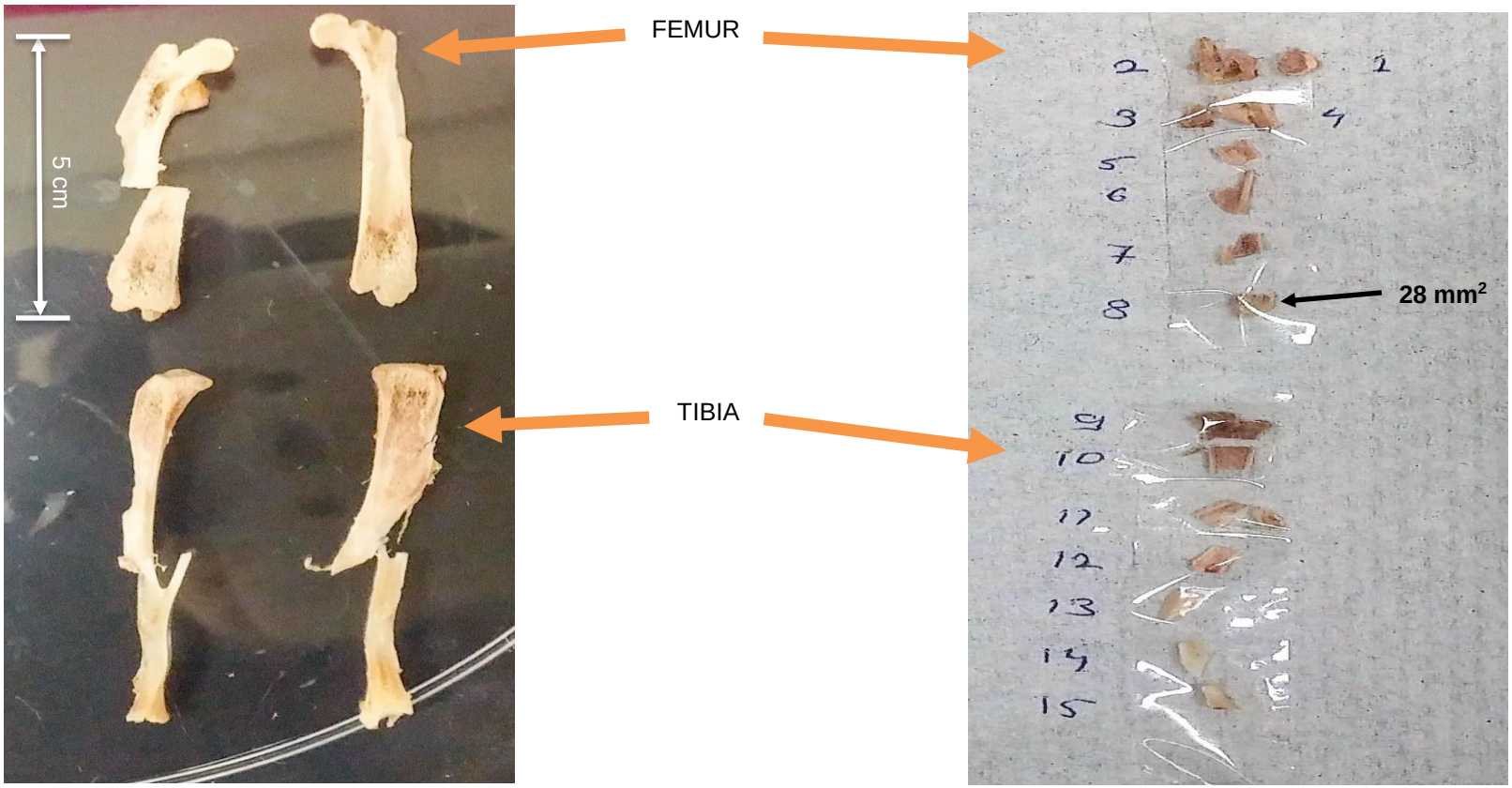

(a) (b)

Figure 2-3 Bone sample 1-23-17-11F KO, (a) the longitudinal cut with a bone saw and (b) small pieces of the same sample, along with the scale

Chapter 3 Observations

3.1 FTIR Observations

Every spectrum we obtained indicated high fluorescence (Figure 3-1) due to the presence of organic constituents. There is a deproteination process to avoid such fluorescence [3]. Since we wanted to retain original bone composition, we did not eliminate the organic constituents in the bone. Fluorescence can be suppressed by exposing the sample to multiple scans of the exciting light wavelengths before taking the infrared spectrum. This method cannot always entirely eliminate the fluorescence and can overheat the sample. We used 32 scans in fluorescence suppression mode for our measurements, but most of our spectra had some fluorescence background. We implemented baseline method to subtract the fluorescence. Table 3-1 indicates essential components of bone, and their wavenumbers, present in the spectrum.

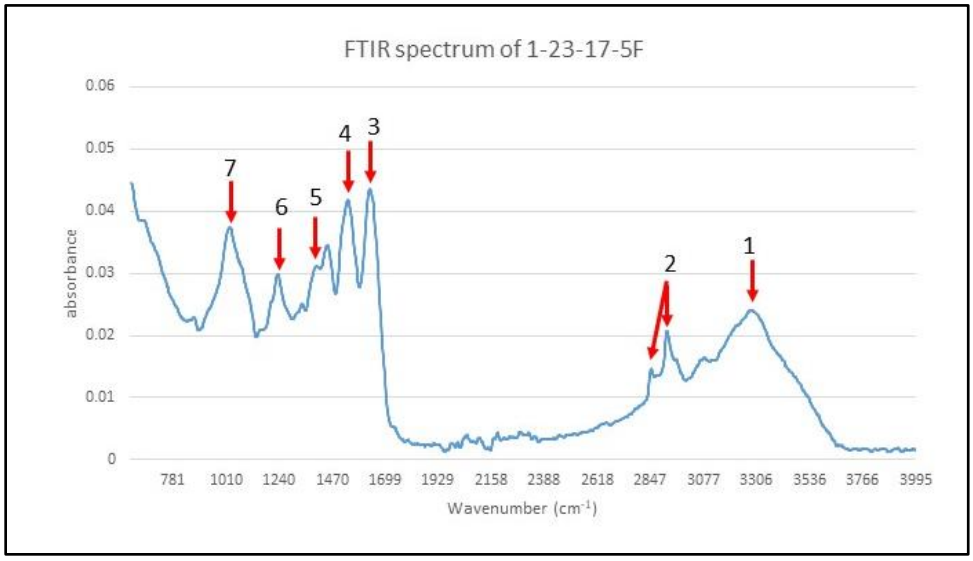

Figure 3-1 Typical FTIR spectrum for mid-diaphysis of bone

Table 3-1 Components present in Figure 3-1 and their wavenumbers

Sr. No.	Component	Wavenumber (cm^{-1})
1	OH^-	3280
2	CH_2	2922 & 2852
3	Amide I	1631
4	Amide II	1541
5	CO_3^{2-}	1405
6	Amide III	1235
7	PO_4^{3-}	1014

In this study, the area under the phosphate (PO_4^{3-}) peak and amide I peak were considered. I saw the typical spectrum for a sample on the femur with the fluorescence throughout spectra. We eliminated the fluorescence with the baseline method (Figure 3-2). After implementing the baseline method, I took the integral area under the peak into account regarding the quantity of the compound.

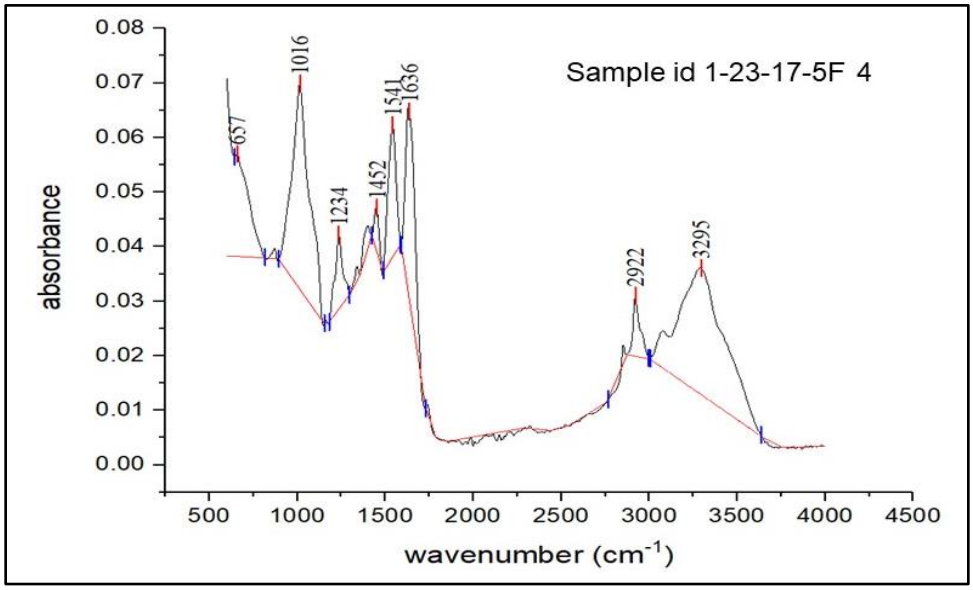

Figure 3-2 Baseline method implemented on the FTIR spectra to obtain an integral area under the peak

3.1.1 Heterogeneity of Bone

The graphs in the following sections show the FTIR spectra as taken from the numbered bone positions. The difference in the spectra shows the heterogeneity of bone. The positions at which spectra were taken were along different locations along the length of the bones (see Figure 2-2 and Figure 2-3). There are two reasons for the heterogeneity and accompanying variation in the spectra. One is the lack of uniformity in the microstructure of the complex composite composition of bone. The other reason is that different locations along the bone represent different growth stages in the development of the bone. At each growth stage, the composition and mineral to matrix ratio is varying. The long bones (femur and tibia) grow from each end, so the more central locations represent more mature bone. Bone growth starts with the formation of collagen (matrix), to which more phosphorus and calcium (mineral) is deposited as growth proceeds. Specialized cells (called osteoblasts) deposit matrix and minerals to promote bone growth. At the same time, other specialized cells (called osteoclasts) remove minerals to reshape and reform bone in response to stresses, nutrition, and other factors. Thus bone formation is a dynamic process subject to many influences as the animal grows. The result is the highly heterogeneous structure indicated in the SEM images and data that will be presented in a later section (Section 4-2).

Each animal is slightly different, both genetically and in its growth environment, resulting in variation in the bone structure and the mineral and matrix content at any location. Only by averaging a number of comparable measurements on different animals can a useful comparison of KO and WT bones be made. In this study, the methodology and techniques were demonstrated for obtaining reproducible and accurate measurements using FTIR were developed. These methods will be useful for gathering more data with larger numbers of animal samples, when these become available not only for TEV KO animals, but for genetically modified animals demonstrating other types of disorders as well.

The following sections show the initial spectra data taken along the length of the bone, and how it is compared and consolidated to draw the conclusions about the overall mineral and matrix. I plotted every FTIR spectra in a single graph for each position of each femur and tibia (Figure 3-3). We marked different locations on the bone with sequential numbers from 1 to 8 on the femur and 9 to 15 on the tibia.

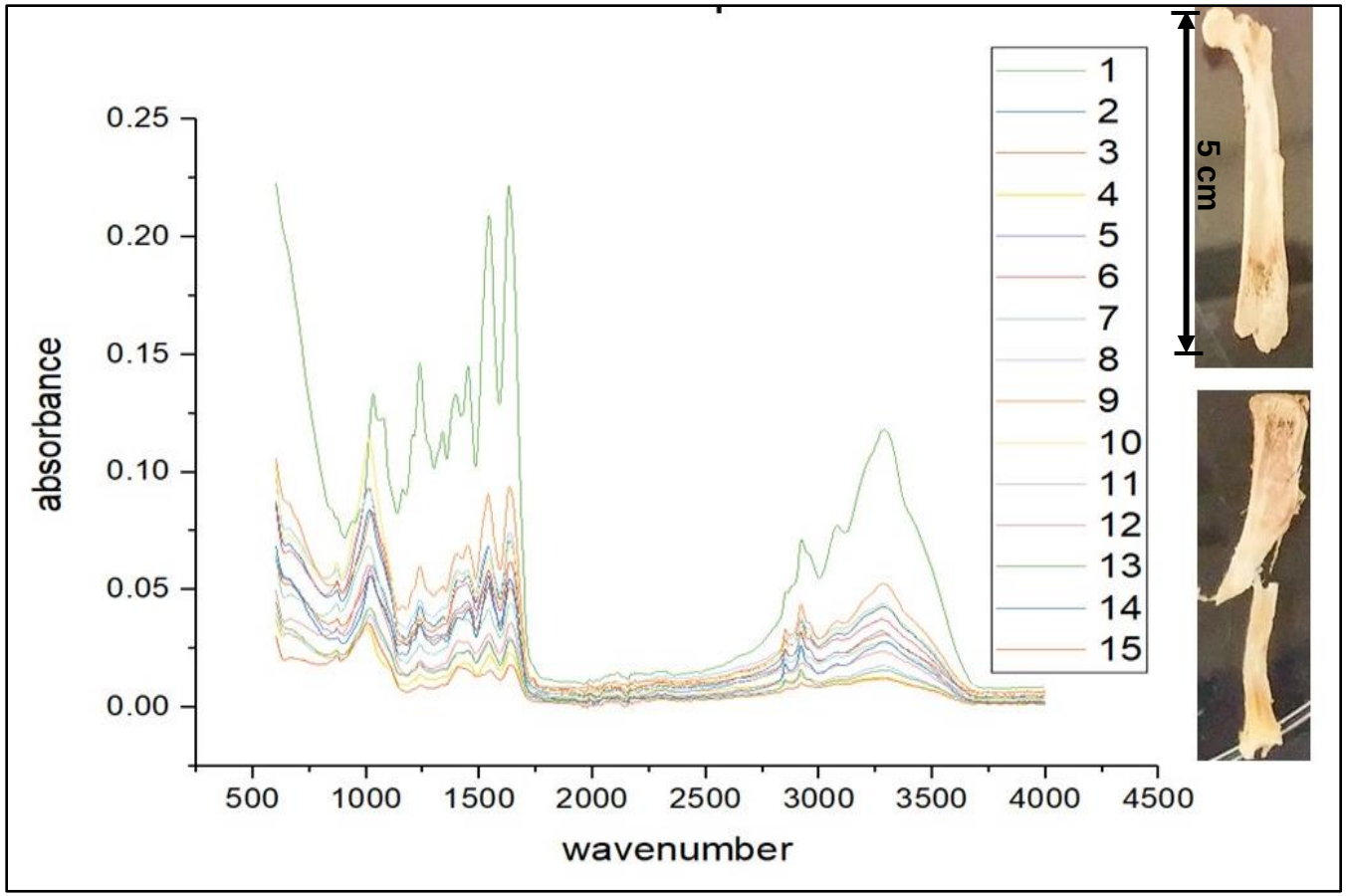

Figure 3-3 FTIR spectra of the single sample on different locations, 1-8 on the femur and 9-15 on the tibia, along with the scale

Furthermore, I analyzed FTIR spectra along with the Mn/Mx of each position for all the samples (Figure 3-4 through Figure 3-31). The difference in the spectra shows the heterogeneity of bone. Due to the differences in the sample condition, I did not see positions 3, 14 and 15 in some samples.

In the following graphs, the mineral and matrix peaks are indicated by star and diamond markers:

★ denotes mineral content (i.e., phosphate peak at a particular wavenumber). Typically, mineral's wavenumber range was 1010-1020 cm^{-1}.

◆ denotes matrix content (i.e., amide I peak at specific wavenumber). Usually, matrix's wavenumber range was 1630-1634 cm^{-1}.

3.2.1 FTIR Spectrum of 1-23-17-5F WT

5F was the only WT sample from the 1-23-17 age group. Since I sampled along the length of the bone, the variation in wavenumber of the matrix was limited, whereas that of the mineral was significant for both femur and tibia (Figures 3-4a and 3-4b). The femur had distinctive peaks of mineral for each position with a maximum absorbance of 16% at position 1.

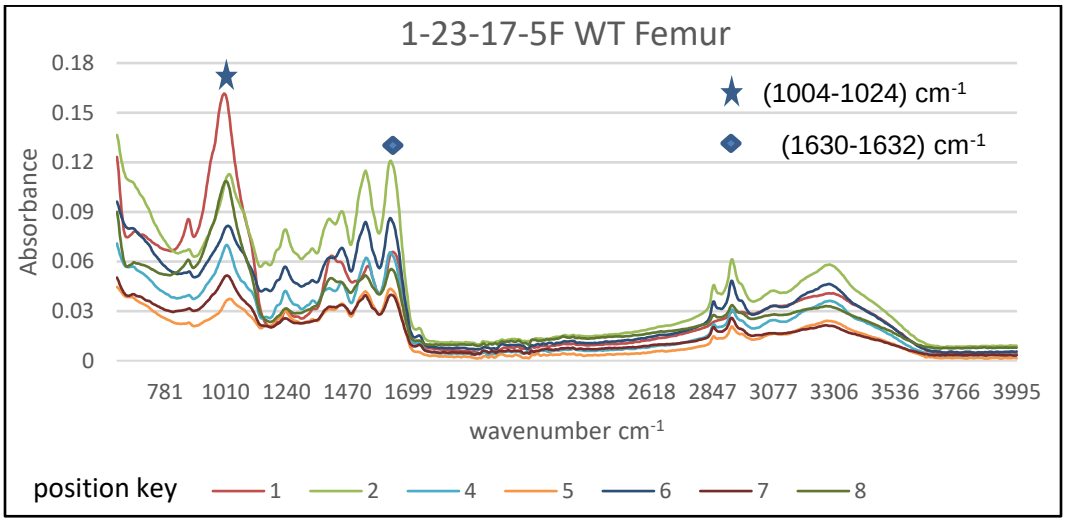

Figure 3-4(a)

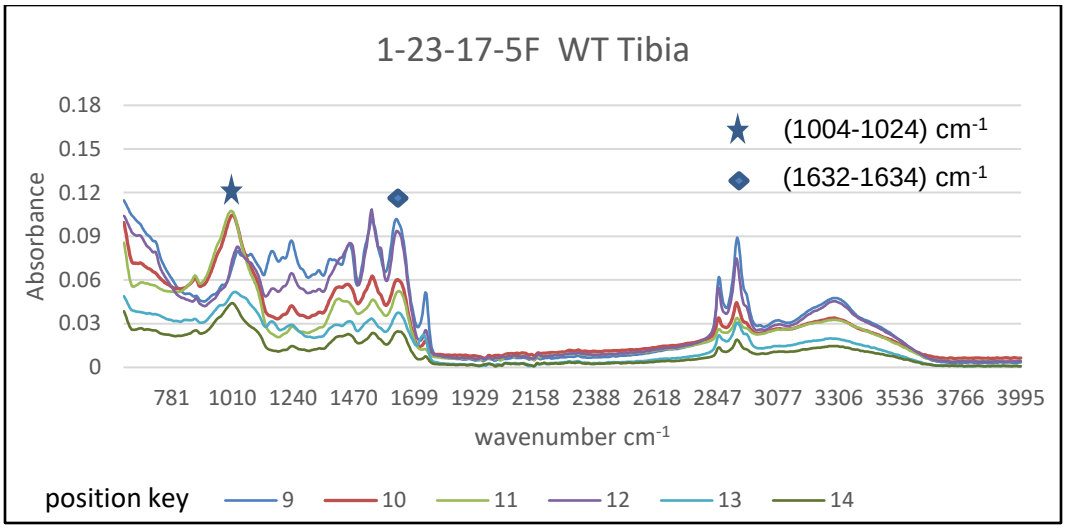

Figure 3-4(b)

Figure 3-4 FTIR spectra of bone sample 1-23-17-5F WT, (a) Femur (b) Tibia

3.2.2 Mn/Mx of 1-23-17-5F WT

For the femur, positions at which the absorbance for mineral and matrix peaks were the same gave a higher Mn/Mx ratio than the other locations (Figures 3-4a and 3-5a). For the tibia, positions at which absorbance for the mineral was a higher than the matrix show higher Mn/Mx than the other positions (Figures 3-4b and 3-5b). These differences may represent different growth regions along the development of the bone.

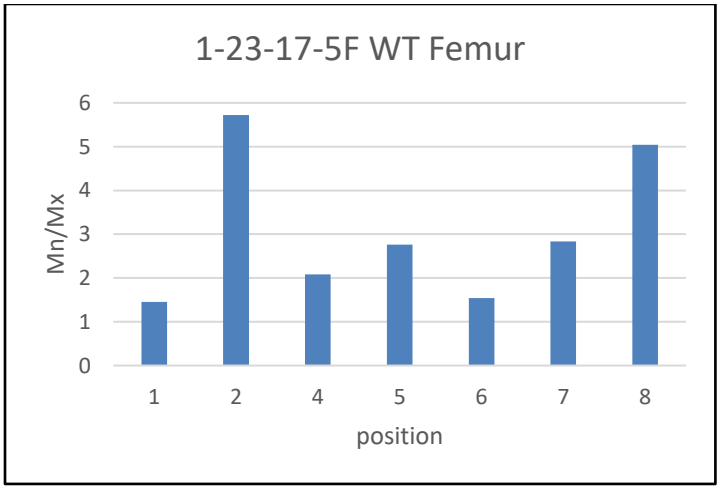

Figure 3-5(a)

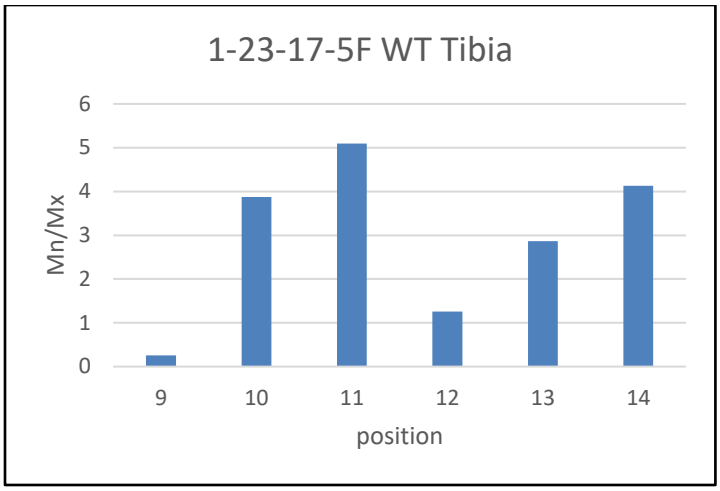

Figure 3-5(b)

Figure 3-5 Mn/Mx of bone sample 1-23-17-5F WT, (a) Femur (b) Tibia

3.3.1 FTIR Spectrum of 1-23-17-9F KO

9F was a KO sample from the 1-23-17 age group. As I traversed the bone length, the variation in wavenumber of mineral and matrix for both femur and tibia was substantial (Figure 3-6). CH_2 and OH^- peak height was reduced more than the other compounds (Figure 3-6a). The highest absorbance was around 11% for a mineral, which was same for all the tibia samples in a 1-23-17 group (Figure 3-6b).

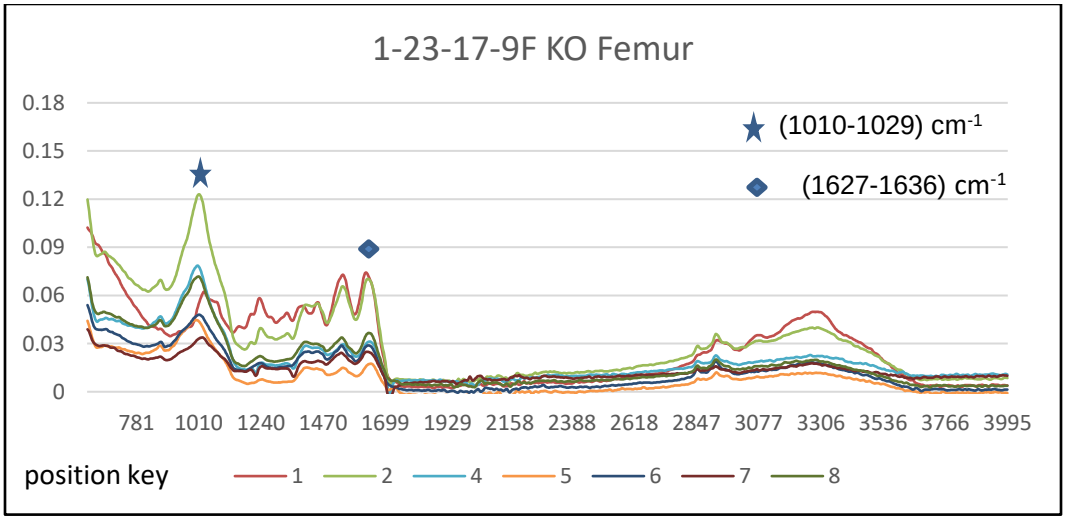

Figure 3-6(a)

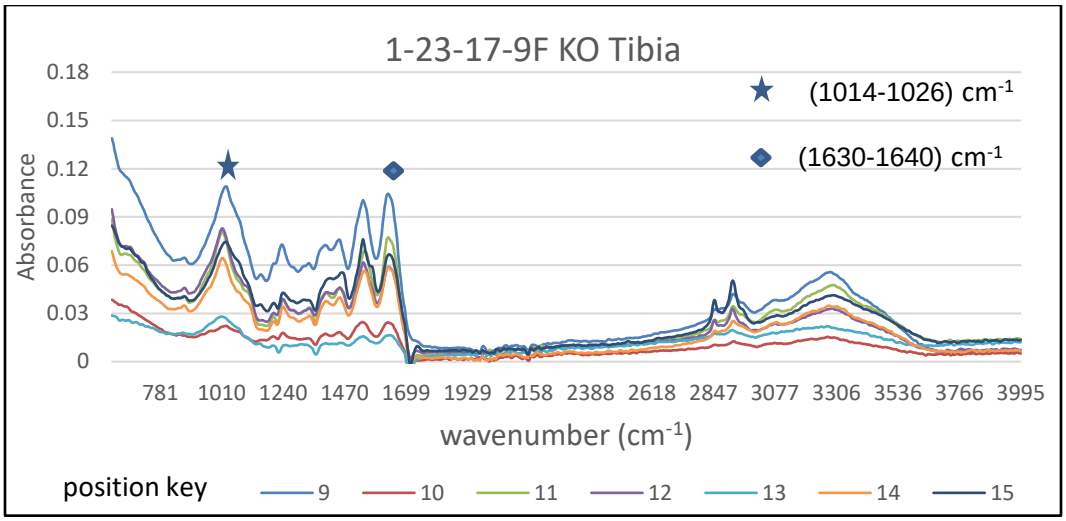

Figure 3-6(b)

Figure 3-6 FTIR spectra of bone sample 1-23-17-9F KO, (a) Femur (b)Tibia

3.3.2 Mn/Mx of 1-23-17-9F KO

The femur shows elevated Mn/Mx for all the positions (Figure 3-7a), whereas the tibia shows consistently low Mn/Mx for all the positions. The OH^- peak widening and CH_2 peak lowering could be related to the elevated Mn/Mx in the femur (Figures 3-6a and 3-7a). I observed lowered Mn/Mx when there was an increase in absorbance of OH^- and CH_2 peaks (Figures 3.6b and 3-7b).

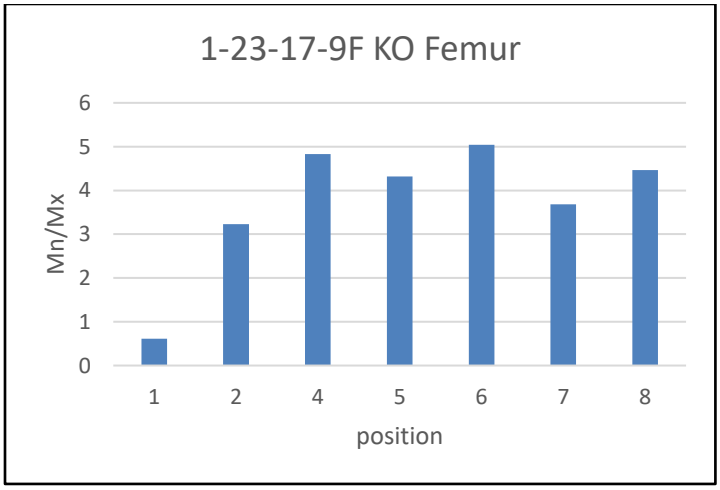

Figure 3-7(a)

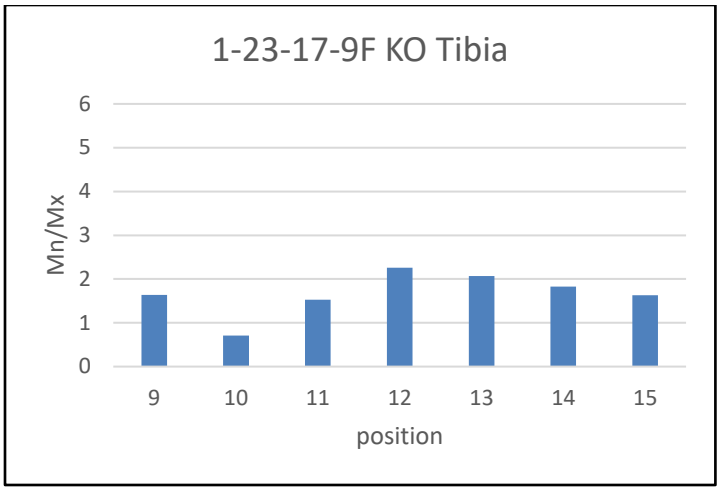

Figure 3-7(b)

Figure 3-7 Mn/Mx of bone sample 1-23-17-9F KO, (a) Femur (b) Tibia

3.4.1 FTIR Spectrum of 1-23-17-11F KO

11F was a KO sample in the 1-23-17 age group. For amide I, the highest absorbance (around 22%) was observed in a femur from the 1-23-17 group (Figure 3-8a). The variation in wavenumber of the mineral was significant for both femur and tibia (Figures 3-8a and 3-8b).

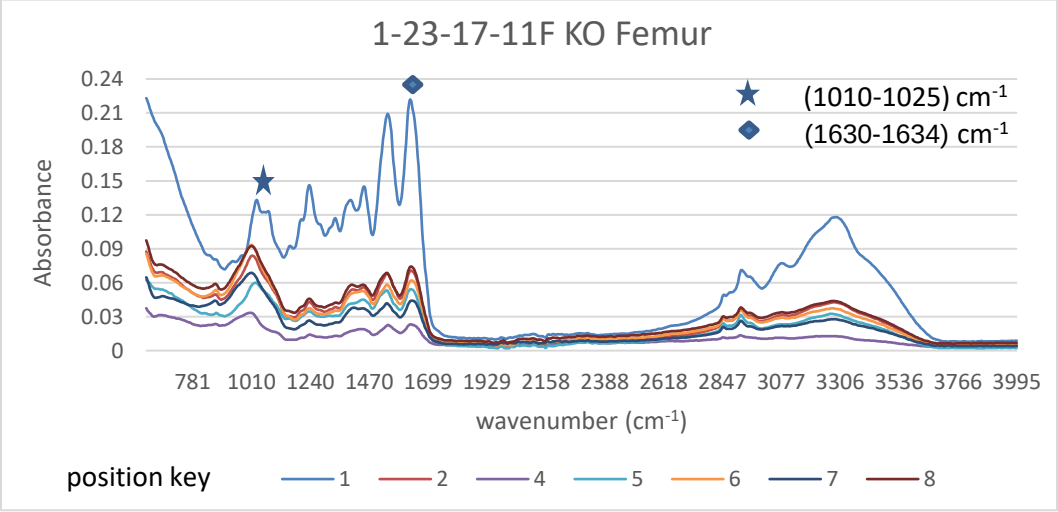

Figure 3-8(a)

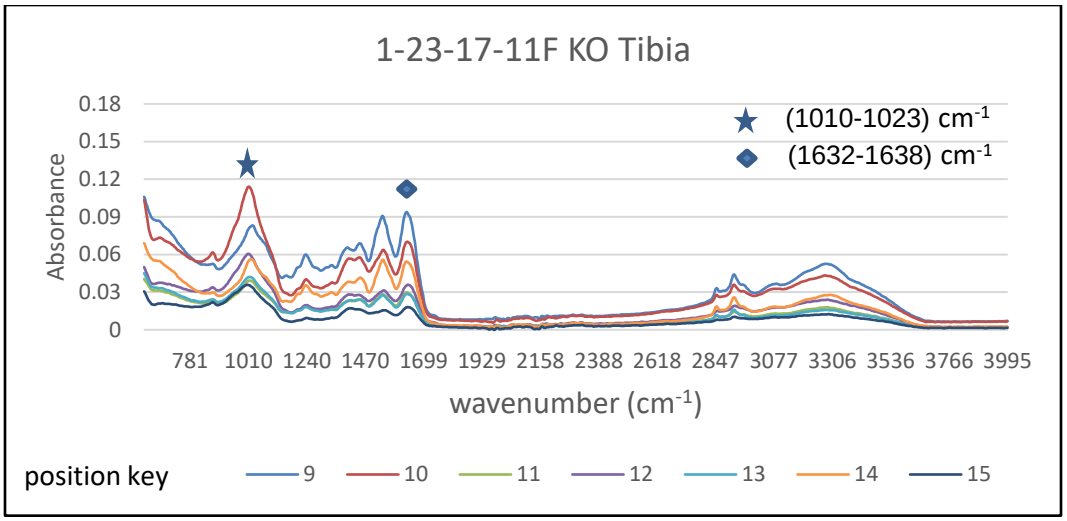

Figure 3-8(b)

Figure 3-8 FTIR spectra of bone sample 1-23-17-11F KO, (a) Femur (b) Tibia

3.4.2 Mn/Mx of 1-23-17-11F KO

Mn/Mx for most of the positions was around the median for the femur and tibia (Figures 3-9a and 3-9b). This case was observed in both KOs in the 1-23-17 age group, though there are differences in their averages.

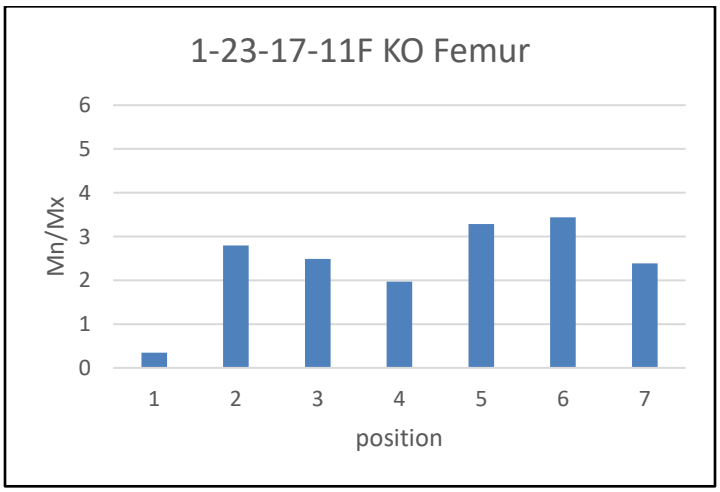

Figure 3-9(a)

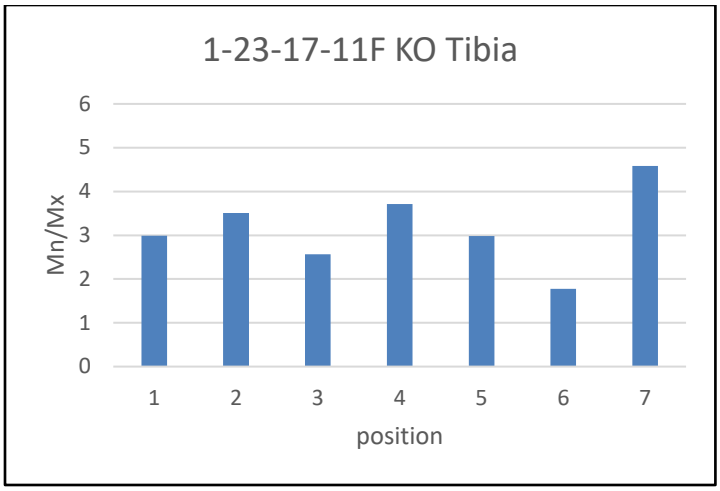

Figure 3-9(b)

Figure 3-9 Mn/Mx of bone sample 1-23-17-11F KO, (a) Femur (b) Tibia

3.5.1 FTIR Spectrum of 3-8-17-1F WT

1F was the only sample in the 3-8-17 age group and was a WT. The lengthwise variation in wavenumber of mineral and matrix was limited for the femur, whereas for the tibia, it was large (Figures 3-10a and 3-10b). The femur had overlapping peaks of mineral (Figure 3-10a). There were distinctive peaks of mineral and matrix for the tibia (Figure 3-10b).

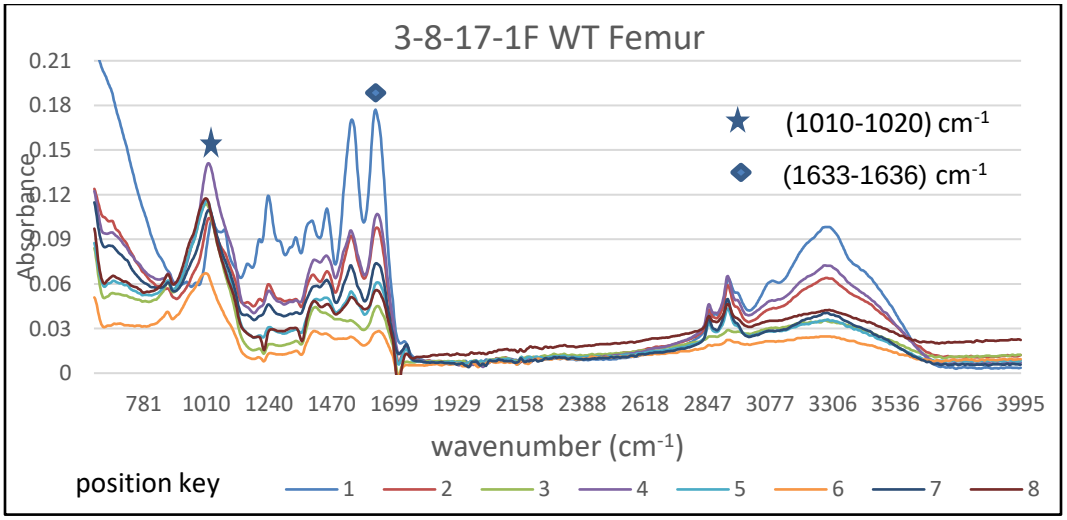

Figure 3-10(a)

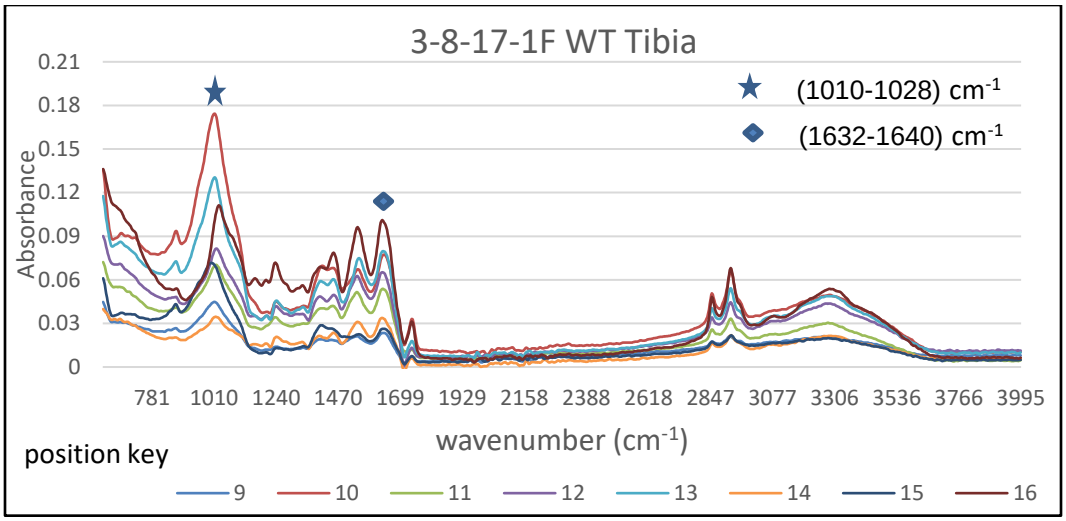

Figure 3-10(b)

Figure 3-10 FTIR spectra of bone sample 3-8-17-1F WT, (a) Femur (b) Tibia

3.5.2 Mn/Mx of 3-8-17-1F WT

Comparing previous age groups' WT samples also indicated a substantial variation in Mn/Mx for both the femur and tibia (Figures 3-11a and 3-11b).

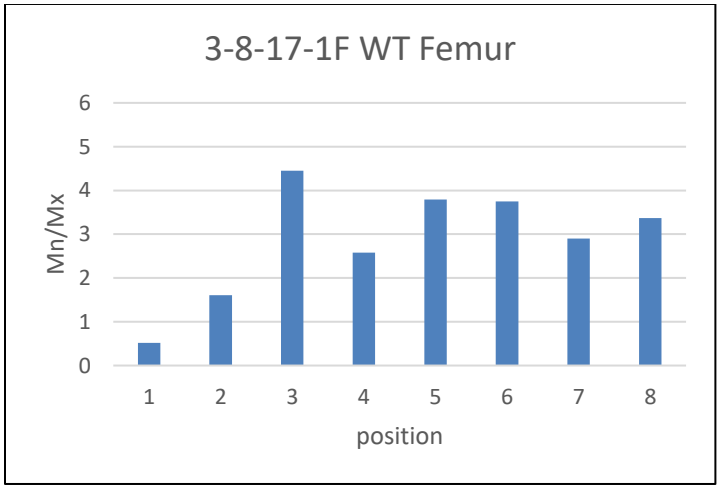

Figure 3-11(a)

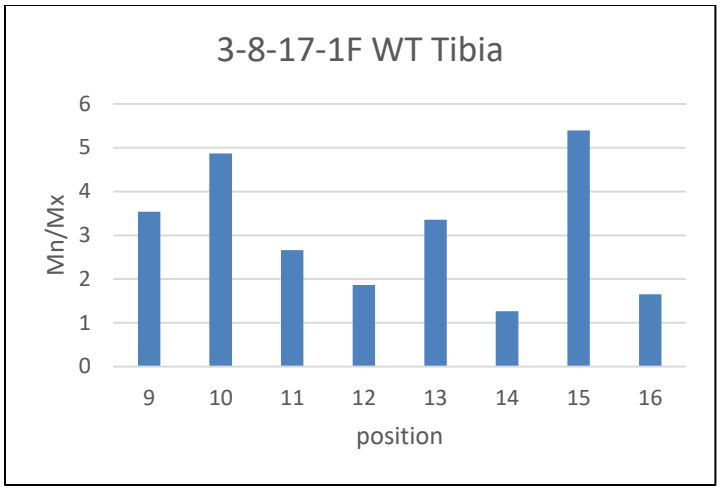

Figure 3-11(b)

Figure 3-11 Mn/Mx of bone sample 3-8-17-1F WT, (a) Femur (b) Tibia

3.6.1 FTIR Spectrum of 3-10-17-1F WT

1F was a WT sample in the 3-10-17 age group. The wavenumber variation of mineral and matrix along the bone was limited with a distinctive spectrum for each position (Figure 3-12a). The highest absorbance was observed in the matrix for the femur at position 1. Position 14's spectrum indicated a high absorbance peak of CH_2, and the variation in wavenumber of mineral and matrix was large (Figure 3-12b).

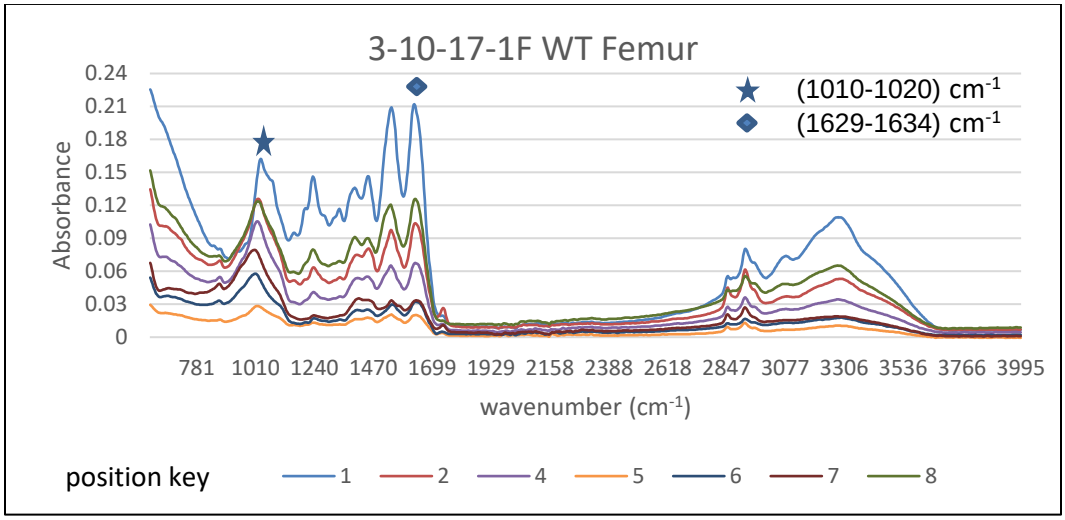

Figure 3-12(a)

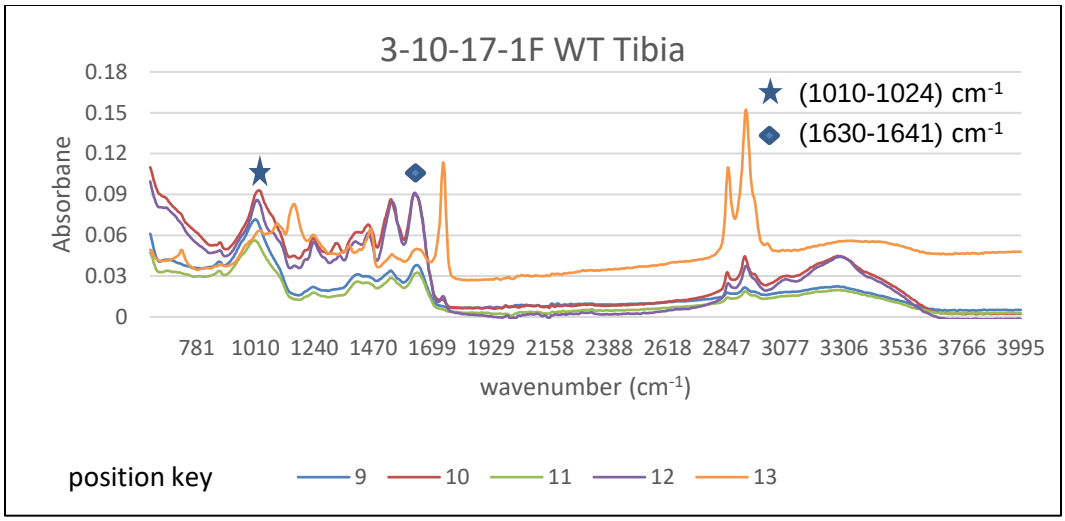

Figure 3-12(b)

Figure 3-12 FTIR spectra of bone sample 3-10-17-1F WT, (a) Femur (b) Tibia

3.6.2 Mn/Mx of 3-10-17-1F WT

Consistent for Mn/Mx with earlier samples, WT's Mn/Mx indicated much more variability than KO (Figures 3-13a and 3-13b). Due to the sample condition, I could not obtain Mn/Mx for positions 14 and 15.

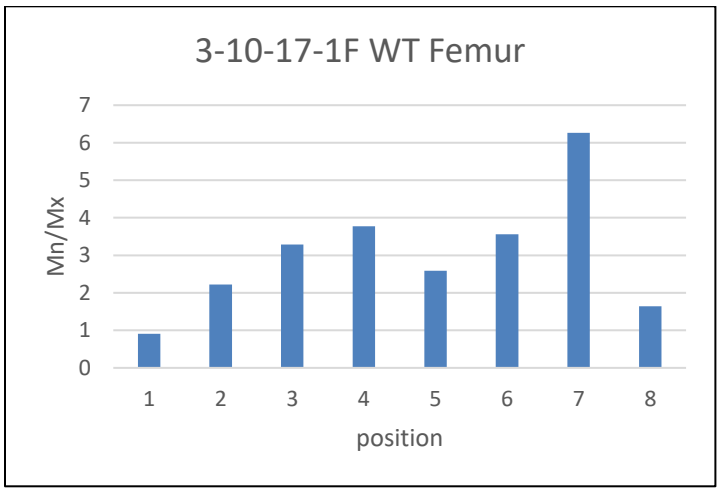

Figure 3-13(a)

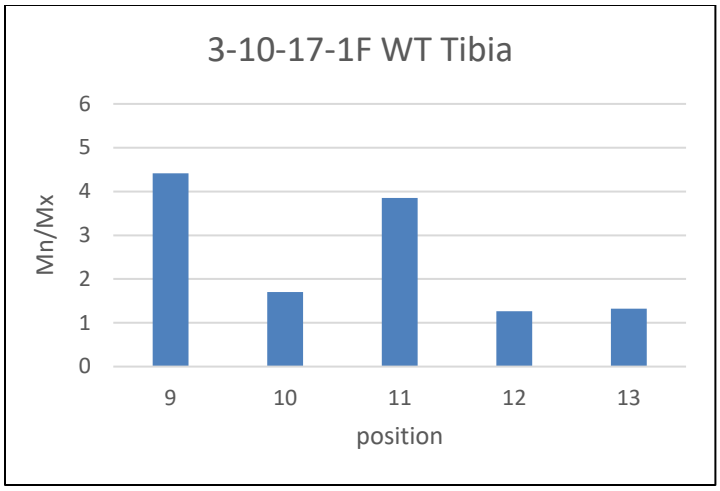

Figure 3-13(b)

Figure 3-13 Mn/Mx of bone sample 3-10-17-1F WT, (a) Femur (b) Tibia

3.7.1 FTIR Spectrum 3-10-17-3F KO

3F was the only KO sample in the 3-10-17 age group. For the femur and tibia, the variation in wavenumber of mineral and matrix was limited (Figure 3-14a and 3-14b). The peaks of CH_2 and OH^- had the least height among all the components.

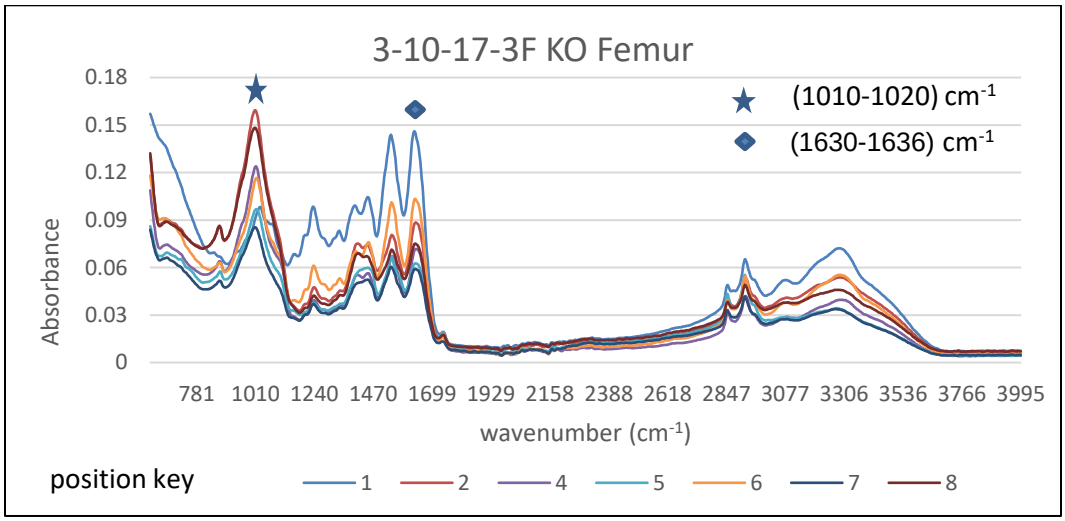

Figure 3-14(a)

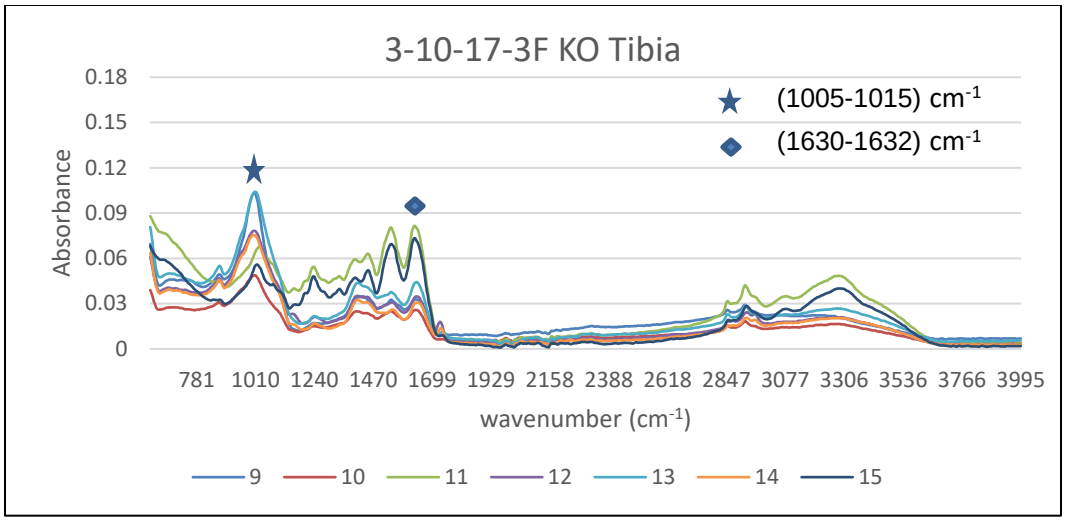

Figure 3-14(b)

Figure 3-14 FTIR spectra of bone sample 3-10-17-3F KO, (a) Femur (b) Tibia

3.7.2 Mn/Mx of 3-10-17-3F KO

Mn/Mx for the KO sample indicated the median value for most positions on the bone was near to the overall mean value for both femur and tibia (Figures 3-15a and 3-15b). In particular, I observed a value of 9.6 for Mn/Mx in the tibia for position 9. Positions 1 and 11 indicated a lower Mn/Mx than all the other positions.

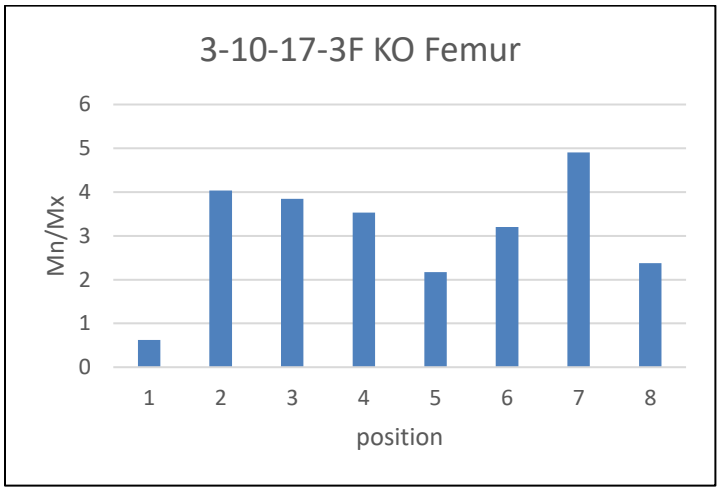

Figure 3-15(a)

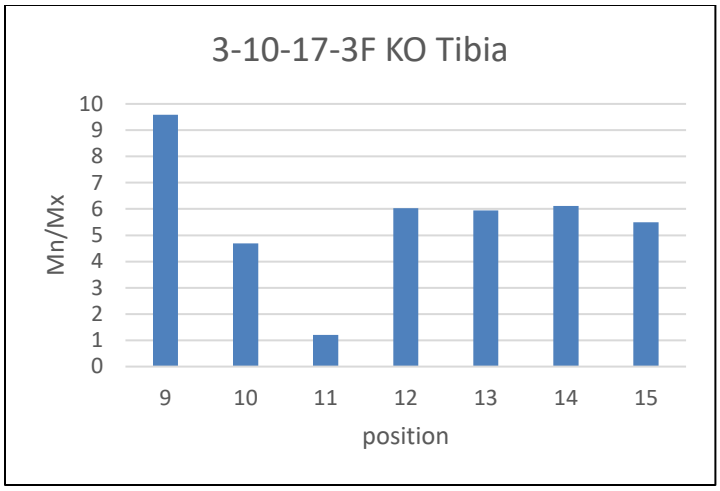

Figure 3-15(b)

Figure 3-15 Mn/Mx of bone sample 3-10-17-3F KO, (a) Femur (b) Tibia

3.8.1 FTIR Spectrum of 3-10-17-7F WT

7F was one of the WT samples of the 3-10-17 age group and had the most limited variation in wavenumber of mineral and matrix for the femur (Figure 3-16a). Position 14's spectrum had the elevated absorbance of the CH_2 peak, and I observed overlapping peaks for most of the tibia positions (Figure 3-16b).

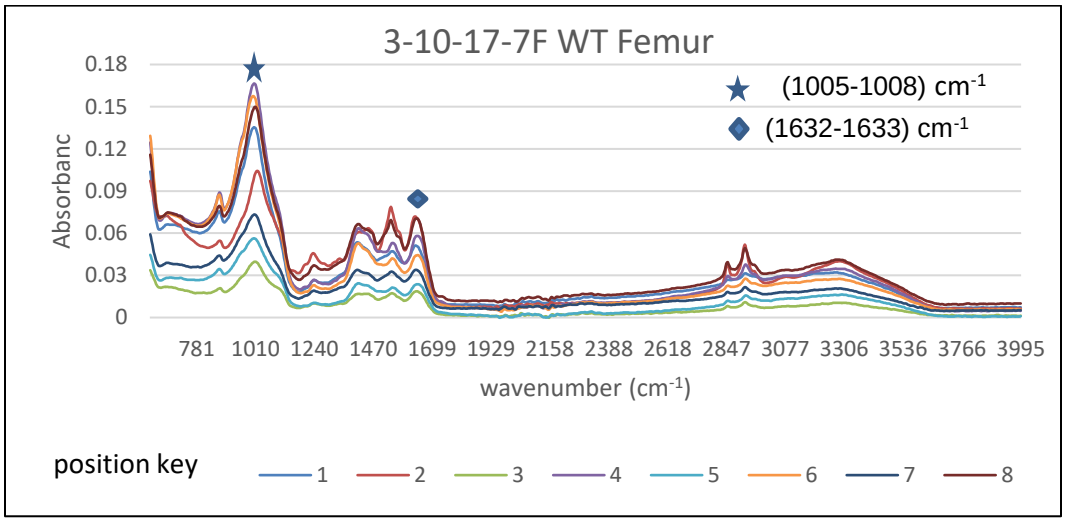

Figure 3-16(a)

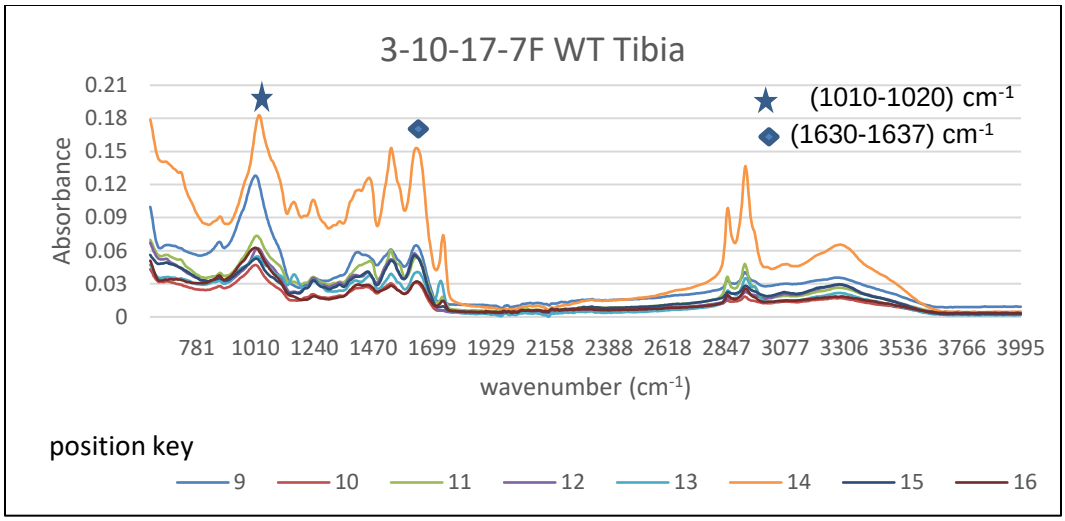

Figure 3-16(b)

Figure 3-16 FTIR spectra of bone sample 3-10-17-7F WT, (a) Femur (b) Tibia

3.8.2 Mn/Mx of 3-10-17-7F WT

Figure 3-17 illustrates the 7F sample, among all the WTs, is an exception as it indicates less difference in the mean and median of Mn/Mx for both the femur and tibia, resembling the characteristics of KO. At position 6, Mn/Mx was high at around 10.

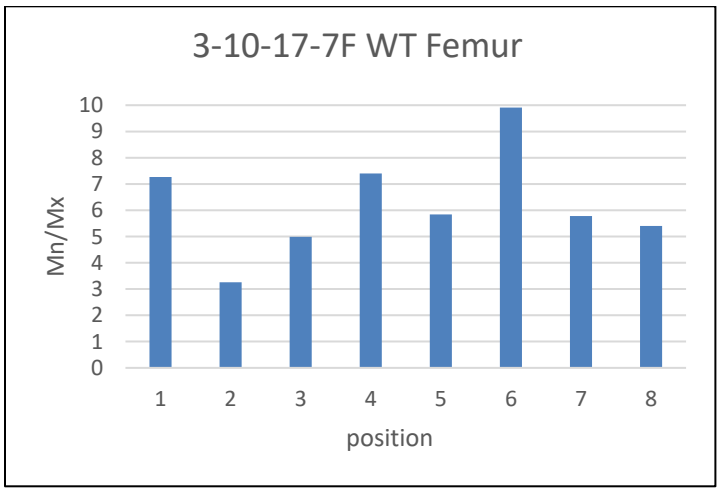

Figure 3-17(a)

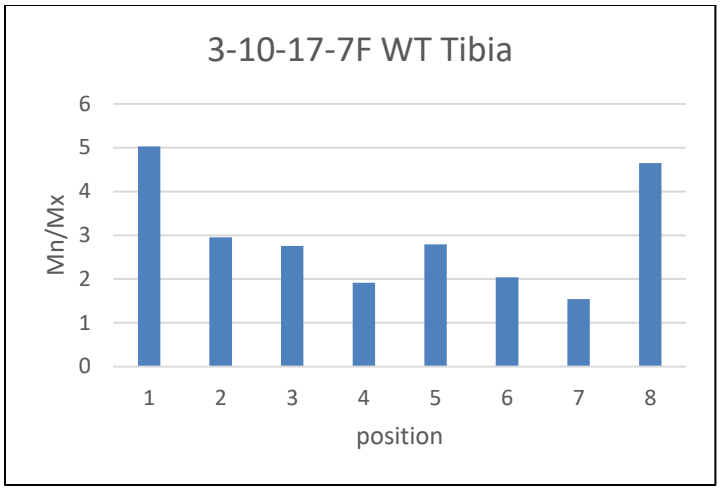

Figure 3-17(b)

Figure 3-17 Mn/Mx of bone sample 3-10-17-7F WT, (a) Femur (b) Tibia

3.9.1 FTIR Spectrum of 3-10-17-11F WT

This is a WT sample in the 3-10-17 age group. The variation in wavenumber of the mineral was significant for both the femur and tibia (Figure 3-18a and 3-18b) but was limited for the matrix. Heights of CH_2 and OH^- peaks were lower than other compounds in the femur (Figure 3-18a). At position 15, I noted a higher absorbance peak of CH_2.

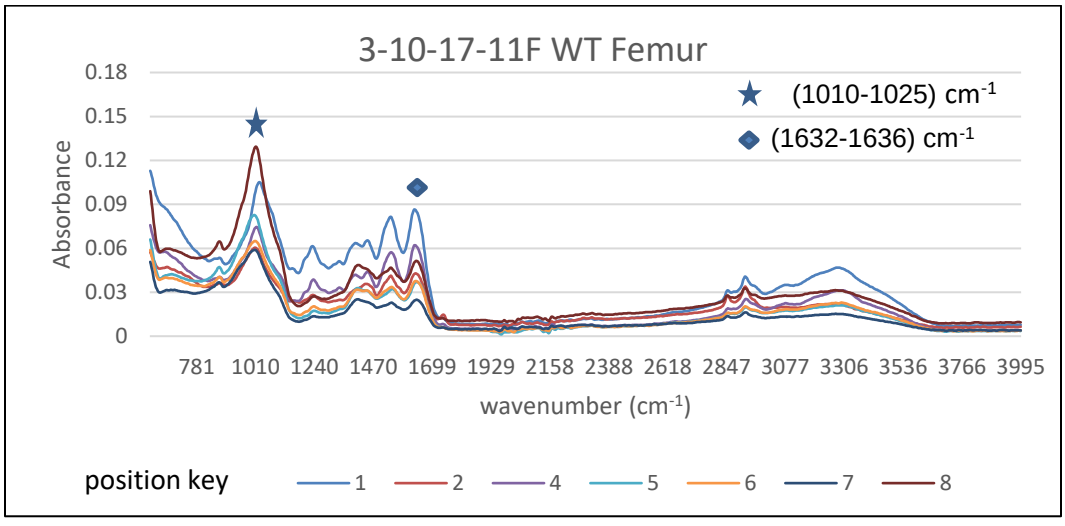

Figure 3-18(a)

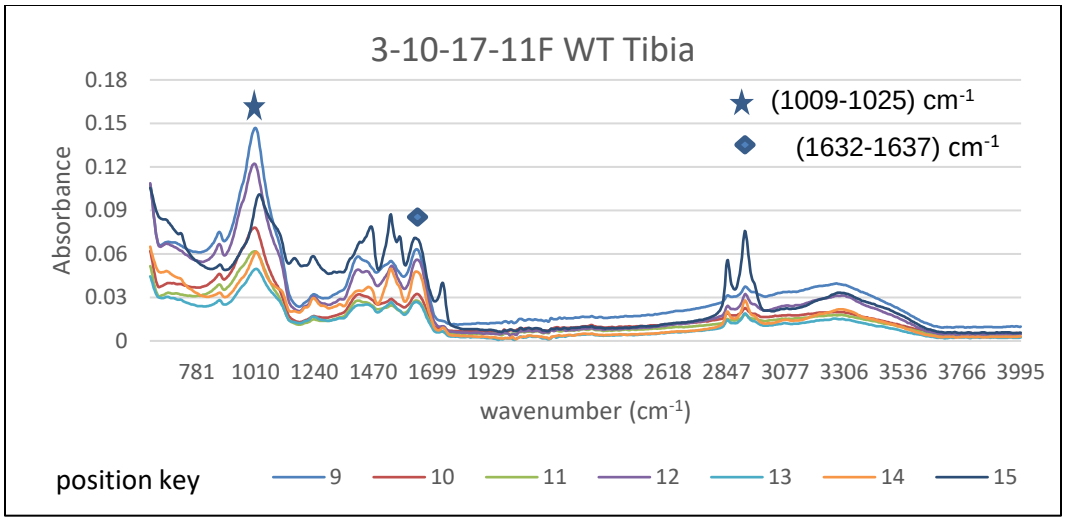

Figure 3-18(b)

Figure 3-18 FTIR spectra of bone sample 3-10-17-11F WT, (a) Femur (b) Tibia

3.9.2 Mn/Mx of 3-10-17-11F WT

At position 4, mineral absorbance was higher than other positions; however, Mn/Mx ratio was lower than all other positions of the femur (Figure 3-19a). The femur followed the same observation for the WTs: difference in the median and mean is minimum. The tibia had consistently higher Mn/Mx throughout the sample (Figure 3-19b).

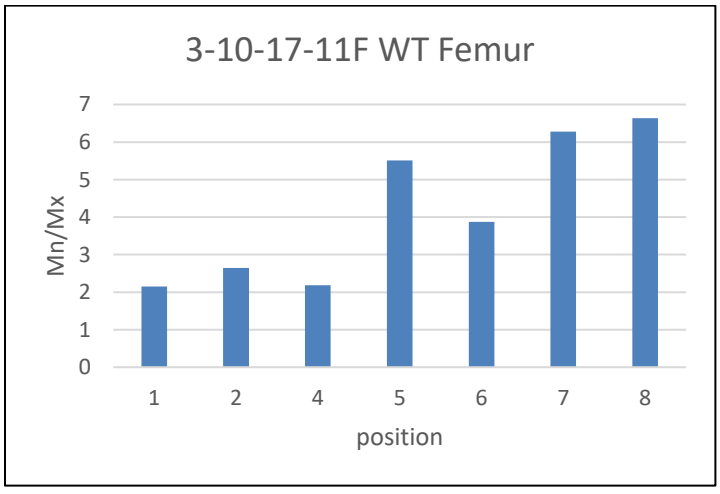

Figure 3-19(a)

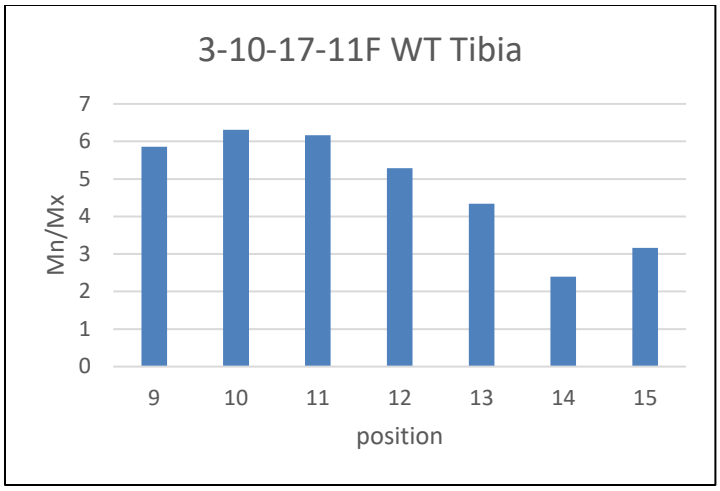

Figure 3-19(b)

Figure 3-19 Mn/Mx of bone sample 3-10-17-11F WT, (a) Femur (b) Tibia

3.10.1 FTIR Spectrum of 3-10-17-12F WT

12F was also a WT in the 3-10-17 age group. The femur had overlapping spectra, except for position 2, which indicated an exceptionally high absorbance spectrum (Figure 3-20a), whereas the tibia had distinctive peaks for mineral (Figure 3-20b). The variation in wavenumber of mineral and matrix was limited for both the femur and tibia. For lower absorbance peak broadening occurred.

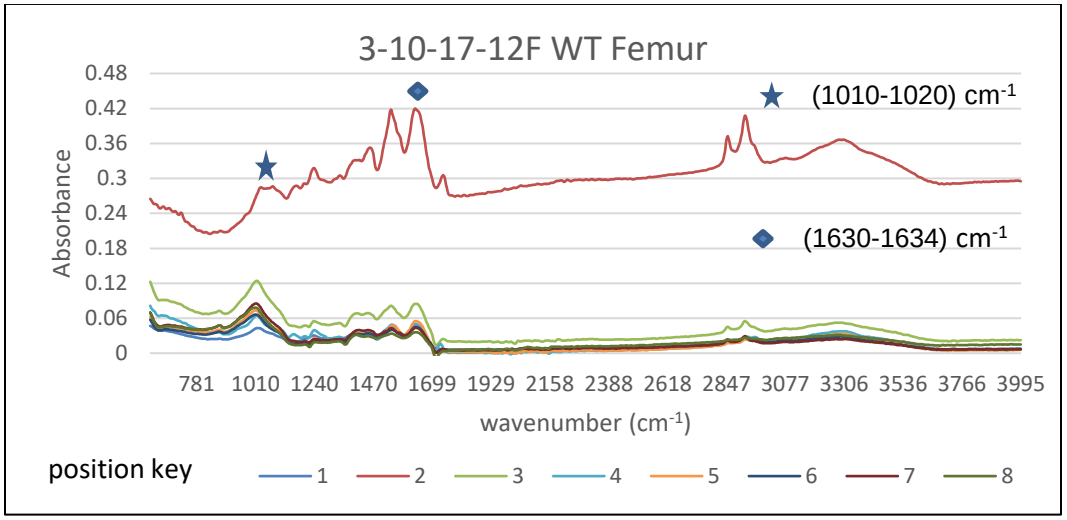

Figure 3-20(a)

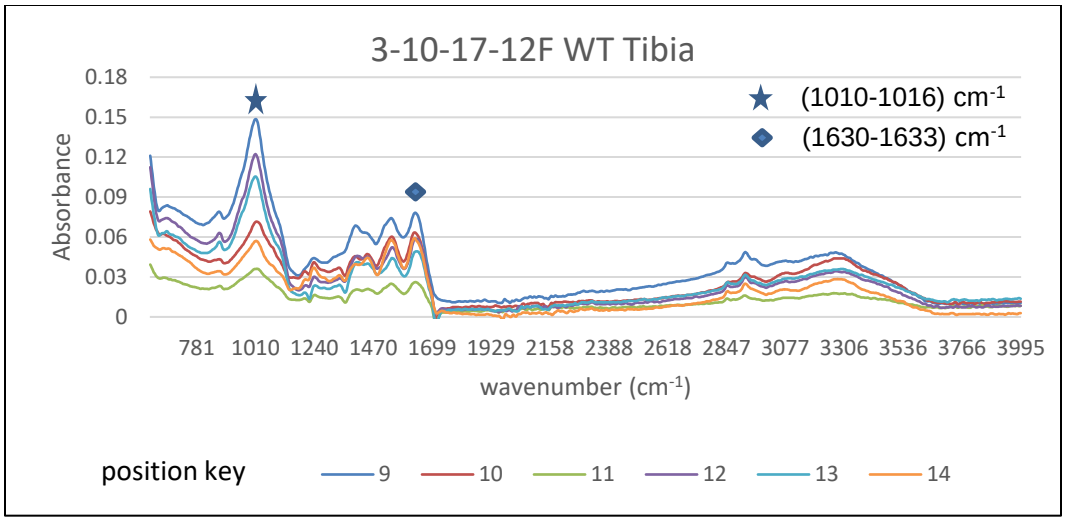

Figure 3-20(b)

Figure 3-20 FTIR spectra of bone sample 3-10-17-12F WT, (a) Femur (b) Tibia

3.10.2 Mn/Mx of 3-10-17-12F WT

For position 2, the spectrum indicated a higher absorbance but had a lower Mn/Mx as the mineral peak absorbance was less than the matrix peak. For both the femur and tibia, difference in the median and mean was high (Figure 3-21).

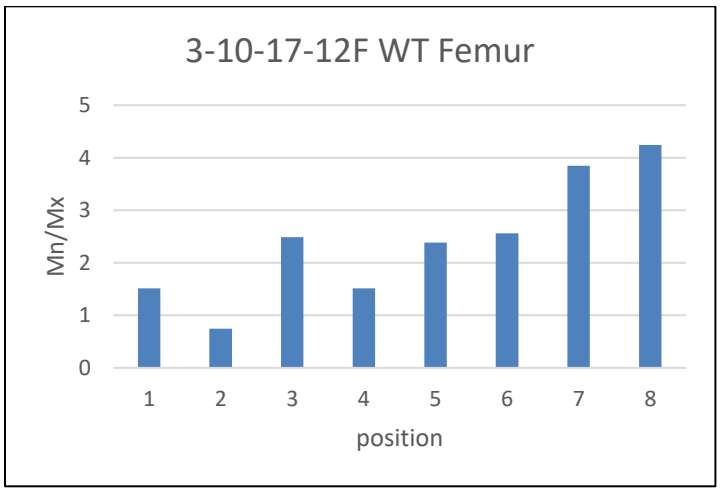

Figure 3-21(a)

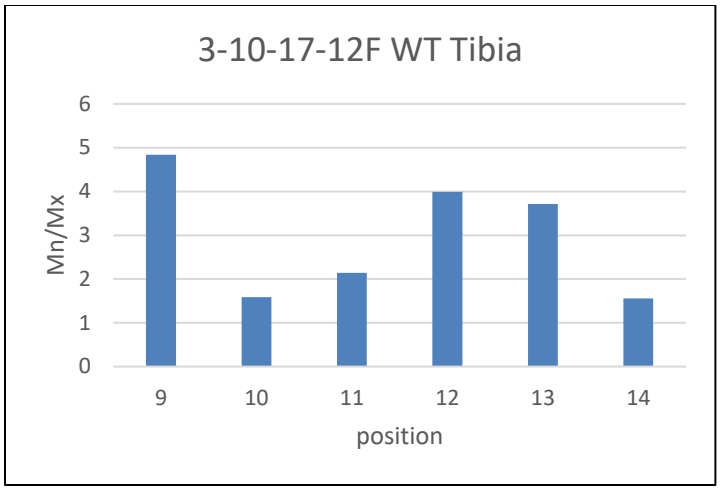

Figure 3-21(b)

Figure 3-21 Mn/Mx of bone sample 3-10-17-12F WT, (a) Femur (b) Tibia

3.11.1 FTIR Spectrum of 3-13-17-2F WT

2F was a WT sample in the 3-13-17 age group with a maximum variation in mineral wavenumber, especially for the tibia (Figure 3-22). Most spectra overlapped in the femur with a low absorbance peak of CH_2 and OH^-.

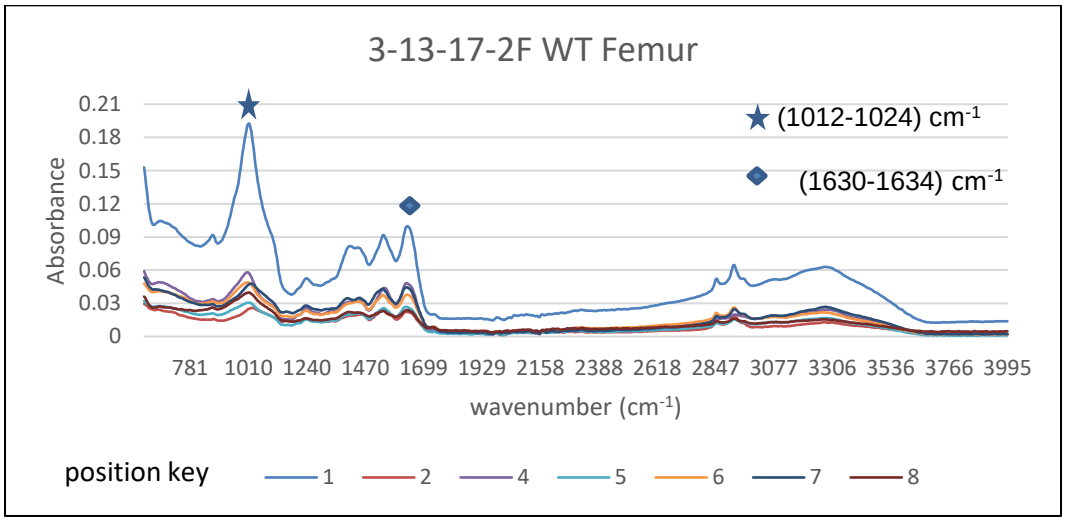

Figure 3-22(a)

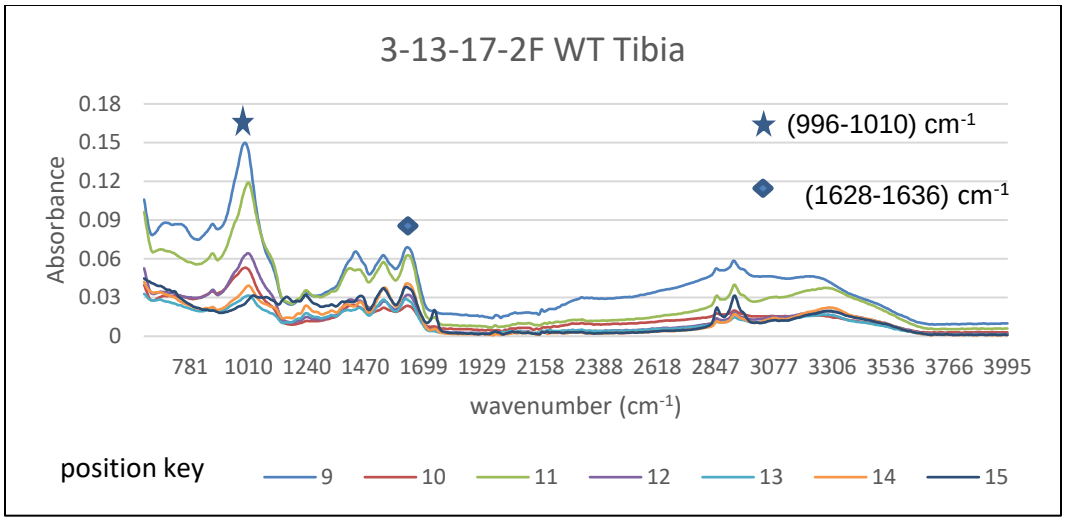

Figure 3-22(b)

Figure 3-22 FTIR spectra of bone sample 3-13-17-2F WT, (a) Femur (b) Tibia

3.11.2 Mn/Mx od 3-13-17-2F WT

Peaks with higher absorption indicated elevated Mn/Mx for both the femur and tibia (Figure 3-23). Extreme positions indicated elevated Mn/Mx in the femur. Initial positions on tibia indicated higher Mn/Mx.

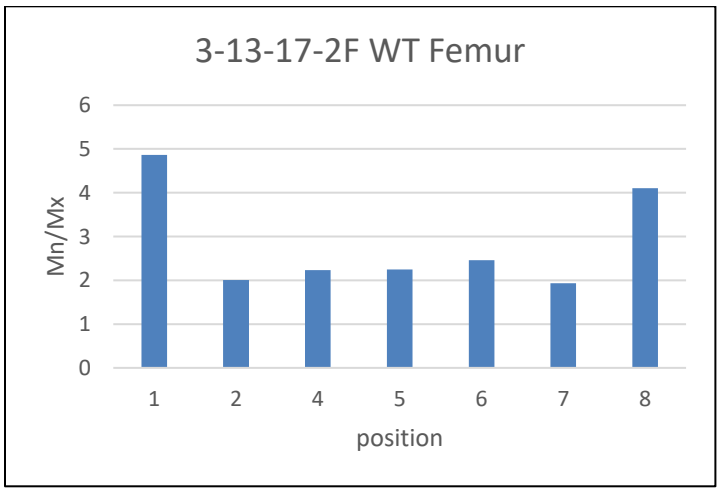

Figure 3-23(a)

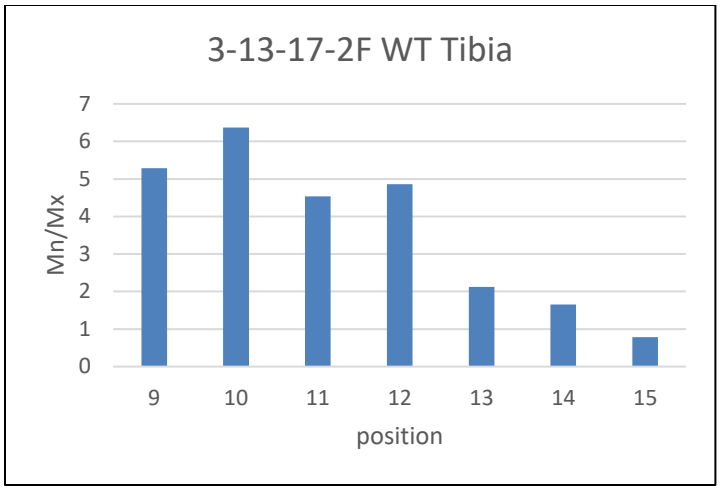

Figure 3-23(b)

Figure 3-23 Mn/Mx of bone sample 3-13-17-2F WT, (a) Femur (b) Tibia

3.12.1 FTIR Spectrum of 3-13-17-4F WT

This is another WT sample in the 3-13-17 age group. The variation in mineral wavenumbers was limited with a distinctive peak for each position (Figure 3-24). At position 2, the highest Mn/Mx was observed in this sample.

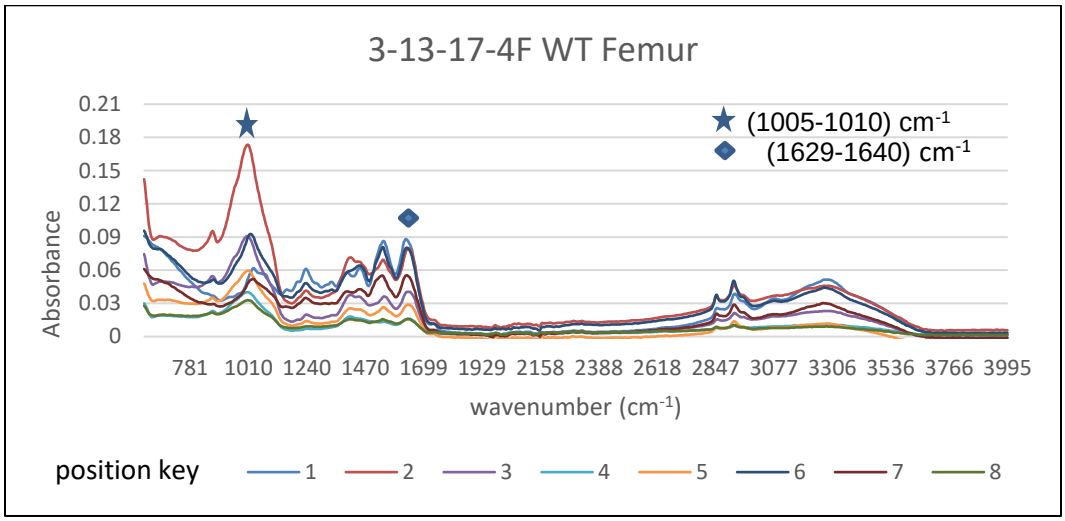

Figure 3-24(a)

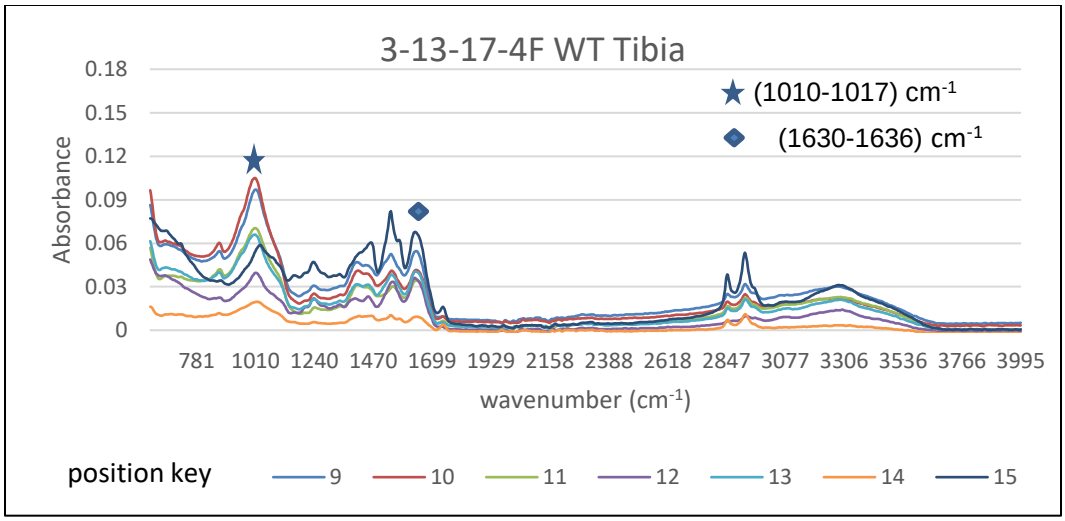

Figure 3-24(b)

Figure 3-24 FTIR spectra of bone sample 3-13-17-4F WT, (a) Femur (b) Tibia

3.12.2 Mn/Mx of 3-13-17-4F WT

In the femur, positions 1, 6 and 7, at which mineral peak broadened was observed, indicated lower Mn/Mx than the other positions (Figure 3-25a). The femur elevated Mn/Mx for most of the positions.

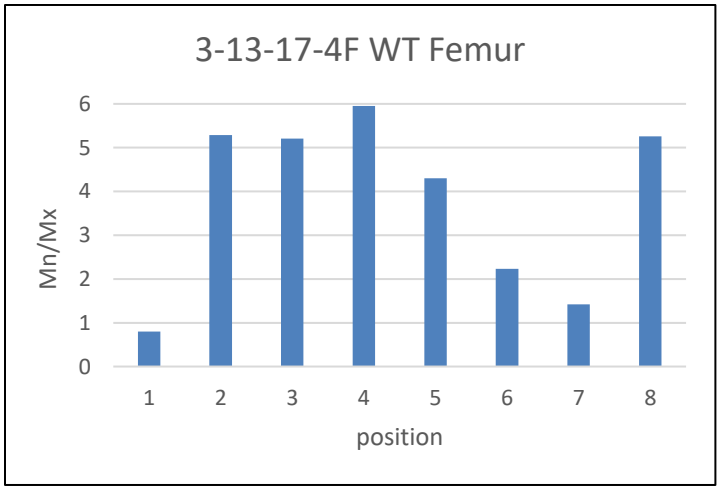

Figure 3-25(a)

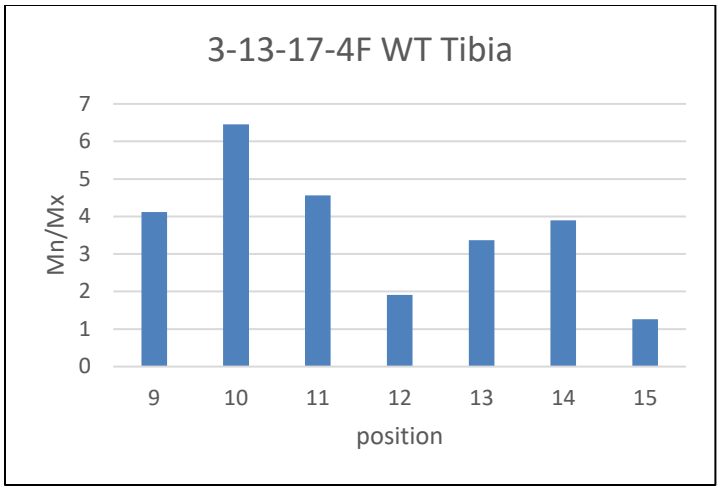

Figure 3-25(b)

Figure 3-25 Mn/Mx of bone sample 3-13-17-4F WT, (a) Femur (b) Tibia

3.13.1 FTIR Spectrum 4-7-17-1F KO

1F was a KO sample in the 4-7-17 age group. The variation in wavenumbers of mineral and matrix was limited with a distinctive spectrum for each position (Figure 3-26). Peak heights of CH2 and OH^- were negligible for the femur, and absorbance of the CH2 peak was high for position 15.

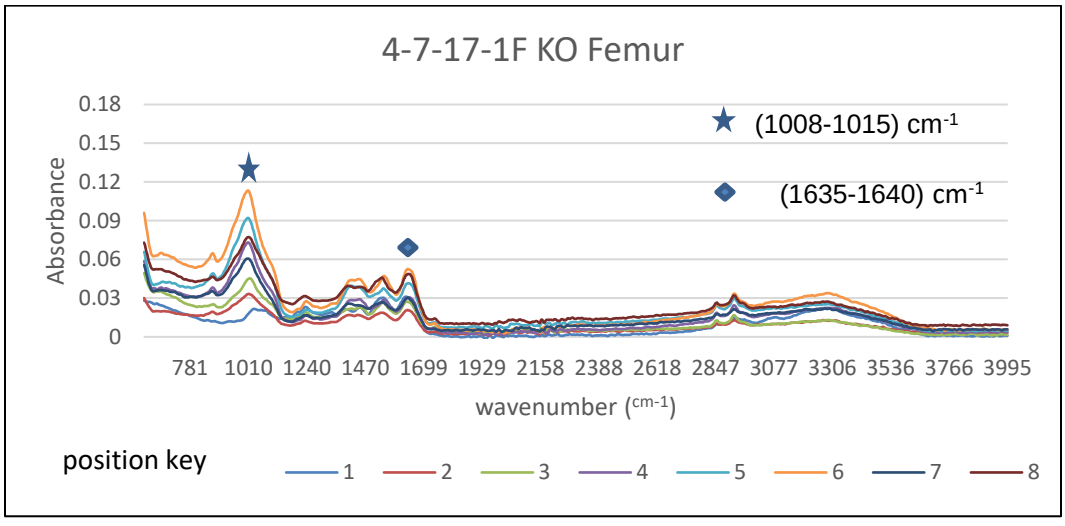

Figure 3-26(a)

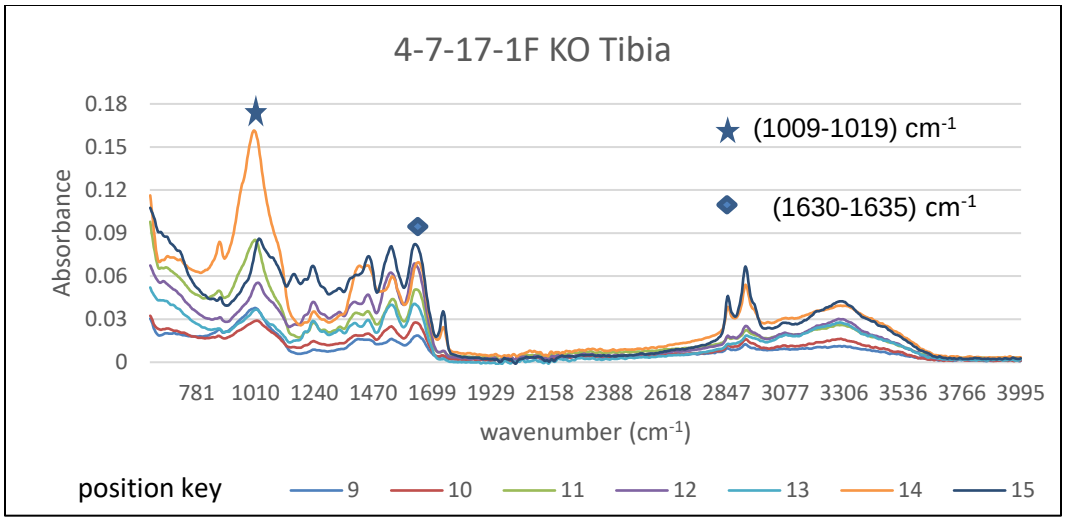

Figure 3-26(b)

Figure 3-26 FTIR spectra of bone sample 4-7-17-1F KO, (a) Femur (b) Tibia

3.13.2 Mn/Mx of 4-7-17-1F KO

Mn/Mx was a higher for all positions of the femur except position 1 (Figure 3-27). The difference in the median and mean was low for femur but large for the tibia. I observed elevated Mn/Mx for the positions at which the mineral absorbance peak was high.

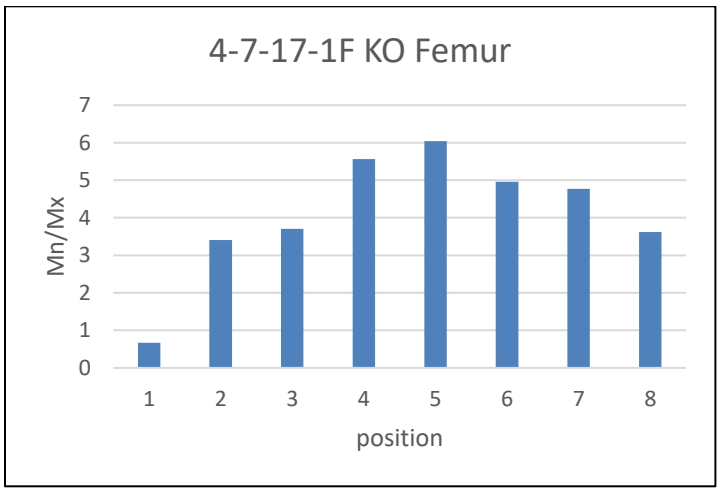

Figure 3-27(a)

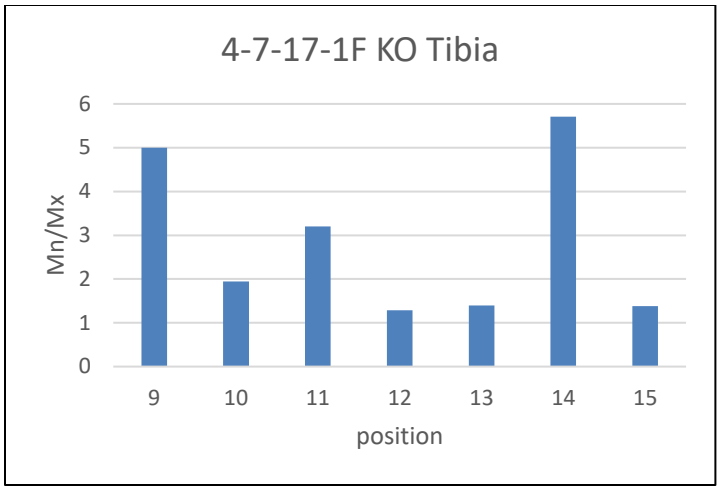

Figure 3-27(b)

Figure 3-27 Mn/Mx of bone sample 4-7-17-1F KO, (a) Femur (b) Tibia

3.14.1 FTIR Spectrum of 4-7-17-2F KO

2F was a KO sample in the 4-7-17 age group. The matrix wavenumber variation was least among all the samples from the 4-7-17 group (Figure 3-28). I observed distinctive peaks for both the mineral and matrix. We analyzed the highest absorbance for the mineral in the femur and for the matrix in the tibia.

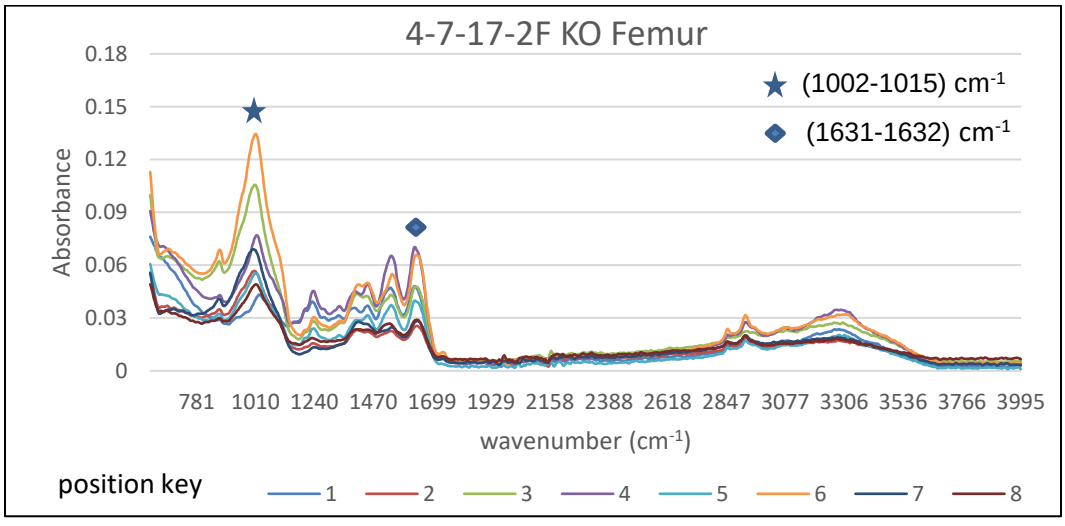

Figure 3-28(a)

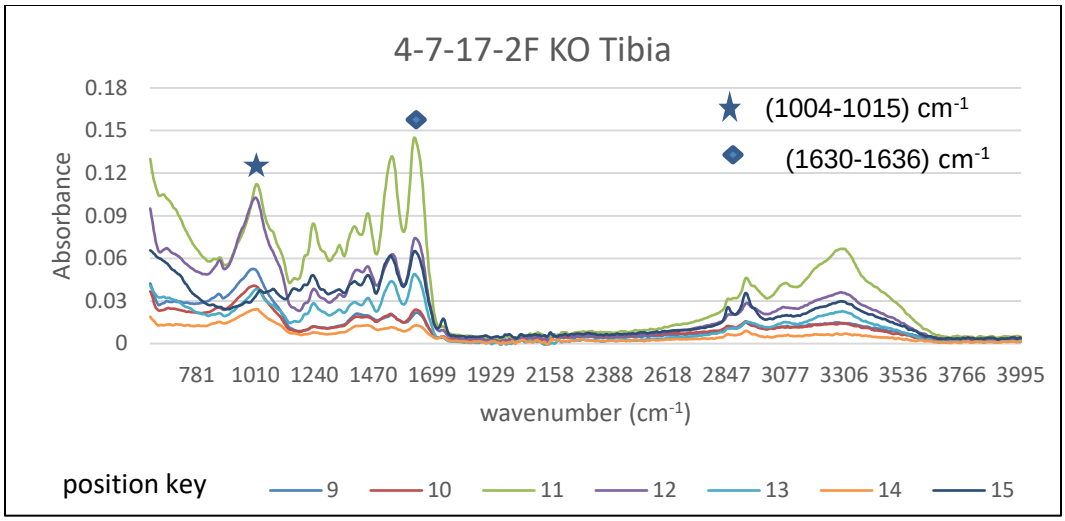

Figure 3-28(b)

Figure 3-28 FTIR spectra of bone sample 4-7-17-2F KO, (a) Femur (b) Tibia

3.14.2 Mn/Mx of 4-7-17-2F KO

Positions at which mineral and matrix absorbance peaks were the same indicated elevated Mn/Mx in the femur (Figure 3-29a). For the tibia, positions at which the absorbance peak of the mineral was higher than of matrix indicated elevated Mn/Mx.

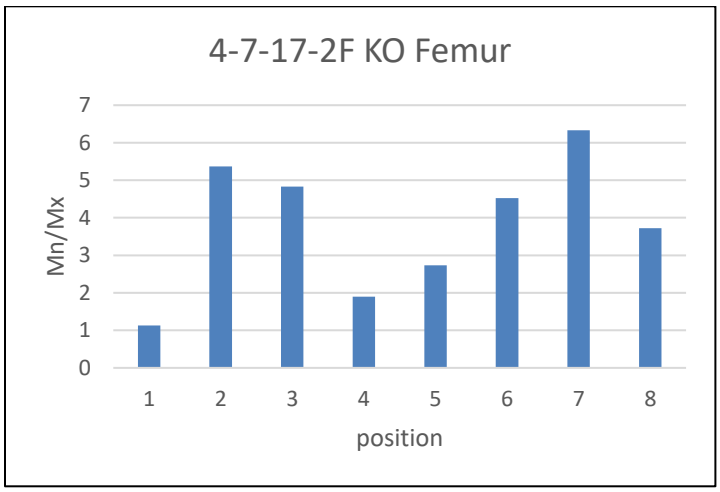

Figure 3-29(a)

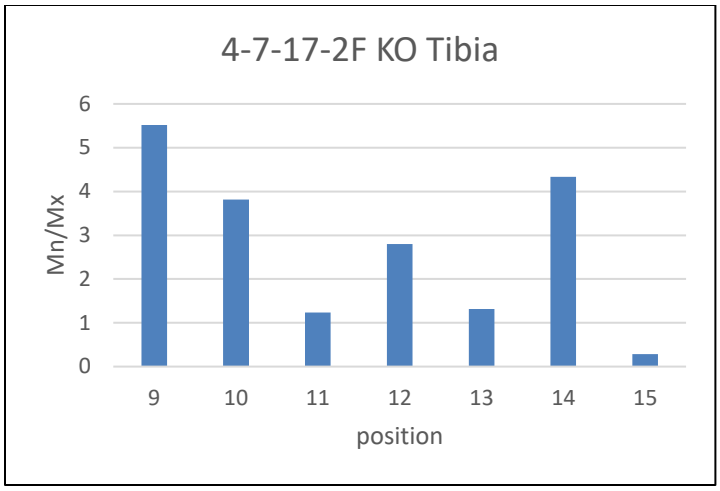

Figure 3-29(b)

Figure 3-29 Mn/Mx of bone sample 4-7-17-2F KO, (a) Femur (b) Tibia

3.15.1 FTIR Spectrum of 4-7-17-7F KO

Figure 3-30 illustrates position 2 in the femur and position 15 in the tibia had elevated absorbance peaks of CH_2. Typically, I observed the high CH_2 absorbance peaks at the end positions. The highest absorbance peak was observed in the mineral for the tibia.

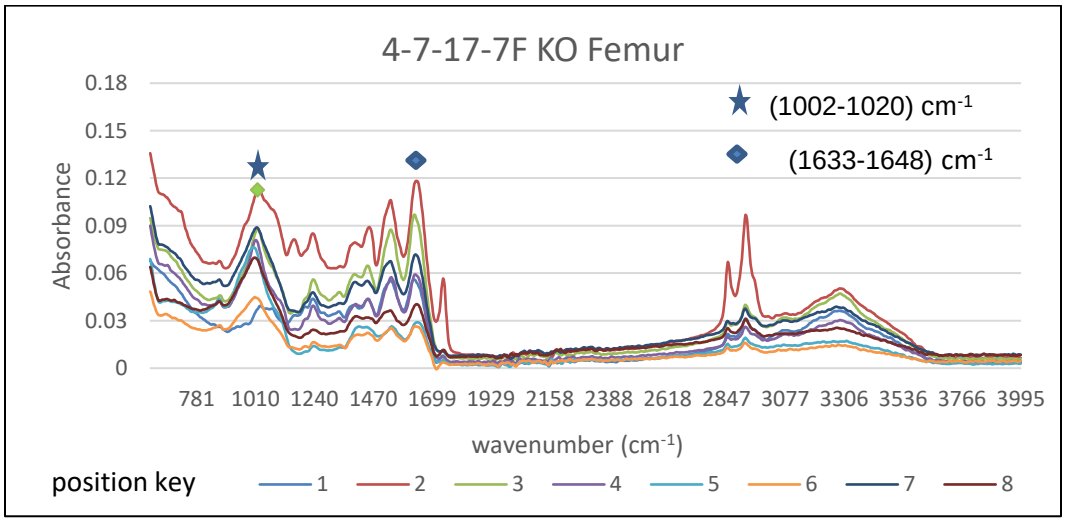

Figure 3-30(a)

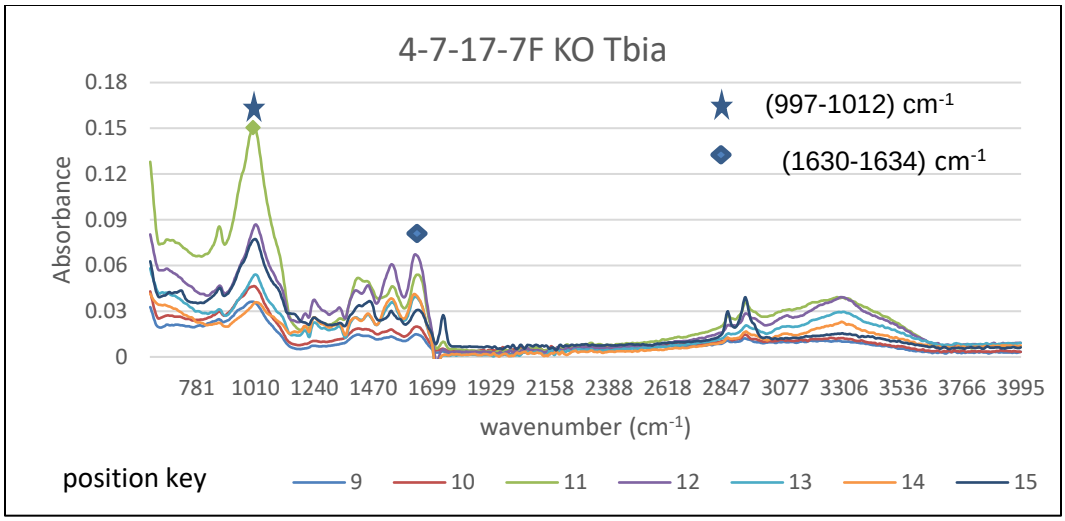

Figure 3-30(b)

Figure 3-30 FTIR spectra of bone sample 4-7-17-7F KO, (a) Femur (b) Tibia

3.15.2 Mn/Mx of 4-7-17-7F KO

For all the positions at which mineral had higher absorbance than matrix, the spectra indicated elevated Mn/Mx (Figure 3-31). Samples indicated higher Mn/Mx for positions in mid-diaphysis of the femur and tibia.

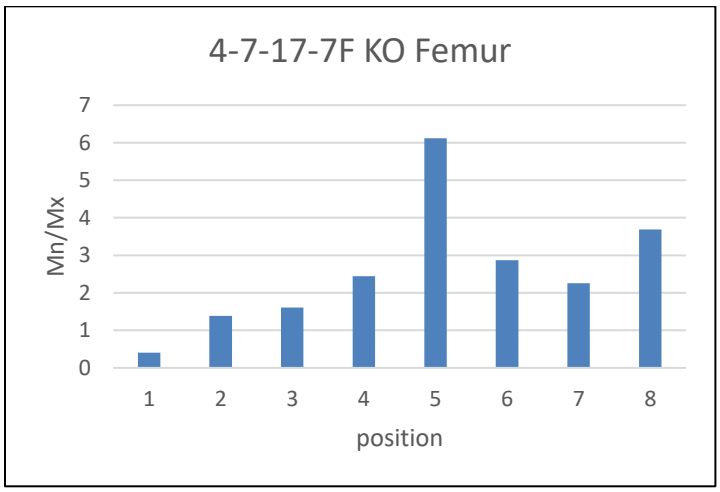

Figure 3-31(a)

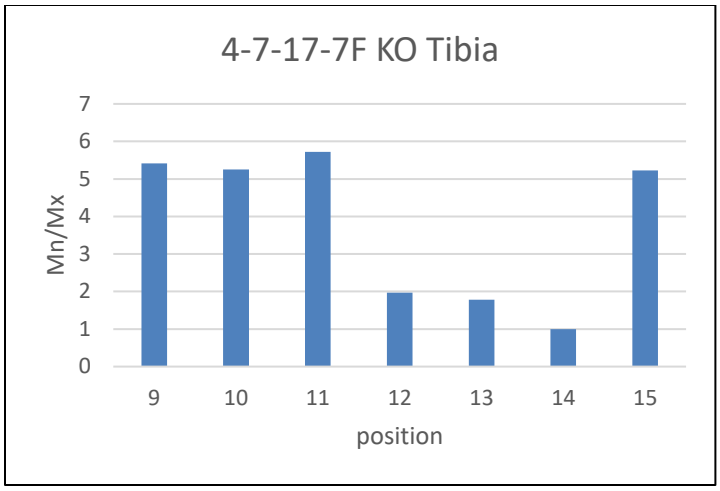

Figure 3-31(b)

Figure 3-31 Mn/Mx of bone sample 4-7-17-7F KO, (a) Femur (b) Tibia

Chapter 4 Results and Discussion

4.1 FTIR - Results and Discussion

I used the reflectance mode in which the light path reflected multiple times across the sample. By using this mode, the heterogeneous morphology was averaged in the sample. Although this method required slicing and polishing with a diamond saw, it was less disruptive to the microstructure than using the transmission mode. We obtained the spectra from OPUS software. With the help of Origin software, we implemented the baseline method on the spectra, which provided the integral area under the peak. Each peak was associated with the unique type of constituent present in the sample. We considered the phosphate peak, typically at 1015 cm^{-1} for the mineral, and amide I peak, usually at 1634 cm^{-1} for the matrix. The amount of each compound present in the sample was proportional to the area under that particular peak. Compounds such as carbonate and proline are of great importance in bone morphology and functionality, but due to their vibrational mode, they are not dominant in FTIR Spectra.

The femur and tibia were compared separately for the same age group. After obtaining a spectrum from a particular position on a bone, we calculated Mn/Mx for each position. To discriminate between the WT and KO rat bone, we compared calculated Mn/Mx in many ways. Firstly, for a single bone, we measured the Mn/Mx of each position and compared this measurement to the other positions in the femur and tibia along the length of the same bone. Secondly, we examined the same position for different samples for the femur and tibia. Thirdly, we examined the femur and tibia by age group. Comparisons using these methods were not conclusive. However, Mn/Mx of the mid-diaphysis was significant. We found Mn/Mx of the mid-diaphysis was higher in the KO than in the WT.

4.1.1 Mn/Mx of Femur Position for Different Samples

Bone is heterogeneous. We made each piece of femur and tibia for all the samples of equal sizes and corresponding positions. However, ensuring each piece was from the same position does not ensure the same composition of different samples. In this section, I compared WT and KO with a second method, in which I analyzed the same position on each sample. In this section, we covered Mn/Mx for the positions 1 through 8 on the femur, illustrated in Figure 4-1 through Figure 4-7.

Position 1 was from femur for all the samples (Figure 4-1). Position 1 was a part of the cancellous bone in which mineral concentration was reduced compared to matrix content [2, 3]. Mn/Mx was small for all the samples, as expected, except samples 3-10-17-7F and 3-13-17-2F, which indicated a high Mn/Mx for position 1. Samples that indicated exceptions were WT from different age groups.

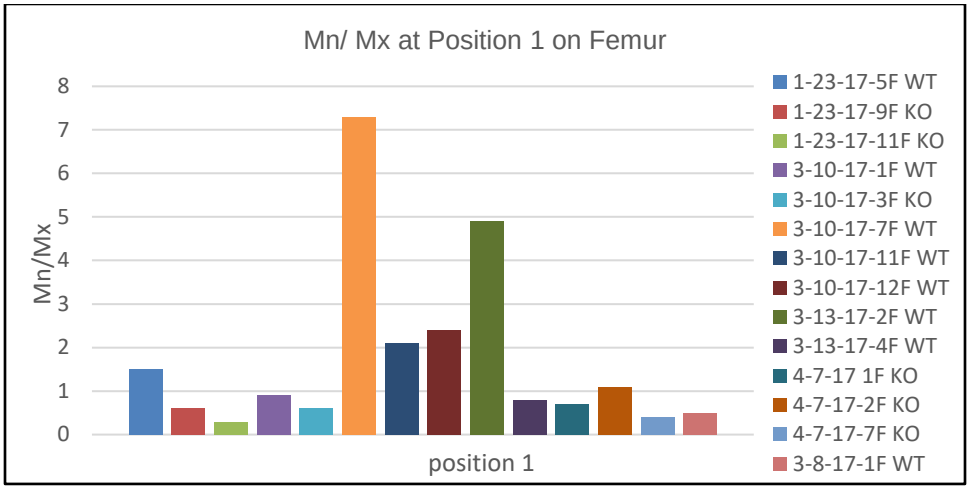

Figure 4-1 Mn/Mx of the femur at position 1 for all the samples

Position 2 was a part of the cancellous bone, and matrix content was lower than position 1. Mn/Mx was elevated for position 2 (Figure 4-2). Two WT samples, 1-23-17-5F and 3-13-17-4F, and one KO, 4-7-17-2F, indicated elevation in Mn/Mx was higher than expected, whereas Mn/Mx was lowered for the 3-10-17-12F WT sample.

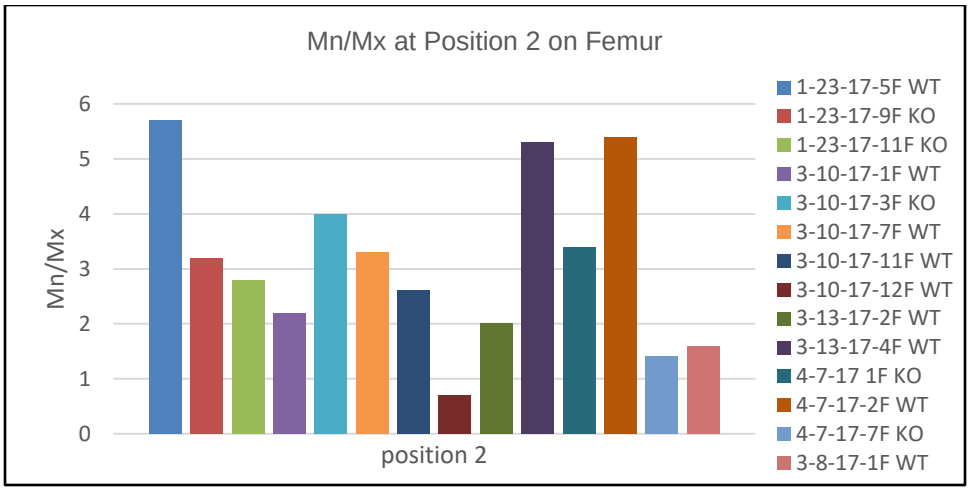

Figure 4-2 Mn/Mx of the femur at position 2 for all the samples

I could not obtain position 3 for every sample because of its structural difference and it is not taken into consideration for comparison Each sample indicated a limited range of Mn/Mx for position 4, (Figure 4-3). The mean of Mn/Mx for a position 4 was around 3.

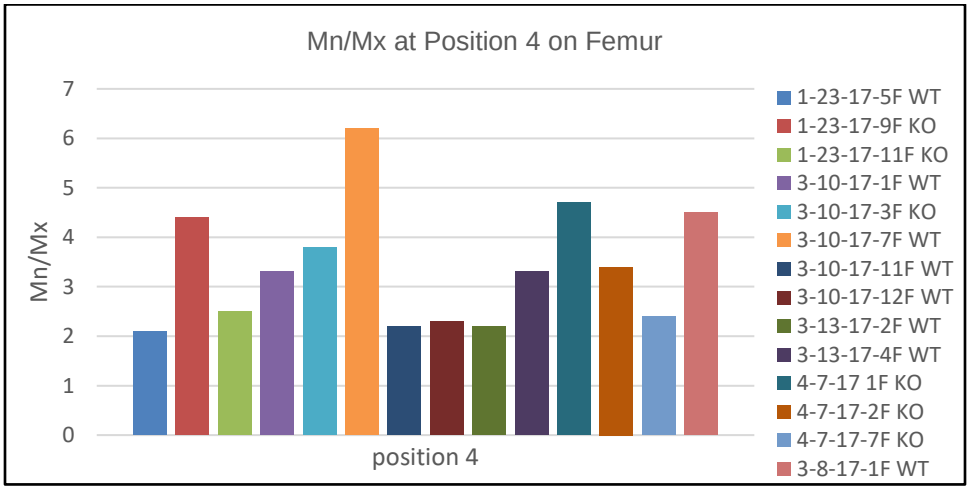

Figure 4-3 Mn/Mx of the femur at position 4 for all the samples

Mn/Mx was elevated for position 5 for all the samples. Position 5 was related to the mid-diaphysis of the samples in which crystal growth was mature. Figure 4-4 implies the same through increased Mn/Mx for most of the samples. The WT sample 3-10-17-12F

indicated a greater Mn/Mx decreased than position 3, whereas few samples indicated Mn/Mx near position 4.

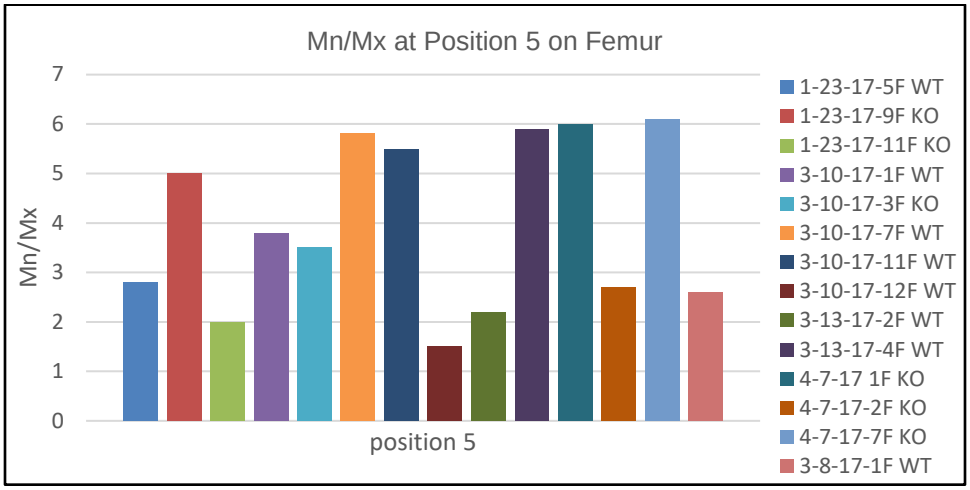

Figure 4-4 Mn/Mx of the femur at position 5 for all the samples

For position 6, Mn/Mx dropped from the position to the earlier range of ratio for the samples 1-23-17-9F, 3-10-17-11F, 3-13-17-4F, 4-7-17-1F and 4-7-17-7F (Figure 4-5). The sample 3-10-17-7F WT indicated an exception here as its Mn/Mx value increased compared to position 5. For all other samples, their Mn/Mx remained the same.

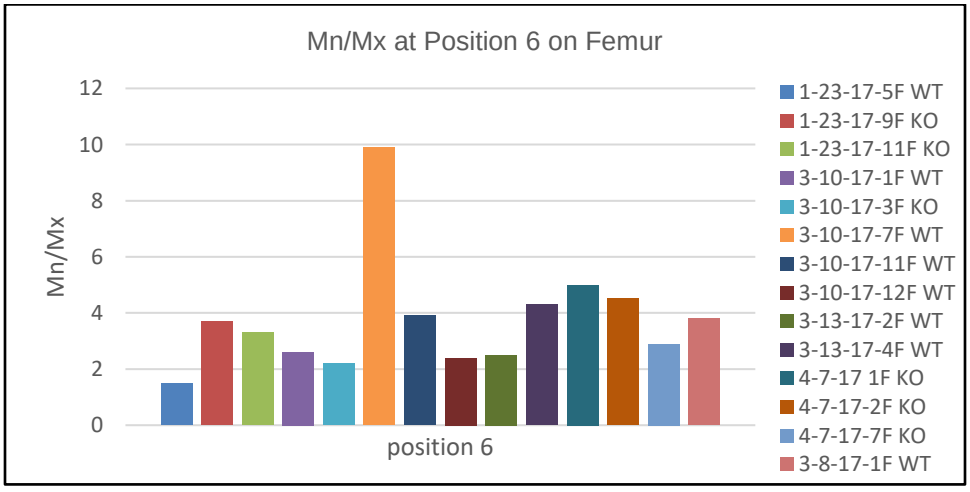

Figure 4-5 Mn/Mx of the femur at position 6 for all the samples

For position 7, Mn/Mx dropped into the range of 2 to 3 (Figure 4-6). Some samples (3-10-17-7F, 3-10-17-11F, and 4-7-17-1F) indicated Mn/Mx elevated to 5 to 6. The difference in elevation of Mn/Mx was high for sample 4-7-17-2F.

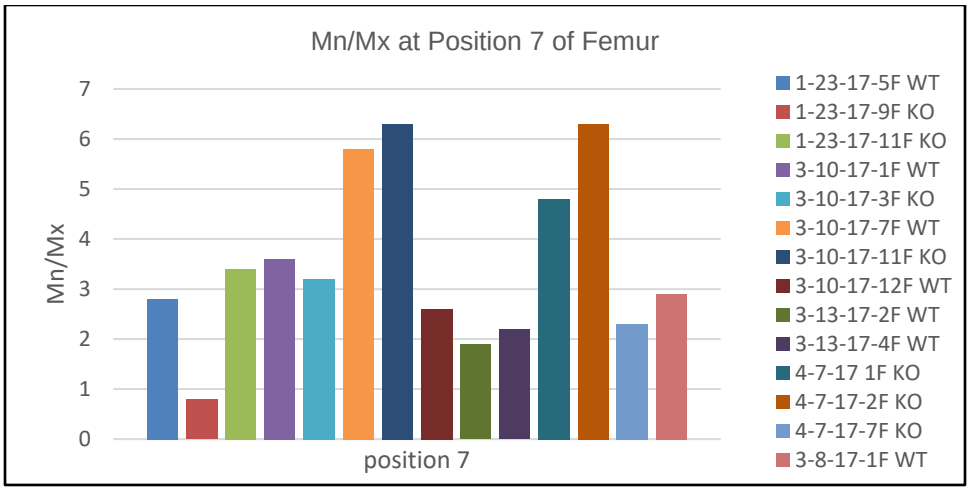

Figure 4-6 Mn/Mx of the femur at position 7 for all the samples

Mn/Mx for position 8 indicated consistent Mn/Mx compared to the other positions of the samples (Figure 4-7). Mn/Mx was high in sample 3-10-17-11F WT for position 8. Sample3-10-17 WT indicated different results compared to other samples for all positions in the femur.

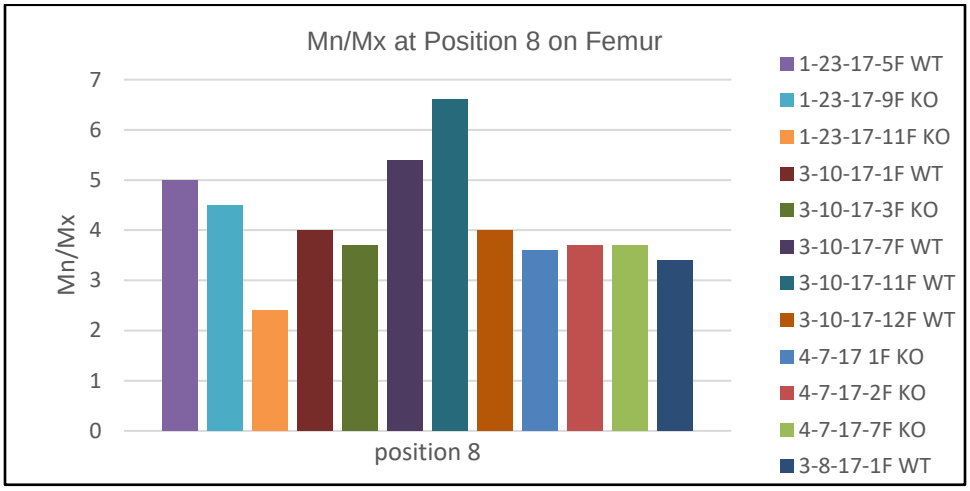

Figure 4-7 Mn/Mx of the femur at position 8 for all the samples

4.1.2 Mn/Mx of Tibia Position for Different Samples

This section compares the tibia to distinguish between WT and KO with varying age groups. We analyzed the same position on each sample. I covered Mn/Mx for the positions 9 to 15 on the tibia, illustrated in Figure 4-8 through Figure 4-14.

Position 9 is from cancellous bone. Figure 4-8 depicts the mean of Mn/Mx, which is in the range of 4 to 5. The WT sample 1-23-17-5F had the lowest Mn/Mx, whereas the KO sample 3-13-17-3F indicated the highest Mn/Mx among all the samples. Mn/Mx lowered for most of the samples from position 9 (Figure 4-8); WT samples 3-10-17-11F, 3-13-17-2F and 3-13-17-4F indicated elevated Mn/Mx.

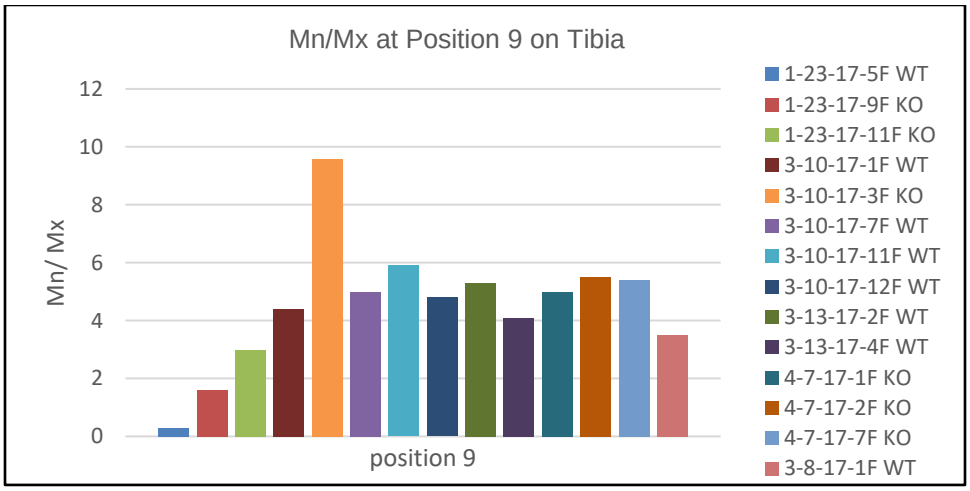

Figure 4-8 Mn/Mx of the tibia at position 9 for all the samples

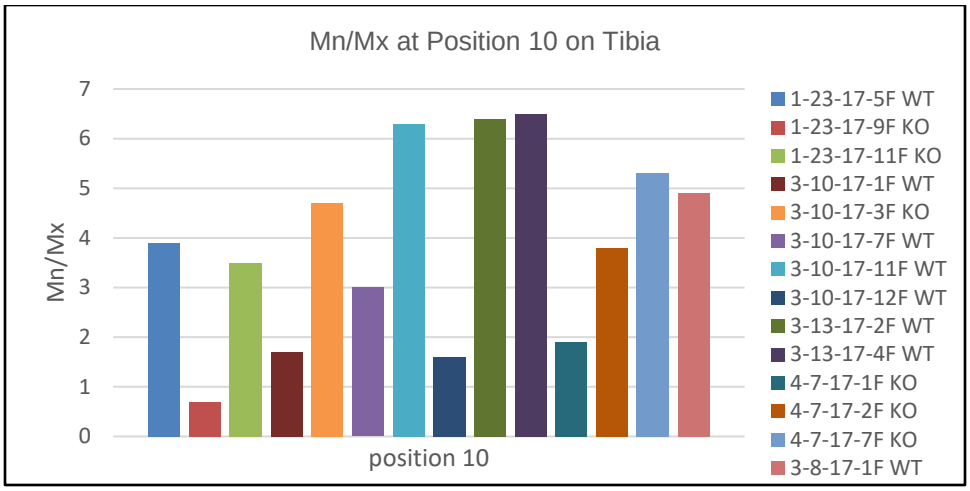

Figure 4-9 Mn/Mx of the tibia at position 10 for all the samples

Mn/Mx lowered for samples 3-13-17-2FWT, 3-13-17-4F WT and 4-7-17-2F KO from position 10 (Figures 4-9 and 4-10); the 3-10-17-11F WT sample had the same Mn/Mx as the previous position, and all other sample indicated increased Mn/Mx compared to the earlier position on tibia. Figure 4-10 illustrates, for position 11, the nature of the Mn/Mx change varied in comparison with position 11 over the samples. Sample 3-10-17-11F's Mn/Mx value was consistent with each position. For sample 1-23-17-9F, Mn/Mx increased through each position in the tibia. For samples 3-10-17-3F, 3-10-17-2F, 3-10-17-12F and 4-7-17-2F, Mn/Mx was elevated from earlier positions.

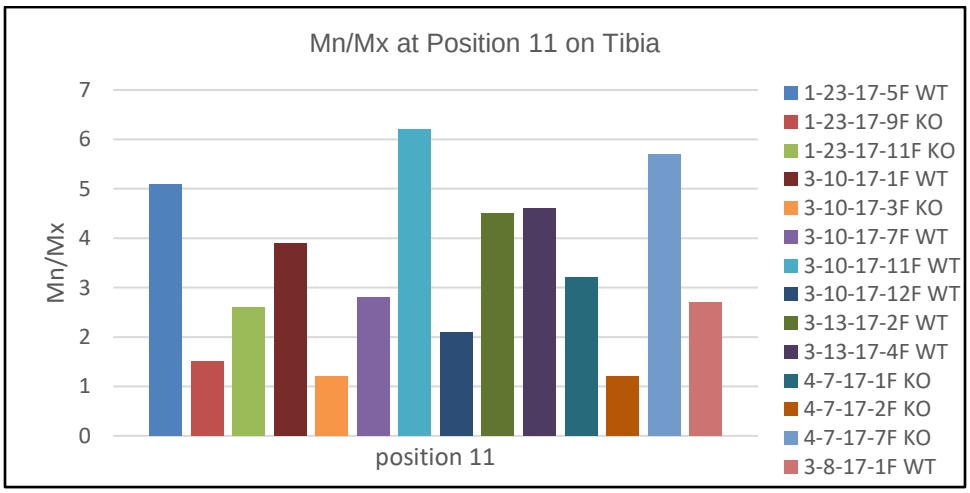

Figure 4-10 Mn/Mx of the tibia at position 11 for all the samples

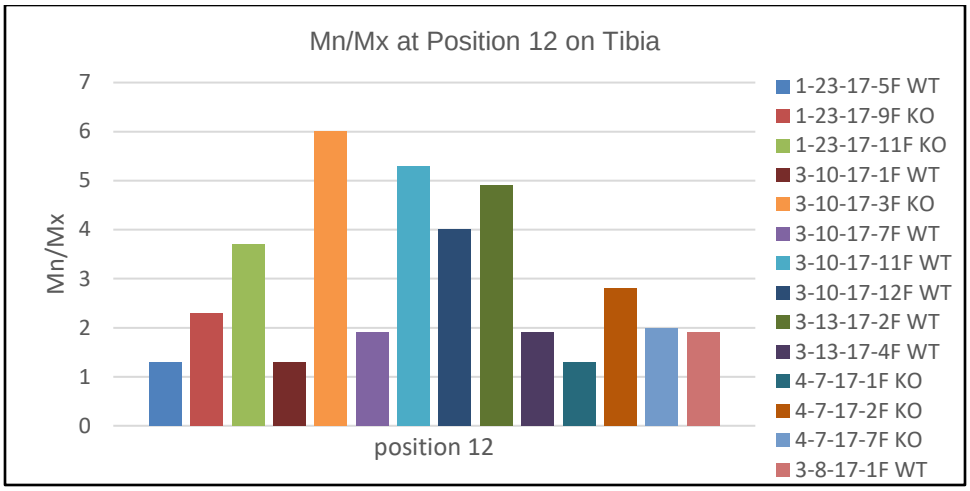

Figure 4-11 Mn/Mx of the tibia at position 12 for all the samples

The mean of Mn/Mx was around the value 2 to 3 for position 13 (Figure 4-12). Mn/Mx was consistent for sample 3-10-17-3F KO. Samples 3-10-17-7F, 3-13-17-4F and 3-8-17-1F were WTs and indicated increased Mn/Mx.

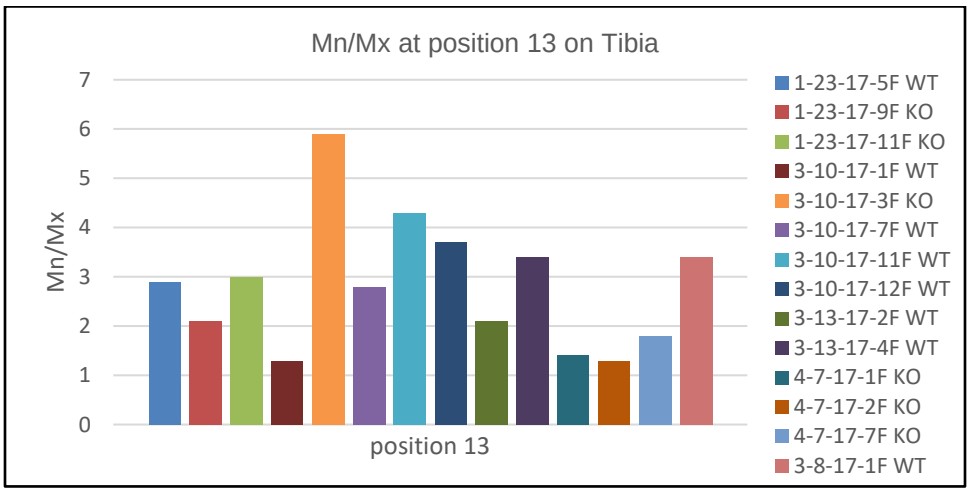

Figure 4-12 Mn/Mx of the tibia at position 13 for all the samples

Samples 1-23-17-5F WT, 3-13-17-4F WT, 4-7-17-1F and 4-7-17-2F, indicated elevated Mn/Mx from earlier positions (Figure 4-13). Mn/Mx was consistent with a value of 6 for sample 3-10-17-3F in the tibia. Due to the structural disruption of the sample, we could not obtain position 14 for sample 3-10-17-1F, while handling it.

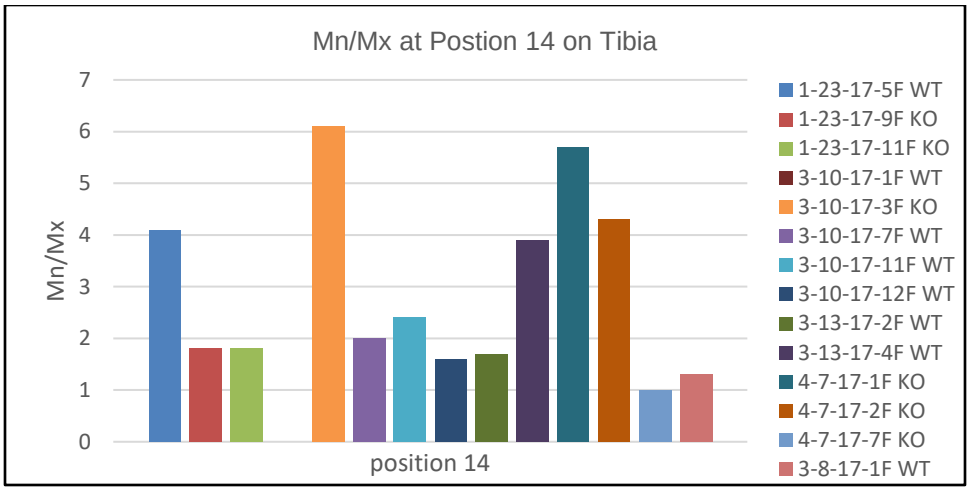

Figure 4-13 Mn/Mx of the tibia at position 14 for all the samples

It is observed, samples 3-13-17-2F WT, 4-7-17-1F KO and 4-7-17-2F KO had lowered Mn/Mx values and consistency for a sample 3-10-17-3F KO. Position 15 for samples 1-23-17-5F, 3-10-17-1F and 3-10-17-12F was not obtained due to the samples' structural disruption while handling those.

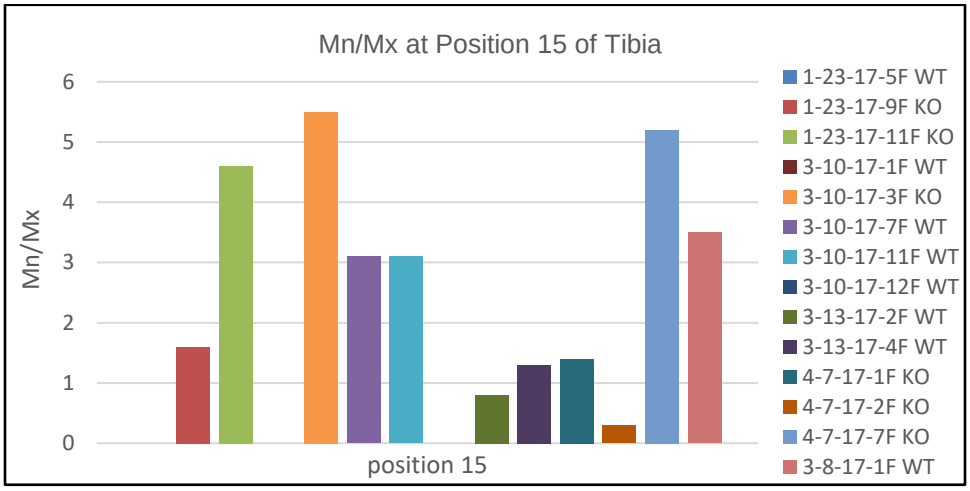

Figure 4-14 Mn/Mx of the tibia at position 15 for all the samples

4.1.3 Mn/Mx of Femur Age-Group for Different Samples

Same age grouping was a substantial basis to compare WT and KO, though each age group did not have a mixture of WT and KO samples. The relatively low number of KO rat samples available was due to the early stage of development in breeding the KO colonies. The altered gene causes a low survival rate among rat pups because, in addition to affecting bone growth, there appears to be disruptions in lung and heart growth.

In this section, the comparisons for the femur, illustrated in Figure 4-15 through Figure 4-20, are discussed. There were, in total, seven spectra on each femur leading to seven different values of Mn/Mx. I plotted bar charts of the Mn/Mx mean and error bars represent the standard deviation of those seven measurements for each sample.

Figure 4-15 illustrates the 1-23-17 group is the oldest among all the samples. However, mineral properties do not depend upon animal age, but on crystal age. This group had one WT (5F) and two KO (9F & 11F). The mean and standard deviation for 5F WT and 9F KO were approximately the same and were higher than 11F KO (Figure 4-15).

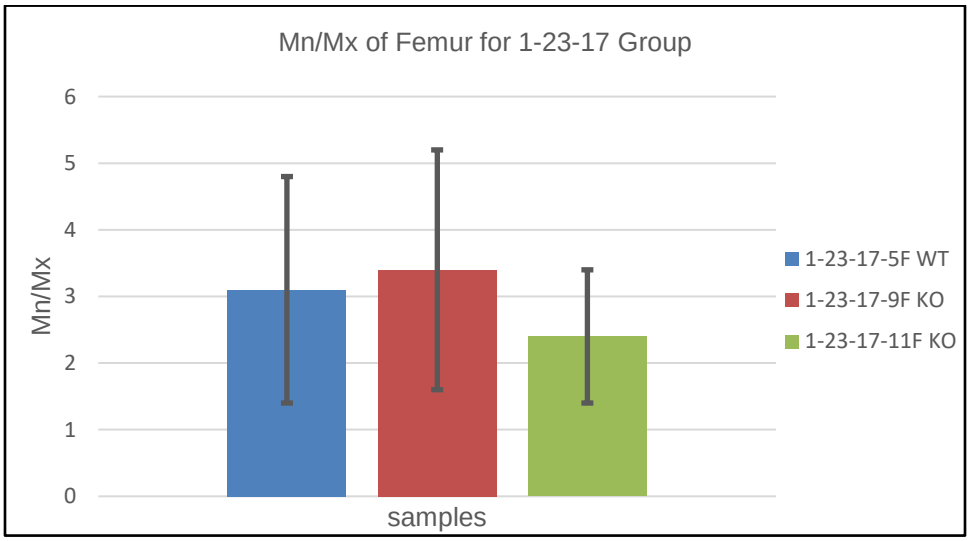

Figure 4-15 Mn/Mx of the femur for age group 1-23-17, error bars represent measurement on seven different positions on femur of each sample

The 3-10-17 group had four WT (1F, 7F, 11F and 12F) and one KO (3F) samples, (Figure 4-16). The standard deviation was the same for the three WT (1F, 7F, and 11F)

samples and 3F KO and 12F WT. We saw exceptionally high Mn/Mx for 7F WT in the femur. In this age group, KO had lower standard deviation than the WT samples.

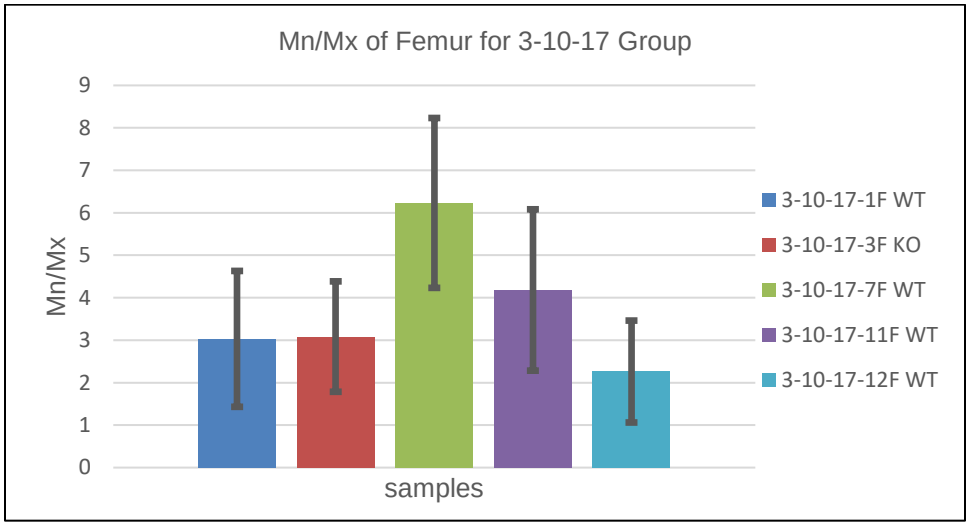

Figure 4-16 Mn/Mx of the femur for the age group 3-10-17, error bars represent measurement on seven different positions on femur of each sample

This age group had only WT samples that had a difference in their means and standard deviations of Mn/Mx (Figure 4-17).

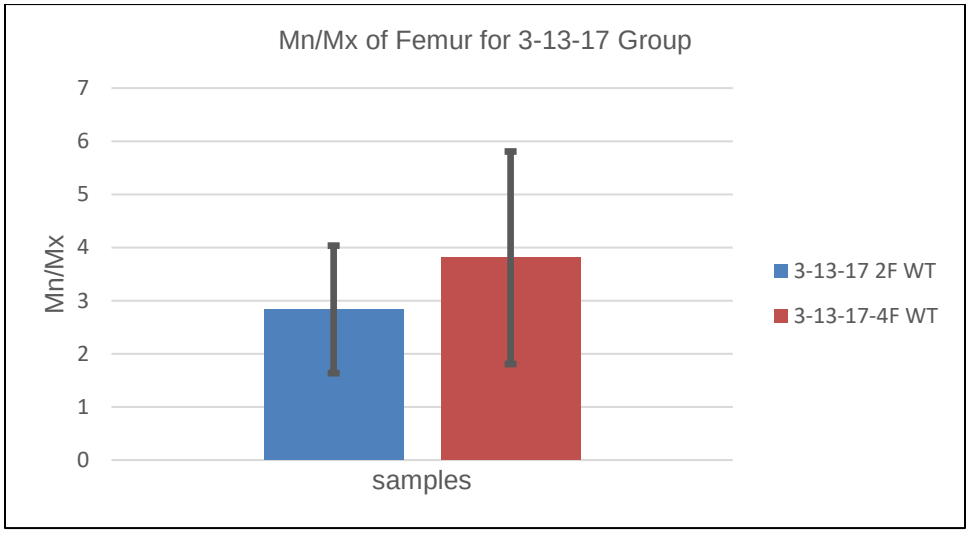

Figure 4-17 Mn/Mx of the femur for the age group 3-13-17, error bars represent measurement on seven different positions on femur of each sample

The 4-7-17 age group had all three KO samples in which the standard deviation of Mn/Mx was equal (Figure 4-18). There was a slight difference in their means of Mn/Mx.

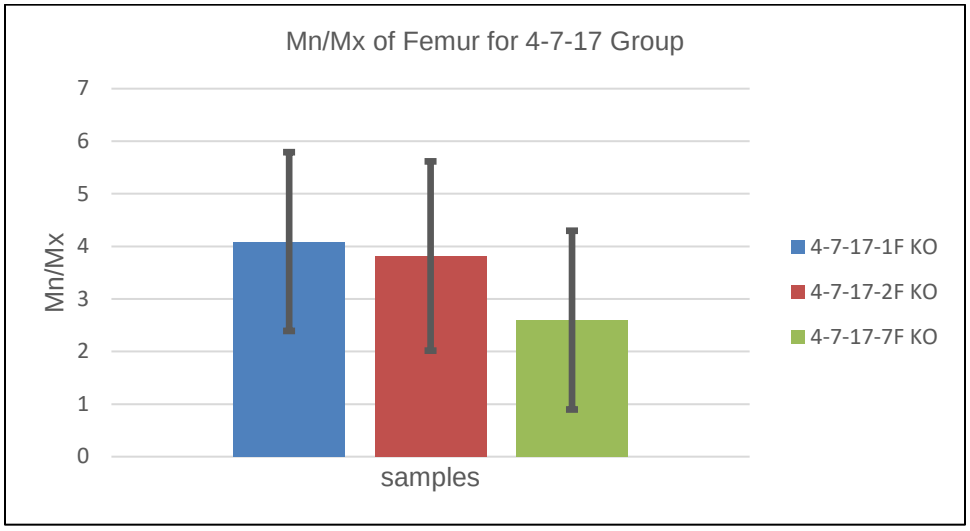

Figure 4-18 Mn/Mx of the femur for the age group 4-7-17, error bars represent measurement on seven different positions on femur of each sample

For the 3-8-17 age group, we had just one sample, a WT with a mean of 2.9 and standard variation of 1.2 (Figure 4-19). There was no other sample to compare the parameters.

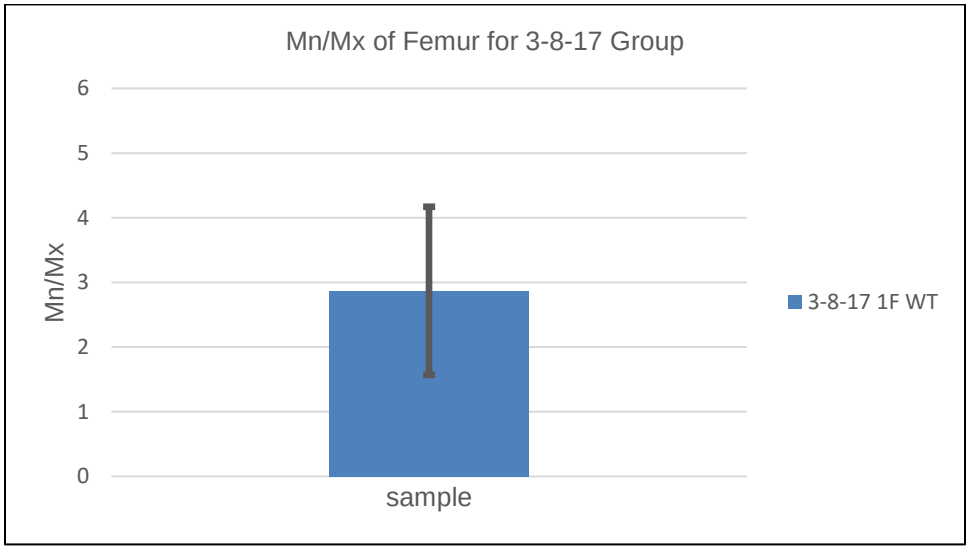

Figure 4-19 Mn/Mx of the femur for the age group 3-8-17, error bars represent measurement on seven different positions on femur of each sample

The mean for all the samples was around 3. Some KO samples indicate higher means, whereas some had lower means of Mn/Mx (Figure 4-20). There was a variation in standard deviation for both WT and KO samples, and this variation was greater than the difference in the mean.

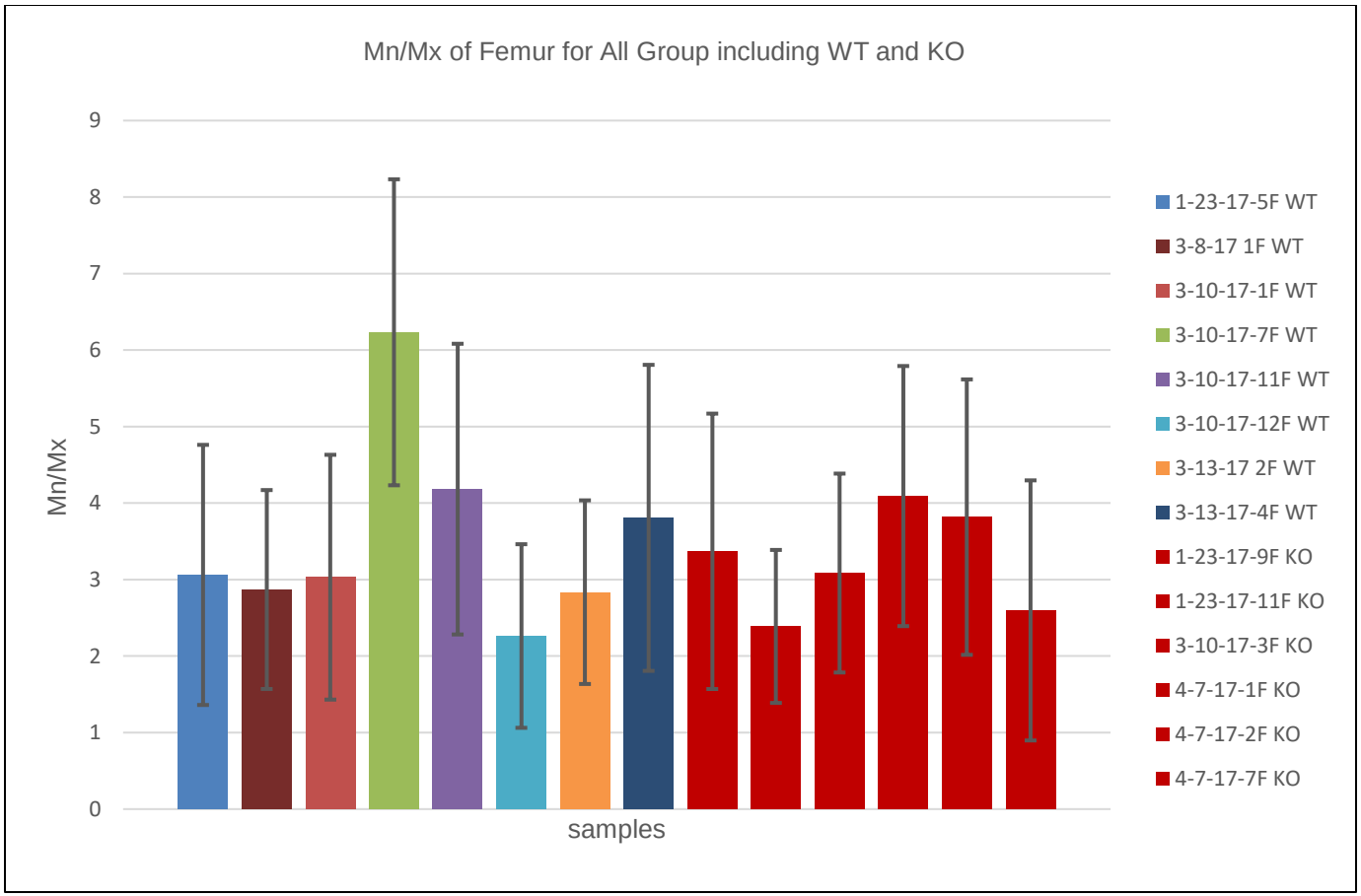

Figure 4-20 Mn/Mx of the femur for all the samples, error bars represent measurement on seven different positions on femur of each sample

(The red bars represent KO rats and rest are WT samples)

4.1.4 Mn/Mx of Tibia Age-Group for Different Samples

Comparing the tibia sections is a third method of comparison by age groupings. The tibia is believed to be more important in the etiology of the limb and foot malformations than the femur. Comparing WT and KO is important, though each age group does not have a mixture of WT and KO samples. Comparisons for the tibia are illustrated in Figure 4-21 through Figure 4-26. There were, in total, seven spectra on each tibia leading to seven different values of Mn/Mx. I plotted bar charts of the Mn/Mx mean and error bars represent the standard deviation of those seven measurements for each sample.

The WT sample had a sizeable standard deviation compared to the other two KO samples (Figure 4-21). The mean for 9F KO was lower than the other two samples. 5F WT and 11F KO had means around 3.

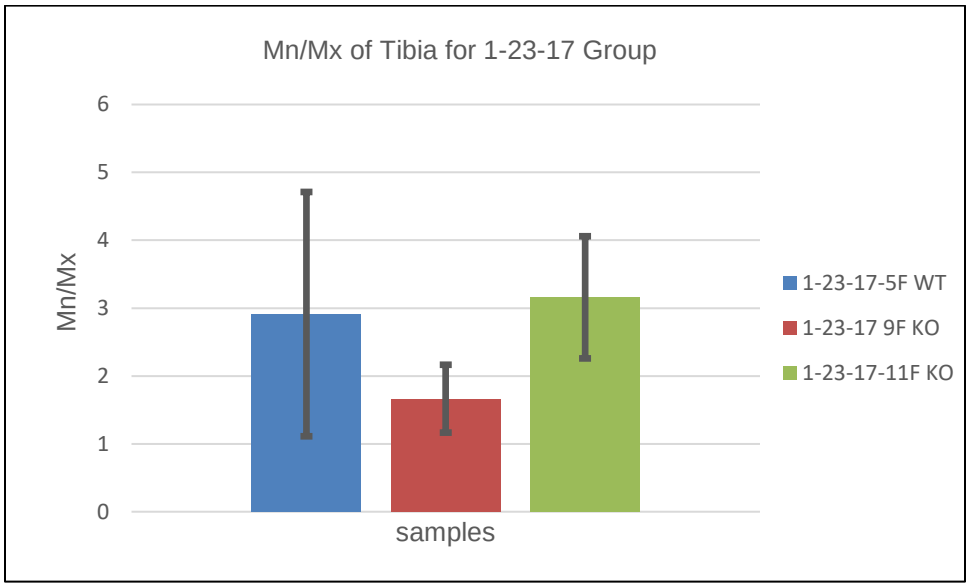

Figure 4-21 Mn/Mx of the tibia for the age group 1-23-17, error bars represent measurement on seven different positions on tibia of each sample

A KO sample had a higher mean and standard deviation for Mn/Mx than the WT samples in this group (Figure 4-22). Both samples indicated the same mean but different standard deviations of Mn/Mx (Figure 4-23).

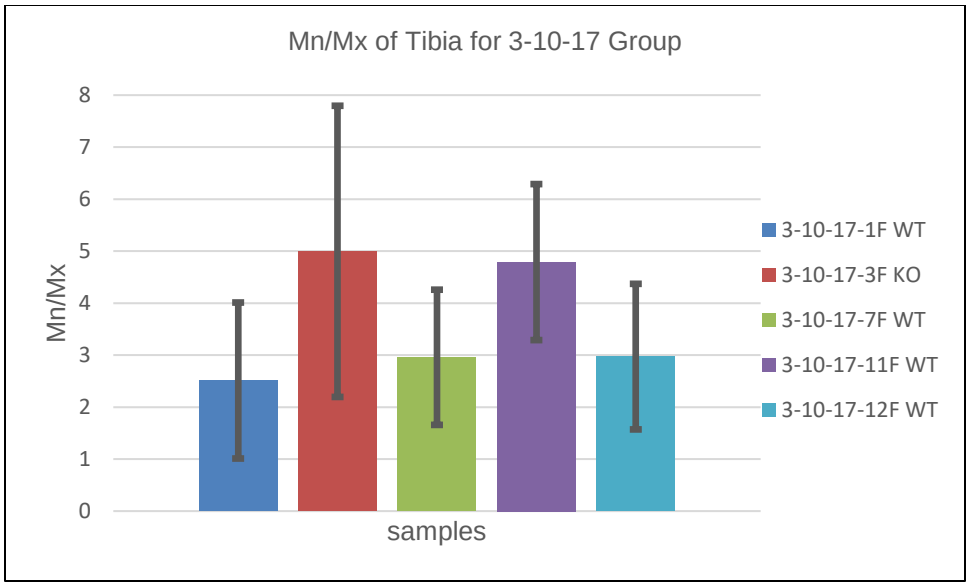

Figure 4-22 Mn/Mx of the tibia for the age group 3-10-17, error bars represent measurement on seven different positions on tibia of each sample

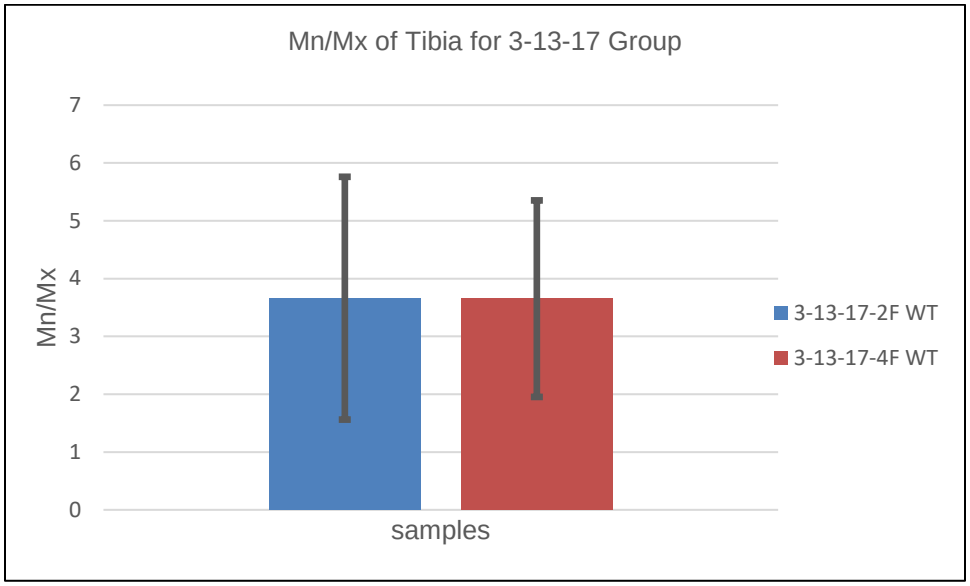

Figure 4-23 Mn/Mx of the tibia for the age group 3-13-17, error bars represent measurement on seven different positions on tibia of each sample

All KO samples had nearly same mean and standard deviation of Mn/Mx (Figure 4-24). I saw the same effects when fstl 5 was disabled in the rat samples. Illustrated in

Figure 4-25, the tibia of the 3-8-17 age group indicated the value of the mean was equal to 3 with a standard deviation of 1.5.

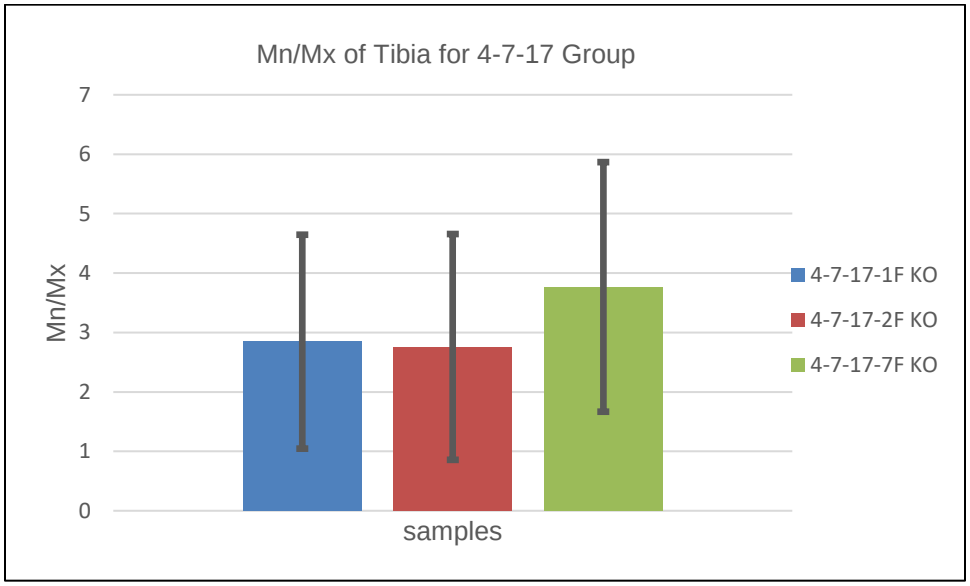

Figure 4-24 Mn/Mx of the tibia for the age group 4-7-17, error bars represent measurement on seven different positions on tibia of each sample

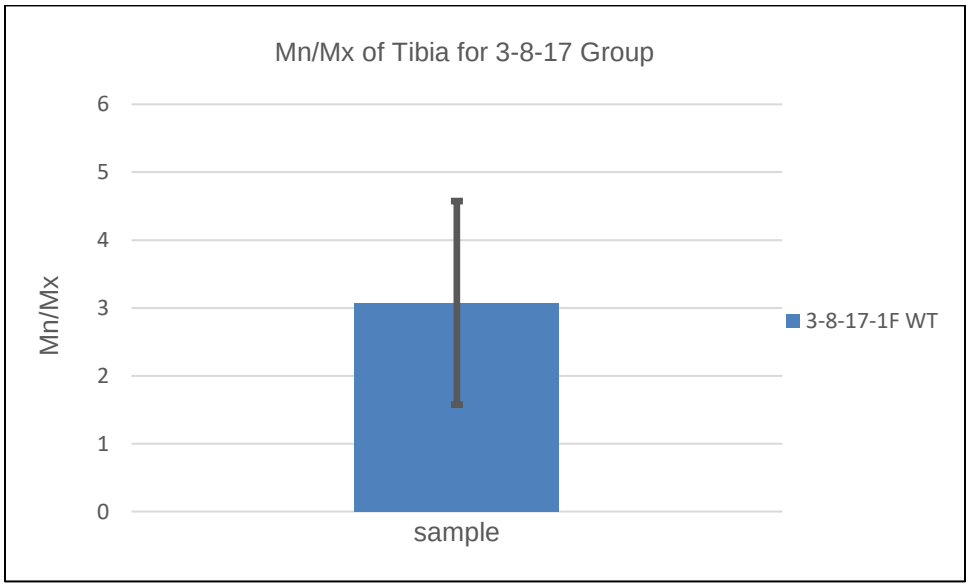

Figure 4-25 Mn/Mx of the tibia for the age group 3-8-17, error bars represent measurement on seven different positions on tibia of each sample

The tibia of the 1-23-17-5F KO sample showed the lowest value for the mean and standard deviation of Mn/Mx among all the samples. Six samples indicated the mean of Mn/Mx was above 3. The standard deviation of KO samples was higher than WT samples (Figure 4-26).

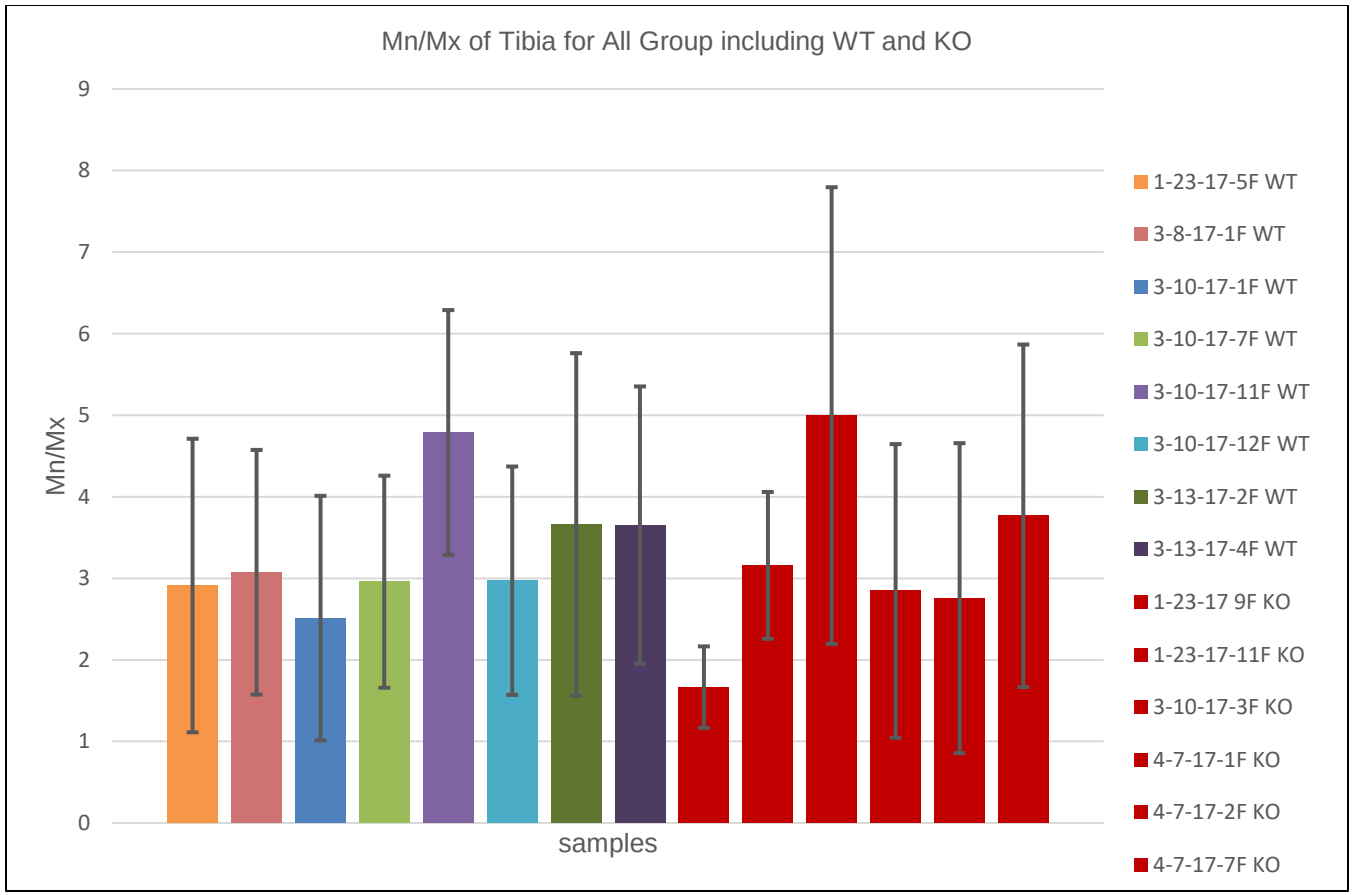

Figure 4-26 Mn/Mx of the tibia for all the sample, error bars represent measurement on seven different positions on tibia of each sample

(the red bars represents KO and the rest are WT rat samples)

4-1.5 Mn/Mx for Mid-Diaphysis Region of the Bone for Different Samples

The mid-diaphysis region is the most mature region of bone with the highest crystal growth, so we considered the middle portion of femur and tibia as parameters for comparison of WT and KO. I obtained a single spectrum on the mid-diaphysis region of both the femur and tibia, which leads to the single value of Mn/Mx for each of femur and tibia. In this section, I compared the averaged Mn/Mx measurement based on the WT and KO of each age group. Same type of samples was combined in a group.

For the age group 1-23-17, Mn/Mx was higher in KO than WT for the mid-diaphysis region (Figures 4-27 and 4-28). There were two KO samples in this age group. We considered the average with standard deviation range of those samples. The mean of Mn/Mx was higher in KO samples than in WT samples.

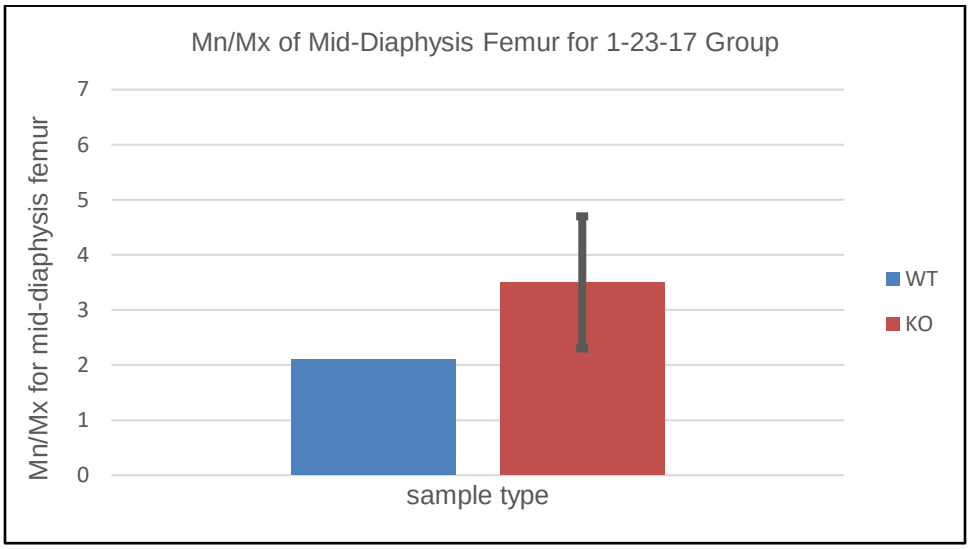

Figure 4-27 Mn/Mx of the femur on the mid-diaphysis region for the age group 1-23-17, error bar represents measurement of two KO samples in the 1-23-17 group

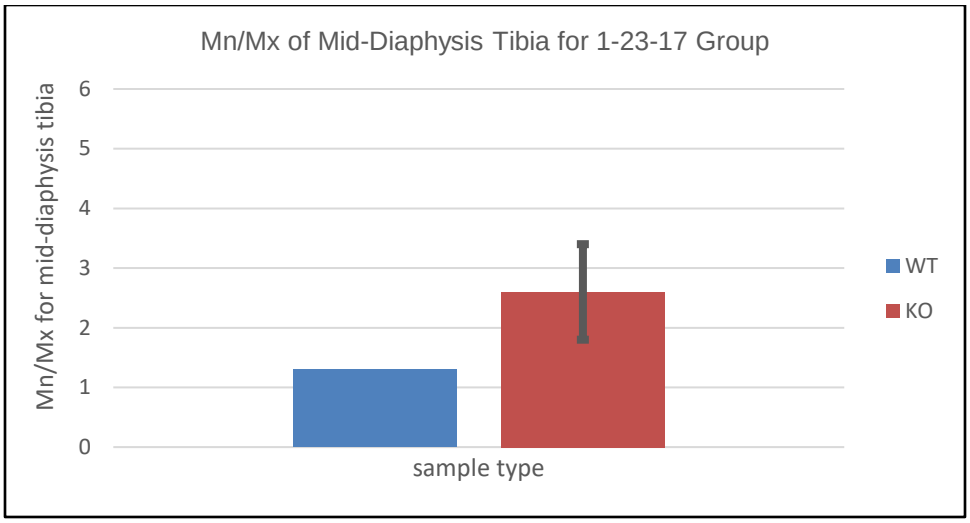

Figure 4-28 Mn/Mx of the tibia on the mid-diaphysis region for the age group 1-23-17, error bar represents measurement of two KO samples in the 1-23-17 group (Where the error bar is missing, there was no variable parameter)

The 3-10-17 group had four WT and one KO sample. We calculated the mean and standard deviation for these four WT samples. For the femur, WT had a Mn/Mx ratio in the mid-diaphysis, but the standard deviation was significant for WT (Figure 4-29). For the tibia, Mn/Mx was higher in KO than in WT; in this case, the standard deviation in WT's Mn/Mx was low (Figure 4-30).

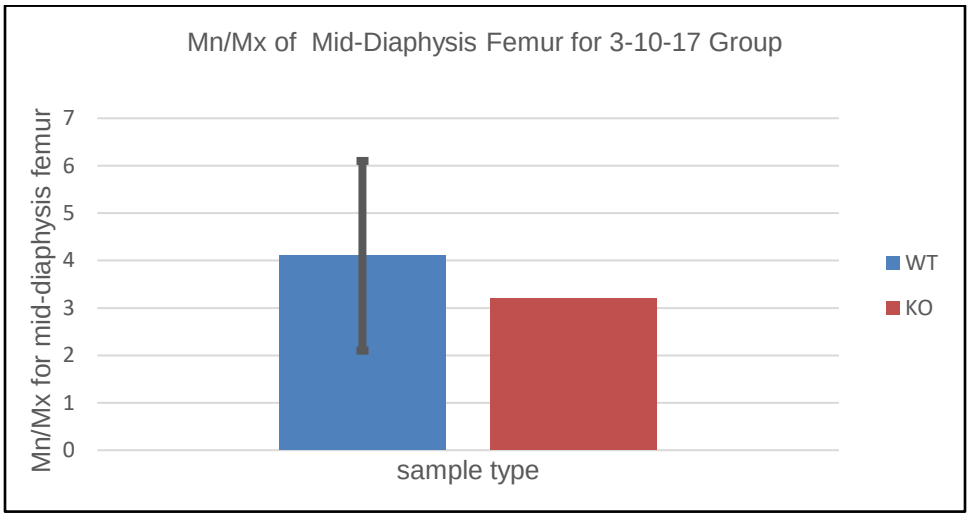

Figure 4-29 Mn/Mx of the femur on the mid-diaphysis region for the age group 3-10-17, error bar represents measurement of four WT samples in the 3-10-17 group

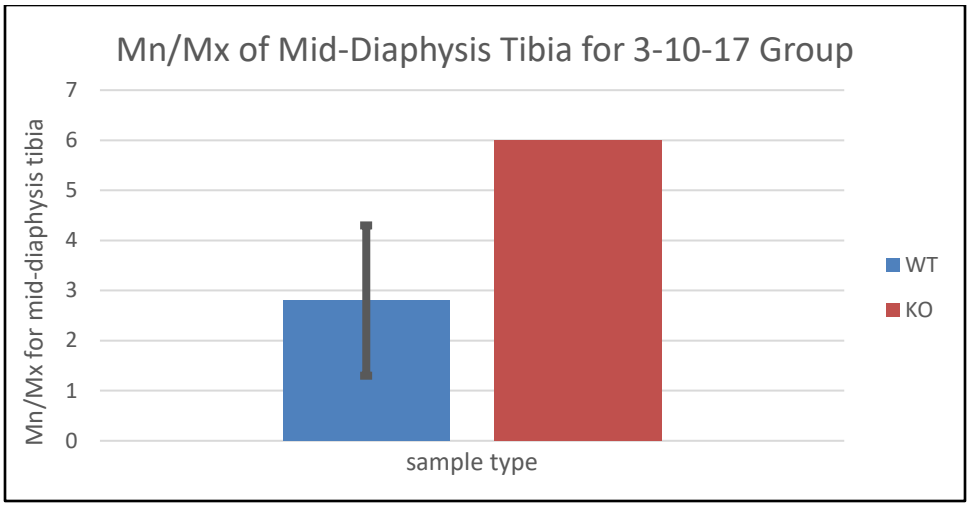

Figure 4-30 Mn/Mx of the tibia on the mid-diaphysis region for the age group 3-10-17, error bar represents measurement of four WT samples in the 3-10-17 group

(Where the error bar is missing, there was no variable parameter)

The 3-13-17, 4-7-17, and 3-8-17 groups did not include a comparison between WT and KO samples. I plotted all means of Mn/Mx with their standard deviation for the mid-diaphysis region (Figure 4-31, 4-32 and 4-33). For group 3-13-17, Mn/Mx was higher in the tibia than the femur, but the standard deviation was larger in tibia than the femur (Figure 4-31).

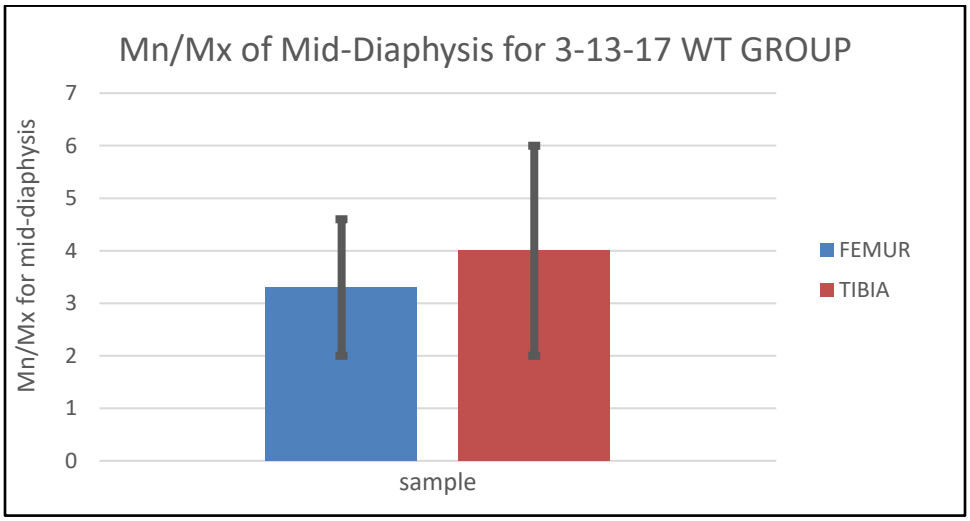

Figure 4-31 Mn/Mx of the femur and tibia on the mid-diaphysis region for the age group 3-13-17 WT, error bars represent two observations each on the femur and tibia

For the age group 4-7-17, as illustrated in Figures 4-32 and 4-33, Mn/Mx was lower in the tibia than in the femur.

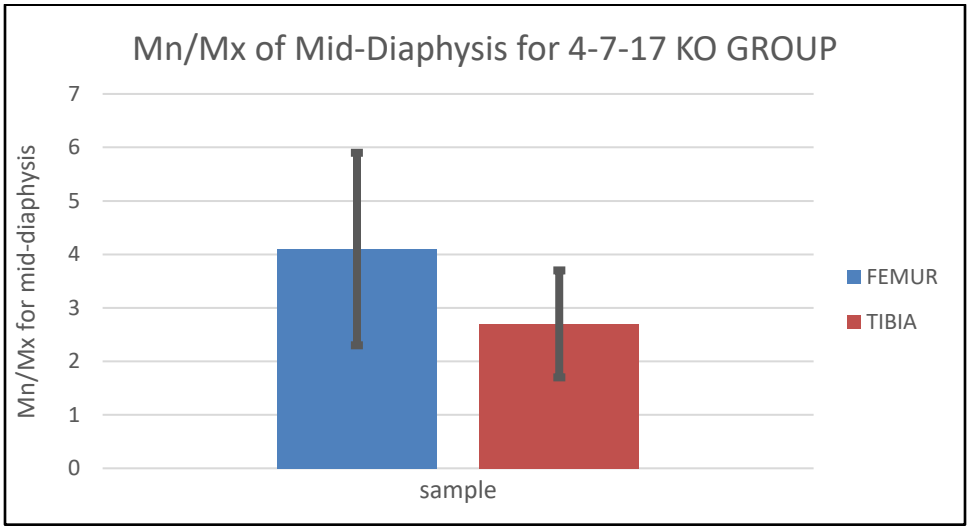

Figure 4-32 Mn/Mx of the femur and tibia on the mid-diaphysis region for the age group 4-7-17 KO, error bars represent two observations each on the femur and tibia

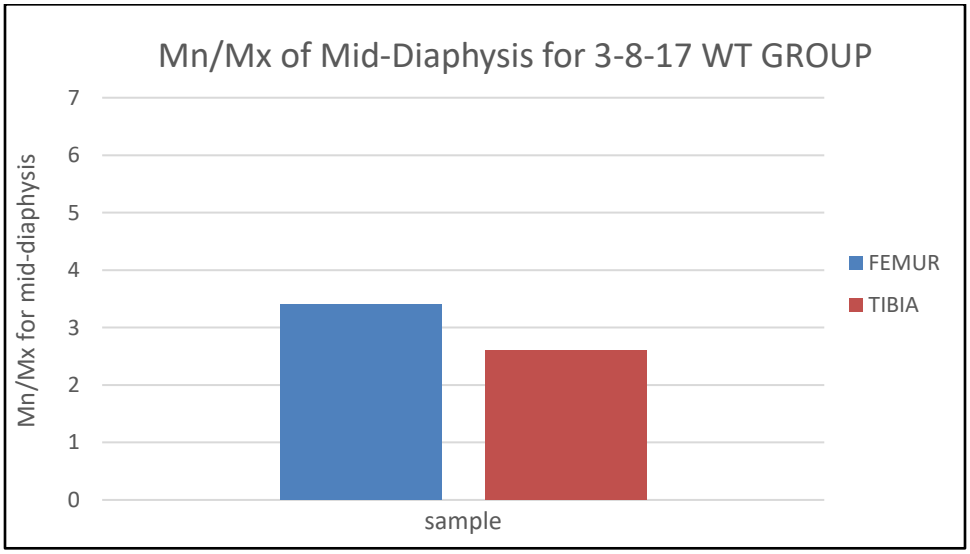

Figure 4-33 Mn/Mx of the femur and tibia on the mid-diaphysis region for the age group 3-8-17 WT

(Where the error bar is missing, there was no variable parameter)

Irrespective of age groups, an average Mn/Mx for all WTs and KOs was calculated, with their standard deviations, separately for the femur and tibia. The mid-diaphysis region resulted in higher Mn/Mx in KO than in WT (Figures 4-34 and 4-35). The means of Mn/Mx were around 3.

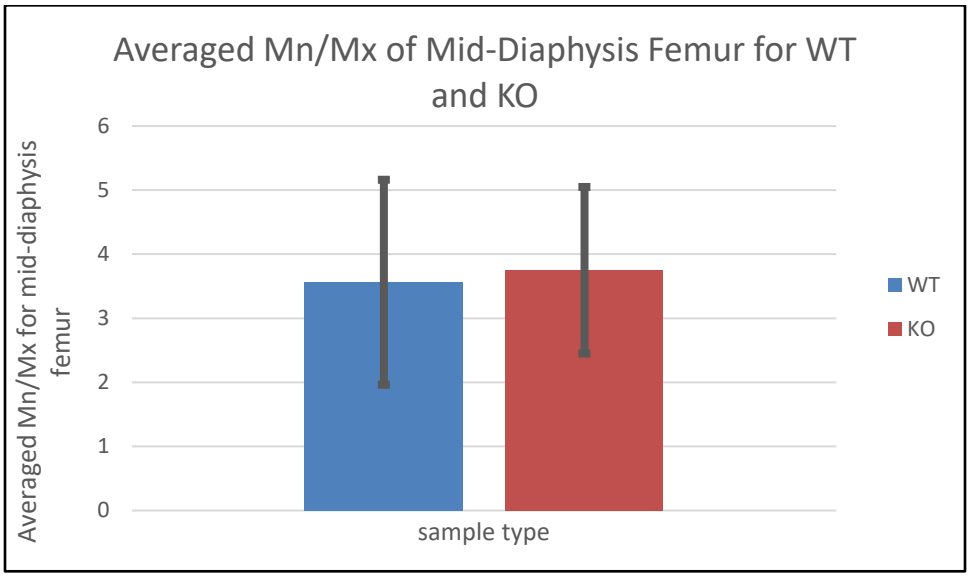

Figure 4-34 Averaged Mn/Mx of the femur on the mid-diaphysis region, error bars represent observations of eight WT and five KO samples

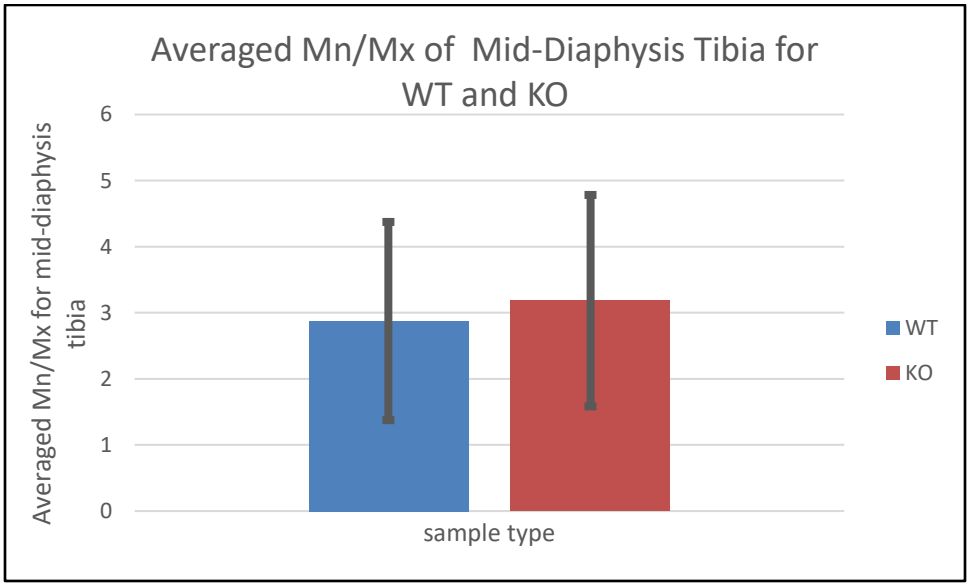

Figure 4-35 Averaged Mn/Mx of the tibia on the mid-diaphysis region, error bars represent observations of eight WT and five KO samples

Without considering the age group, all WT and KO samples' averaged Mn/Mx were compared separately for femur and tibia between (Figure 4-36 and 4-37). Comparison indicated slightly higher Mn/Mx in WT than in KO. The overall average of Mn/Mx was around 3 for both WT and KO samples.

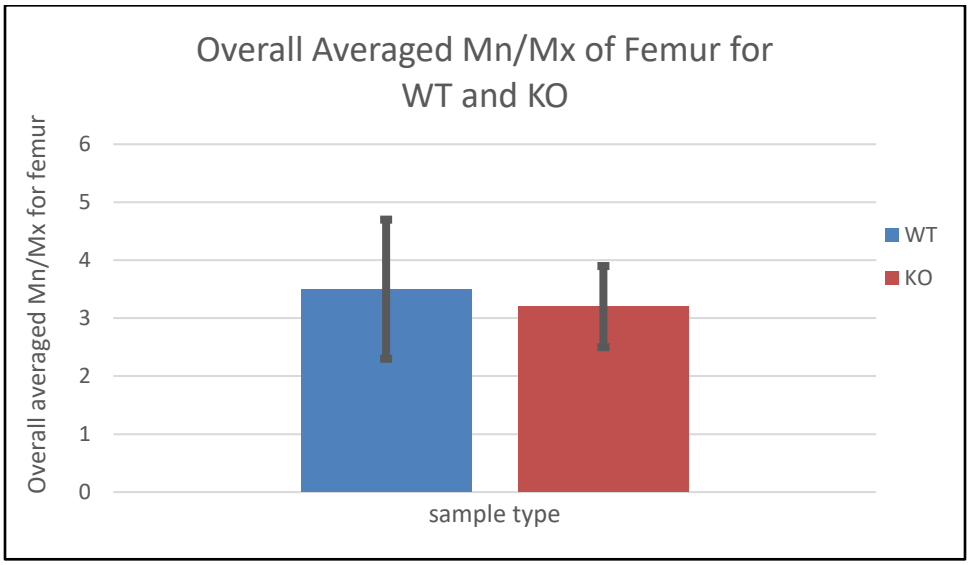

Figure 4-36 Overall averaged Mn/Mx of the femur, error bars represent observations of eight WT and five KO samples

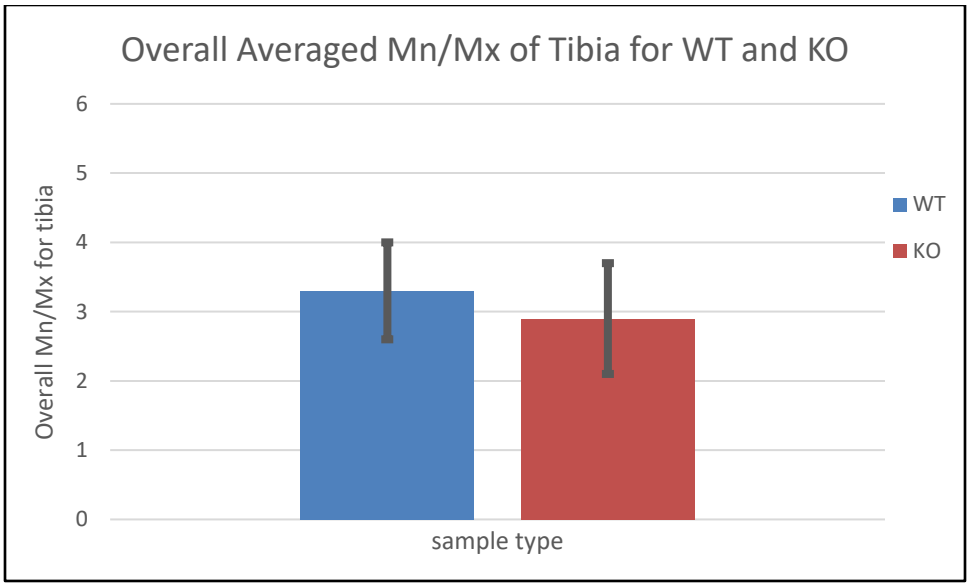

Figure 4-37 Overall averaged Mn/Mx of the tibia, error bars represent observations of eight WT and five KO samples

The area under the phosphate peak was equivalent to mineral content, and the area under the amide I peak represented the quantity of matrix. Phosphate was the primary component of minerals, whereas amide I was the primary component of the matrix.

I implemented different methods for comparisons: position, age group and mid-diaphysis. Comparison of Mn/Mx of mid-diaphysis indicated elevated Mn/Mx in the KO over the WT samples (Figures 4-34 and 4-35). Furthermore, averaged Mn/Mx of WT and KO samples' comparison indicated slightly higher Mn/Mx for the femur and tibia in the WT over the KO. Figures 4-36 and 4-37 illustrate this.

4.2 SEM - Results and Discussion

For the additional insights into FTIR results, we performed Energy Dispersive Spectroscopy with the help of Scanning Electron Microscopy. Initially, we looked for structural changes in the WT and the KO rats. We implemented different techniques, such as high vacuum imaging and low vacuum imaging. Low vacuum imaging helped to determine that coating applied to the sample did not alter the results in high vacuum imaging. Low vacuum imaging, accomplished with the help of BSE, lost resolution at higher magnification. Thus, we were not able to use high magnification in low vacuum. After verifying that coating did not alter mineral and matrix composition, we opted for high vacuum imaging in which SE was used. Since high vacuum imaging requires the sample to be conductive and bone is nonconductive, we coated samples with silver by the sputtering process. However, we did not find structural differences between the WT and KO bones.

4.2.1 X-ray Spectral Mapping

We ran the spectral X-ray mapping to discover the difference in the trabecular and cortical bones (Figure 4-38). With this data acquisition, we could easily identify the boundary between the high mineral (Figures 4-38d and 4-38e) and high matrix regions (Figures 4-38f & 4-38g), along the lateral bone. Furthermore, by mapping significant elements (carbon, oxygen, nitrogen, calcium and phosphorus) on cortical bone, we

determined the qualitative difference between the WT and KO bones (Figures 4-39 and 4-40).

4.2.2 X-ray Mapping of Lateral Bone

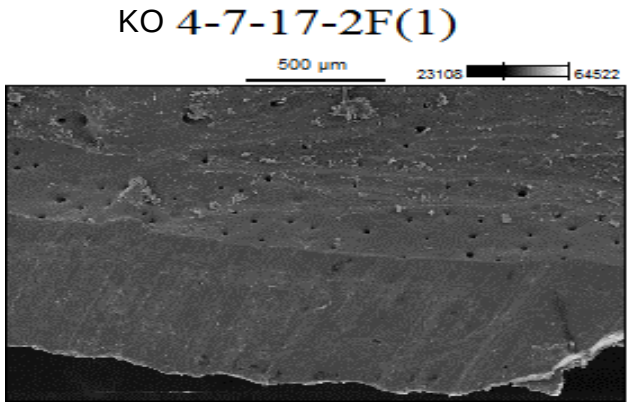

(a)

Data Type:	Counts
Image Resolution:	512 by 384
Image Pixel Size:	4.33 µm
Map Resolution:	256 by 192
Map Pixel Size:	8.65 µm
Acc. Voltage:	25.0 kV
Magnification:	60

(b)

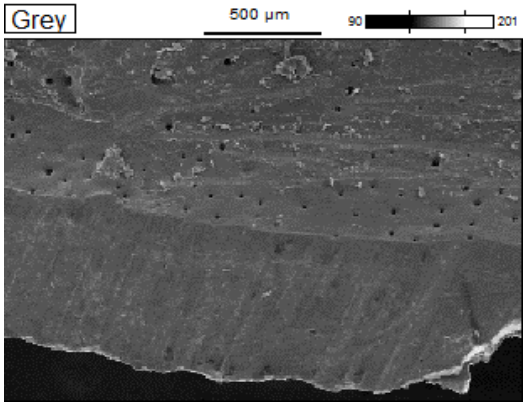

(c)

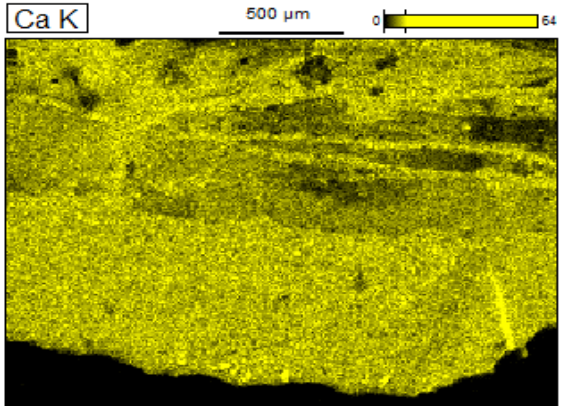

(d)

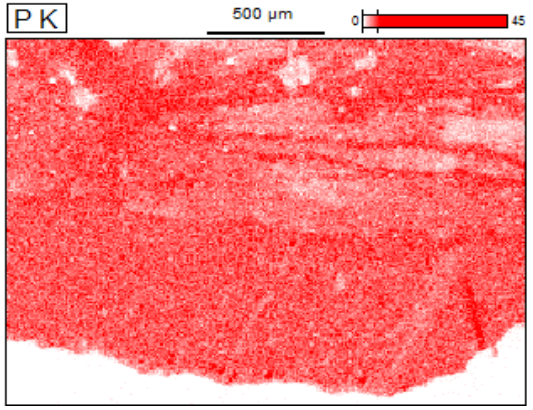

(e)

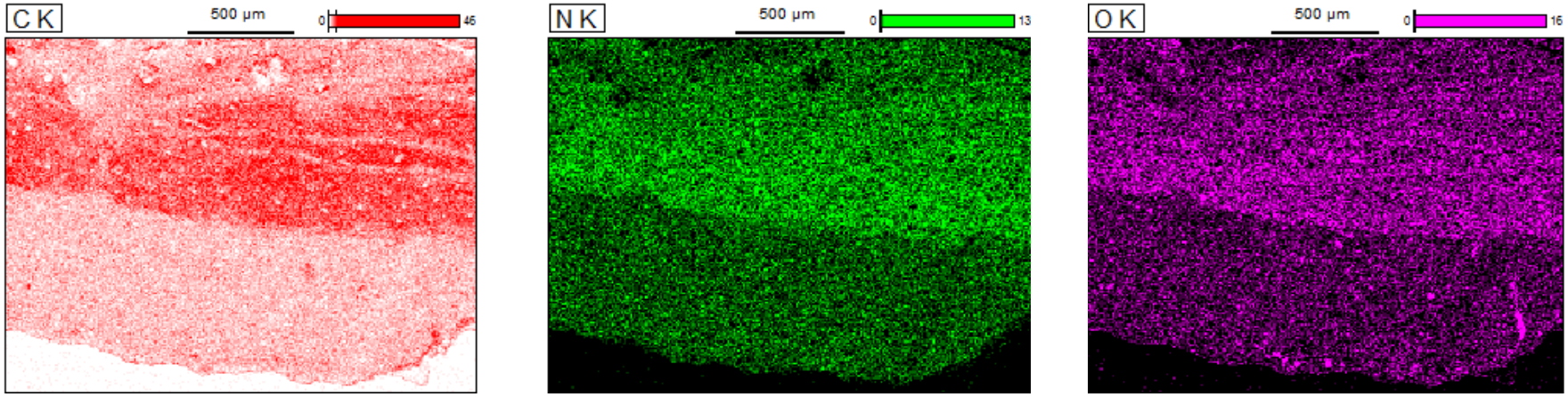

(f) (g) (h)

Figure 4-38 X-ray spectral mapping of lateral bone illustrating a rich region of mineral and matrix components (Figures c, d, e, f, g and h) and examined section (Figure a) with process parameters (Figure b). Note the border between the cortical and trabecular region (lower and upper zone).

4.2.3 X-ray Mapping of WT Cortical Bone

WT

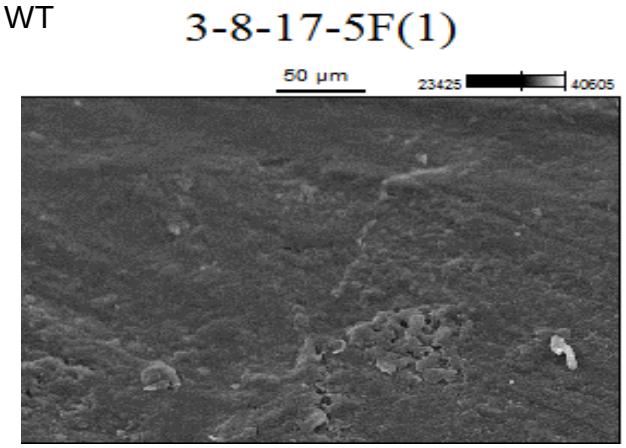

(a)

Data Type: Counts
Image Resolution: 512 by 384
Image Pixel Size: 0.65 µm
Map Resolution: 256 by 192
Map Pixel Size: 1.30 µm
Acc. Voltage: 25.0 kV
Magnification: 400

(b)

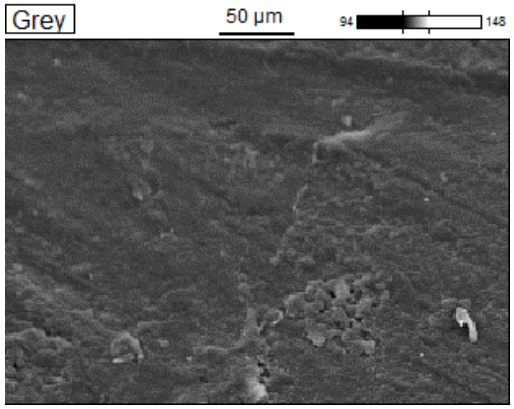

(c)

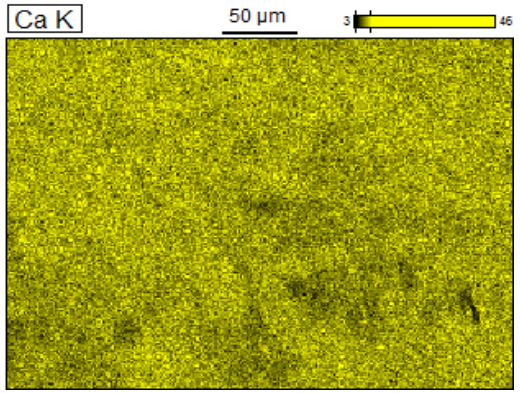

(d)

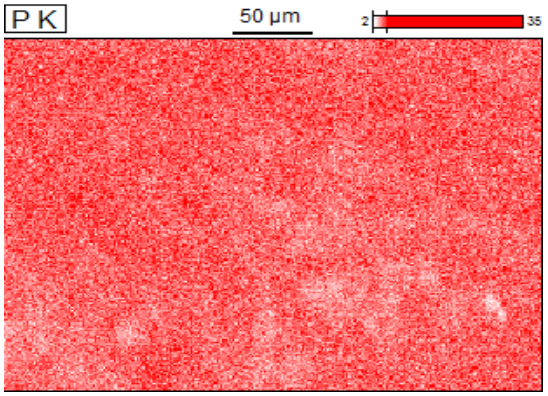

(e)

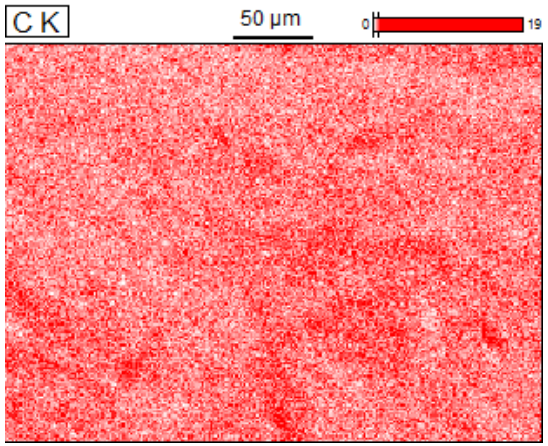

(f)

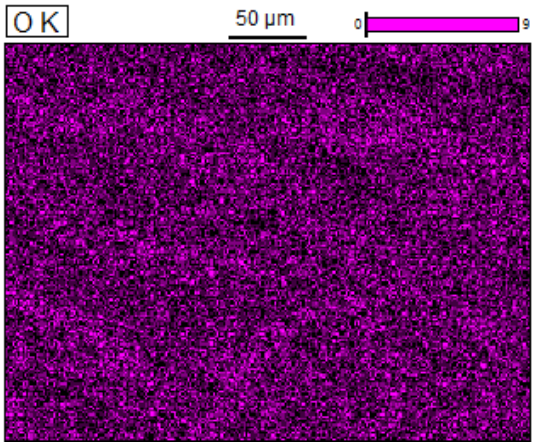

(g)

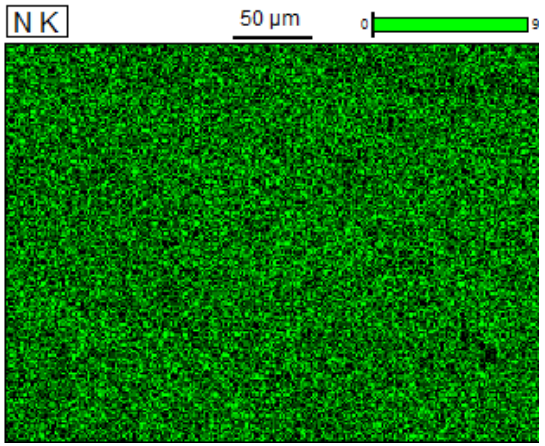

(h)

Figure 4-39 WT X-ray spectral mapping of cortical bone 3-8-17-5F WT illustrating the distribution of different elements (Figures c, d, e, f, g and h) and examined section (Figure a) with process parameters (Figure b)

4.2.4 X-ray Mapping of KO Cortical Bone

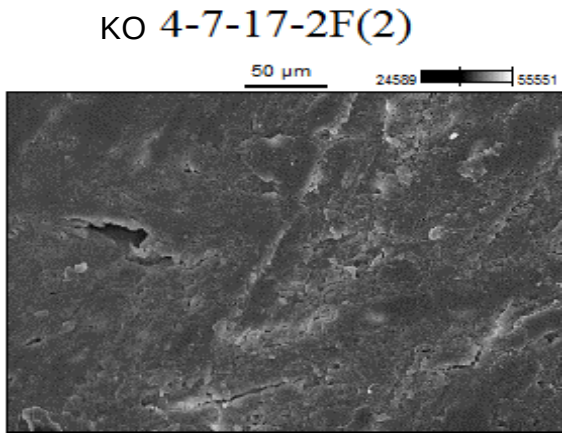

(a)

Data Type: Counts
Image Resolution: 512 by 384
Image Pixel Size: 0.65 µm
Map Resolution: 256 by 192
Map Pixel Size: 1.30 µm
Acc. Voltage: 25.0 kV
Magnification: 400

(b)

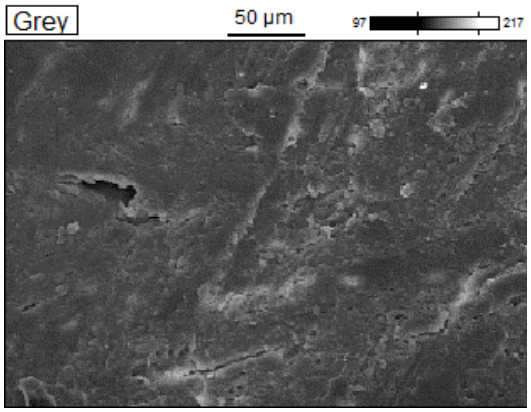

(c)

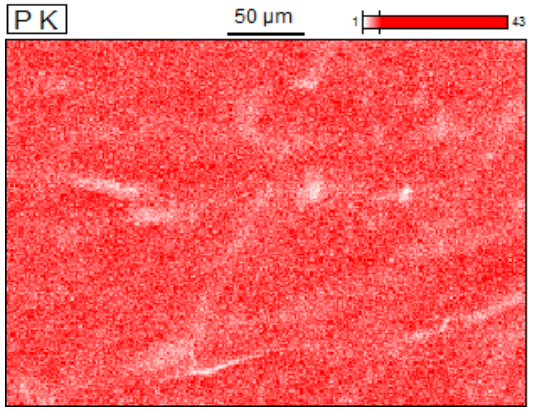

(d)

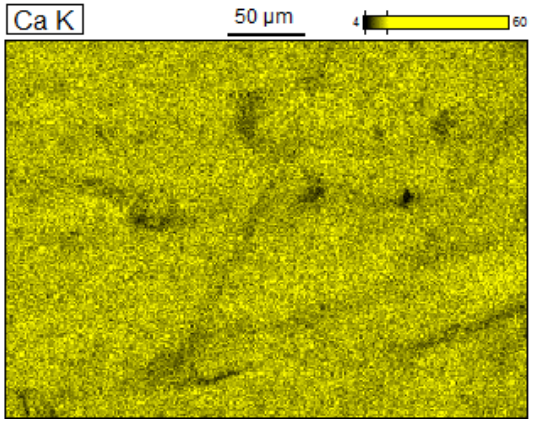

(e)

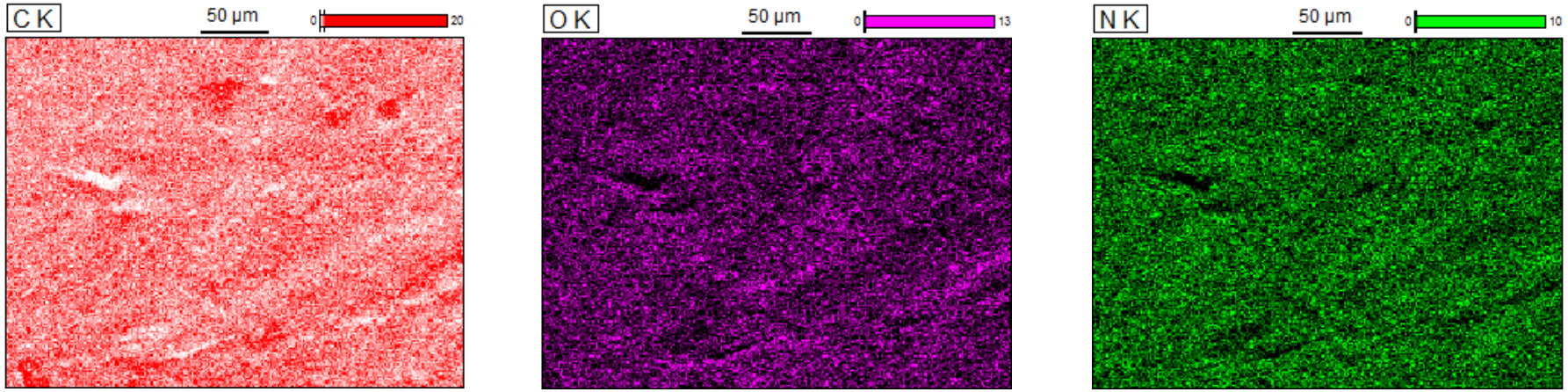

(f) (g) (h)

Figure 4-40 KO X-ray spectral mapping of cortical bone 4-7-17-2FKO illustrating the distribution of different elements (Figures c, d, e, f, g and h) and examined section (Figure a) with process parameters (Figure b)

The difference in the trabecular and cortical bone is apparent. The trabecular section is higher in carbon (Figure 4-38f), whereas the cortical portion is higher in calcium (Figure 4-38d). Furthermore, by the mapping of significant elements (carbon, oxygen, nitrogen, calcium, and phosphorus) on cortical bone, the qualitative difference between the WT and KO become apparent (Figure 4-39 and Figure 4-40). However, this does not give the exact value of variation in the elements for both the types of bone. After running the EDS quantitative results, we found the quantity of components in percentage (Figure 4-41 through Figure 4-44 below). We chose the atomic percentage present in that particular area, which provided the elemental composition with which compound quantity interpretation was indirect. Analyzing the chemical composition of mineral and matrix, we found carbon and oxygen contributed to both mineral and matrix.

Minerals

- Hydroxyapatite - $Ca_5(PO_4)_3(OH)$
- Calcium Carbonate - $CaCO_3$

Matrix

Collagen type I - $(O=C-N)_x$

- Proline ($C_5H_9NO_2$) + Glycine ($C_2H_5NO_2$) + OH^-

Nitrogen primarily represents the amino acids, which are fundamental components of amide I, and contributed 90% of collagen. Minerals were measured by the quantity of hydroxyapatite, which is formed by calcium and phosphorous. Calcium is available in various forms in tissue in addition to the minerals. Calcium is also a part of calcium carbonate. There is a substitution mechanism of calcium involved in crystal reformation. During this substitution mechanism, Si, Zn or Cu ions can replace Ca^{2+} ions, and these calcium ions might be carried away with blood [34]. Therefore, we could not consider calcium as a measure of mineral and carbon and oxygen for matrix measurement. An unusual case observed with the atomic percentage of oxygen. The atomic percentage of oxygen was higher in the KO than in the WT (Figure 4-41).

The cortical bone indicated the amount of nitrogen was higher in the WT than in the KO (Figure 4-41). The comparison denoted matrix content was lower in the KO than in the WT. This trend persisted in the trabecular bone for the WT and KO samples (Figure 4-42).

In a comparison of trabecular with cortical bone for WT and KO, the atomic percentage of carbon and nitrogen were higher in the trabecular than in the cortical, whereas the atomic percentage of oxygen, phosphorous and calcium were higher in the cortical than in the trabecular bone (Figure 4-43 and 4-44).

In general, Mn/Mx being higher in the KO than in the WT supports the FTIR results.

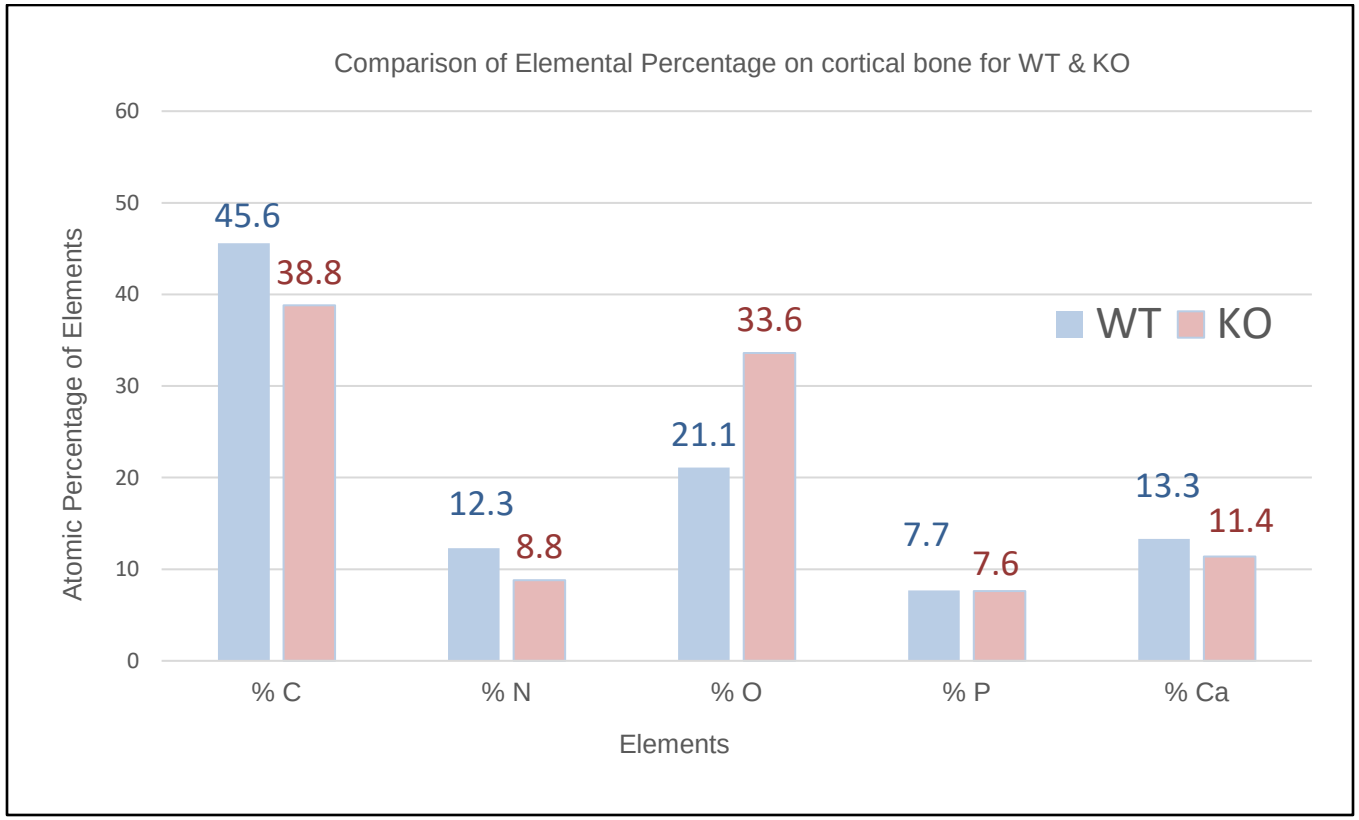

Figure 4-41 Quantitative results from SEM-EDS on the cortical bone for different elements in WT and KO

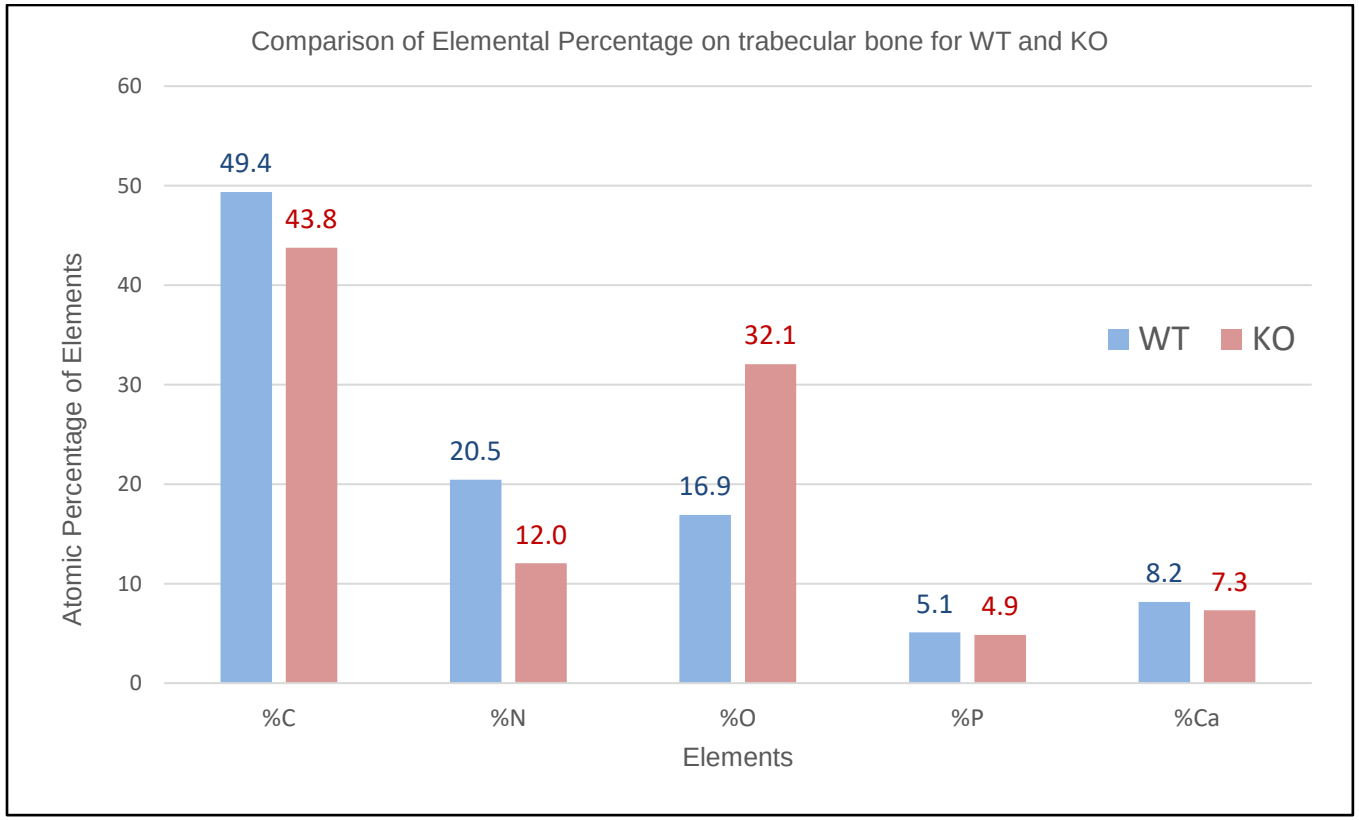

Figure 4-42 Quantitative results from SEM-EDS on the trabecular bone for different elements in WT and KO

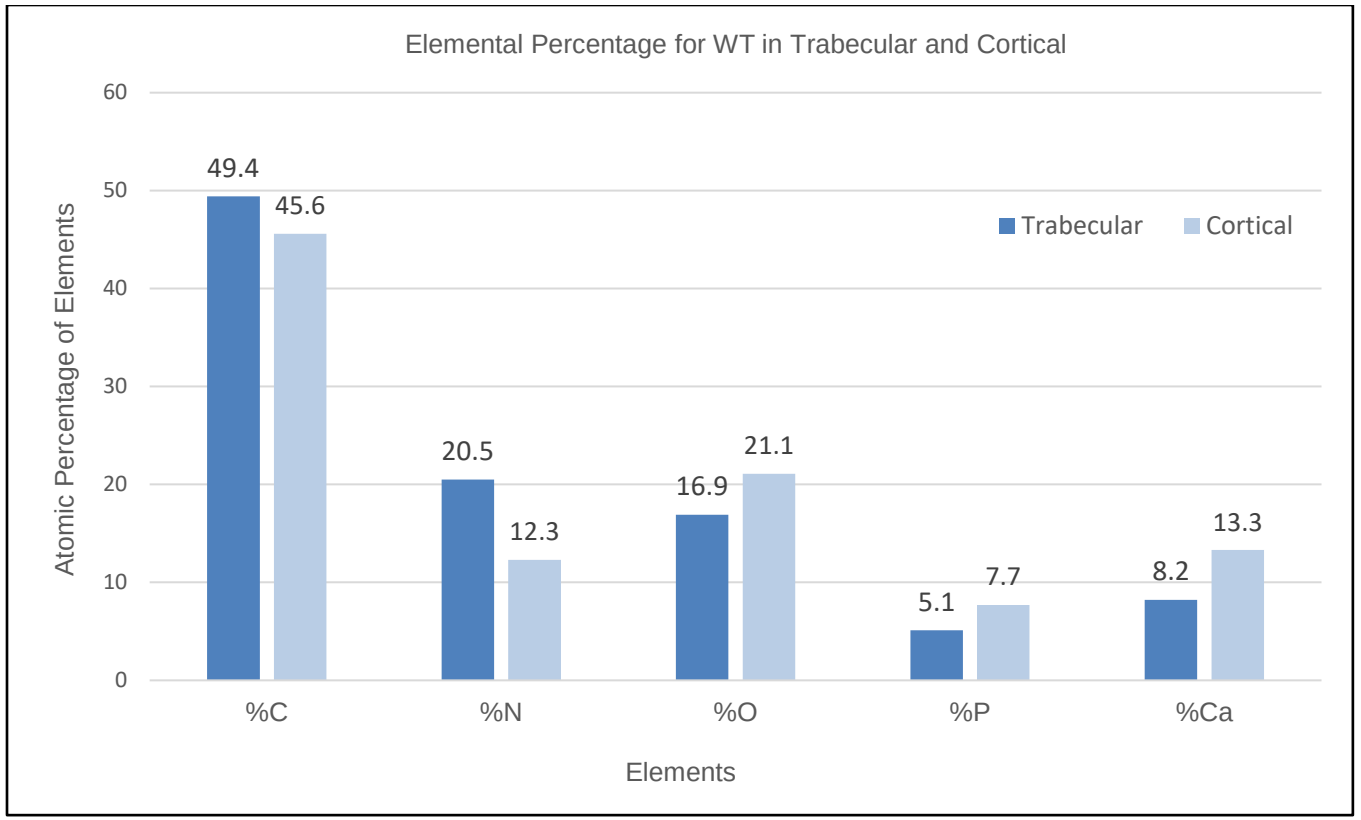

Figure 4-43 Quantitative results from SEM-EDS on the trabecular and cortical bone for different elements in WT

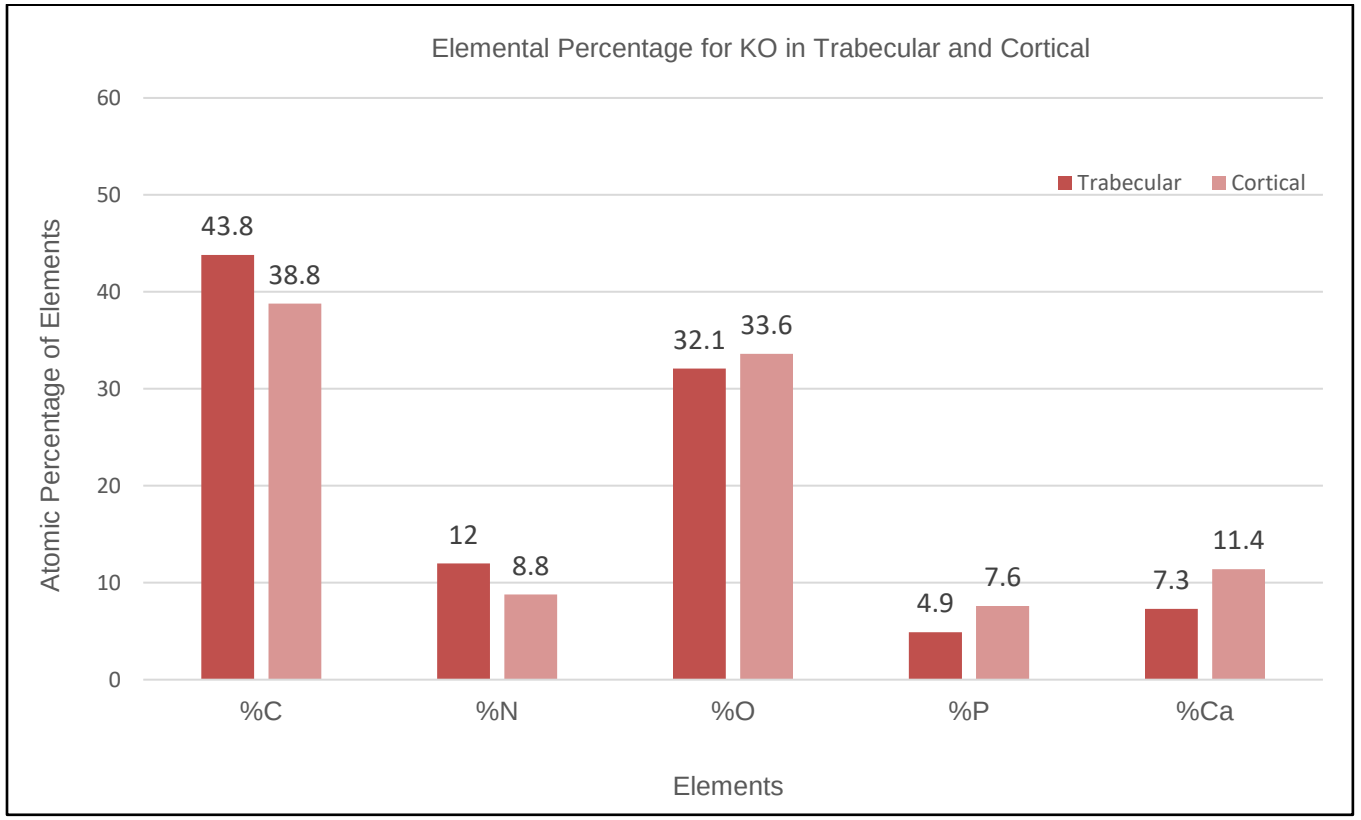

Figure 4-44 Quantitative results from SEM-EDS on the trabecular and cortical bone for different elements in KO

We analyzed WT and KO with FTIR and EDS considering different aspects. Cortical bone indicated the amount of nitrogen was higher in WT than in KO. The comparison denoted the matrix content was lower in KO than in WT. This same trend appeared in the trabecular bone for WT and KO samples. The results indicated that the disabling function of fstl 5 leads to the notable effect on the mid-diaphysis of bone, especially on the tibia. The change involves a greater increased Mn/Mx in KO than in WT.

4.3 Sources of Variations in Spectra

For a single sample, we determined the difference in the spectrum at different locations, which showed the heterogeneity and anisotropic nature of bone. The following parameters can lead to these variations:

1. Sample background: We received samples of different littermates, which could be a reason for the alterations.
2. Age and gender of rat: Development of amino acids, which represents matrix, and hydroxyapatite, which represents mineral, varies with age and gender. Such factors affect the Mn/Mx content we determined for different samples.
3. Crystal age: Mineral morphology changes with the change in crystal age. Crystal reformation is a continuous process. Therefore, depending upon the formation and reformation process, we obtained variable mineral content with FTIR.
4. K-shell: For EDS, we implemented secondary electron imaging, in which we observed the k-shell electrons from the elements and interpreted the results based on the k-shell interactions. This method is not precise with the standard. EDS results change with the sample roughness. A cross-section of the sample is important here, as incident electron intensity would not react equally to every element in the sample [11,35].
5. Sample condition: The sample should be flat enough for both FTIR and SEM. The difference in the quality of polish for different positions and samples could be the reason behind the variation in Mn/Mx.

Chapter 5 Conclusion

If left untreated, TEV can lead to long-lasting disability, malformation, and discomfort. Substantial progress has been achieved in managing and diagnosing the defect, but information about the molecular player and pathways that lead to TEV were unknown before this study.

Fourier Transformed Infrared Spectroscopy is a useful technique to differentiate between the composition of normal and abnormal bone, in this case related to the fstl 5 gene. This technique can also help find pathologies of various diseases and disorders related to the bone, such as Fracture, Osteoporosis, Rickets, Osteomalacia, Osteogenesis imperfecta, Marble bone disease (osteopetrosis), Paget disease of bone and Fibrous dysplasia.

Chapter 6 Future work

6.1 Mechanical Testing

Earlier biomechanical testing was used to determine the possibility of the bone fracture. Fracture testing is achieved by implementing torsion and bending stresses on the bone as these stresses are the main reasons behind fractures. As previously discussed, organic and inorganic constituents concomitantly work while undergoing various stresses.

Tensile and compressive stresses can be implemented and studied as these type of stresses also help to evaluate quality and quantity of bone. The mechanical tester can be used to facilitate tension and compression on the sample. Researchers can measure the force with an attached measuring device.

6.2 XRD

As inorganic part of the bone, hydroxyapatite mineral is crystalline in structure. Therefore, this mineral has specific arrangements of its atoms. If light is incident on these arrayed atoms, that light will reflect from the atom. Such reflected rays either form constructive or destructive interference. The intensity of such light is recorded, and researchers can draw the lattice constant, which is unique for an atom. Researchers can then measure the mineral maturity, which is an essential parameter in evaluating bone strength.

6.3 Skin

Skin is the largest organ of any living organism and consists of several different components, including water, protein, lipids, and various minerals and chemicals. Each element has various functions based on their properties: to protect from infections and other environmental assaults. The skin also contains nerves that sense cold, heat, pain, pressure and touch.

Throughout life, the skin will constantly change, for better or worse. In fact, skin tends to renew itself approximately once a month. Proper skin care is essential for maintaining health and vitality of this protective organ.

The skin is made up of different layers. Layers include a thin outer layer, a thicker middle layer and the inner layer. These layers are called the epidermis, dermis, and hypodermis, respectively. Several methods have been created to analyze the composition of the skin. One is FTIR-ATR. As skin is thin, FTIR-ATR provides the same spectrum whether the epidermis or hypodermis is analyzed. Researches can determine whether there is any co-relationship between bone and skin. They can also observe how this co-relationship varies for WT and KO.

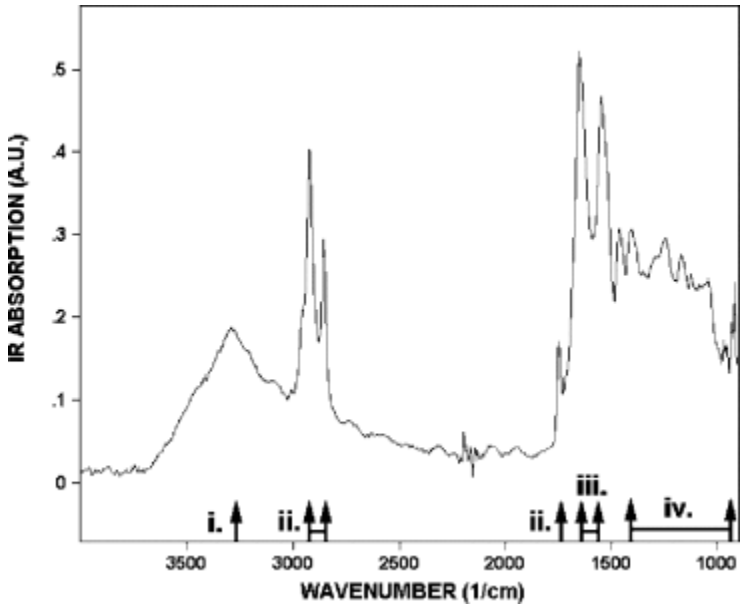

Figure 5-1 Typical FTIR spectrum of human skin

With the help of the reflectance mode, FTIR provides the absorbance spectrum (Figure 5-1). This spectrum illustrates the principle components of skin: (i) water, (ii) lipids, (iii) proteins. Region iv contains information from proteins, lipids, DNA [36] and water and is termed the "fingerprint spectral region."

Table 5-1 The principal absorbing species in the skin in the mid-infrared

Molecular source	Absorption max (cm^{-1})	Physiologic parameter
Water (OH)	3420 (broad), 1640	Stratum corneum hydration
Proteins [amide I, II]	1645, 1545	Stratum corneum proteins
Lipids [CH_3], [CH_2]	[2960, 2870], [2920, 2850]	Stratum corneum lipids
Free fatty acids [C=O]	1710	Sebaceous lipids
Triglycerides	1740, 1460	Sebaceous lipids
Wax esters	1740	Sebaceous lipids

Appendix A

References

1. Rossbach, Hans-Christoph. "Hereditary and familial syndromes of bone and blood. Genetic pathways, diagnostic pitfalls." Fetal and Pediatric Pathology 26.1 (2007): 1-16.
2. Teti, Anna, and Steven L. Teitelbaum. "Congenital disorders of bone and blood." Bone 109 (2018): 78-103.
3. Paschalis, Eleftherios P., Richard Mendelsohn, and Adele L. Boskey. "Infrared assessment of bone quality: a review." Clinical Orthopedics and Related Research® 469.8 (2011): 2170-2178.
4. Kettering, C. F., L. W. Shutts, and Donald H. Andrews. "A representation of the dynamic properties of molecules by mechanical models." Physical Review 36.3 (1930): 531-548.
5. Socrates, George. “Infrared and Raman characteristic group frequencies: tables and charts.” John Wiley & Sons (2001).
6. Larkin, Peter. “Infrared and Raman spectroscopy: principles and spectral interpretation.” Elsevier (2017).
7. Wilson, Edgar Bright, John Courtney Decius, and Paul C. Cross. “Molecular vibrations: the theory of infrared and Raman vibrational spectra.” Courier Corporation (1955).
8. Meier, Rob. "Handbook of Vibrational Spectroscopy: John Chalmers, Peter R. Griffiths, Chichester.” Elsevier (2003): 413-414.
9. “User manual of Optical spectroscopy-FTIR” Bruker Alpha

10. Goldstein, Joseph I. “Scanning electron microscopy and X-ray microanalysis.” Springer, (2017).
11. Sawyer, Linda, David T. Grubb, and Gregory F. Meyers. “Polymer microscopy.” Springer Science & Business Media (2008).
12. Blazewicz, M., and C. Paluszkiewicz. "Characterization of biomaterials used for bone regeneration by FTIR spectroscopy." Journal of Molecular Structure 563 (2001): 147-152.
13. Boyes, Edward D. "High-Resolution and Low-Voltage SEM Imaging and Chemical Microanalysis." Advanced Materials 10.15 (1998): 1277-1280.
14. O’Shea, Ryan M., and Coleen S. Sabatini. "What is new in idiopathic clubfoot?" Current Reviews in Musculoskeletal Medicine 9.4 (2016): 470-477.
15. Moorthi, Ranjani N., et al. "Idiopathic talipes equinovarus (ITEV)(clubfeet) in Texas." American Journal of Medical Genetics Part A 132.4 (2005): 376-380.
16. Basit, Sulman, and Khalid I. Khoshhal. "Genetics of clubfoot; recent progress and future perspectives." European Journal of Medical Genetics 61.2 (2017): 107-113.
17. Grzeschik, Karl-Heinz. "Human limb malformations; an approach to the molecular basis of development." International Journal of Developmental Biology 46.7 (2004): 983-991.
18. Suzuki, Dai, Atsushi Yamada, and Ryutaro Kamijo. "The essential roles of the small GTPase Rac1 in limb development." Journal of Oral Biosciences 55.3 (2013): 116-121.
19. Pflugfelder, G. O., F. Eichinger, and J. Shen. "T-Box Genes in Drosophila Limb Development." Current Topics in Developmental Biology 122 (2017): 313-354.

20. Pickering, Joseph, and Matthew Towers. "Inhibition of signaling in the chick wing gives insights into digit patterning and evolution." Development 143.19 (2016): 3514-3521.

21. Lopez-Rios, Javier. "The many lives of SHH in limb development and evolution." Seminars in Cell & Developmental Biology 49 (2016): 116-124

22. Ornitz, David M., and Pierre J. Marie. "Fibroblast growth factor signaling in skeletal development and disease." Genes & Development 29.14 (2015): 1463-1486.

23. Narayana, Jyoti, and William A. Horton. "FGFR3 biology and skeletal disease." Connective Tissue Research 56.6 (2015): 427-433.

24. Lewandowski, Jordan P., et al. "Spatiotemporal regulation of GLI target genes in the mammalian limb bud." Developmental Biology 406.1 (2015): 92-103.

25. Akiyama, Ryutaro, et al. "Sall4-Gli3 system in early limb progenitors is essential for the development of limb skeletal elements." Proceedings of the National Academy of Sciences 112.16 (2015): 5075-5080.

26. Cunningham, Thomas J., and Gregg Duester. "Mechanisms of retinoic acid signaling and its roles in organ and limb development." Nature Reviews Molecular Cell Biology 16.2 (2015): 110-123.

27. Teven, Chad M., et al. "Fibroblast growth factor (FGF) signaling in development and skeletal diseases." Genes & Diseases 1.2 (2014): 199-213.

28. Neben, Cynthia L., and Amy E. Merrill. "Signaling pathways in craniofacial development: insights from rare skeletal disorders." Current Topics in Developmental Biology 115 (2015): 493-542.

29. Chen, Chong. "Skeleton Genetics: a comprehensive database for genes and mutations related to genetic skeletal disorders." Database 2016 (2016).

30. Allen, Justin M. "Autopodial development is selectively impaired by mis-expression of chordin-like 1 in the chick limb." Developmental biology 381.1 (2013): 159-169.

31. Nelson, Matthew R., et al. "The support of human genetic evidence for approved drug indications." Nature Genetics 47.8 (2015): 856-860.

32. Altshuler, David, Mark J. Daly, and Eric S. Lander. "Genetic mapping in human disease." Science 322.5903 (2008): 881-888.

33. Porcu, Eleonora. "Genotype imputation in Genome-Wide association studies." Current Protocols in Human Genetics (2013): 1-25.

34. Smith, E. L. "Principals of Biochemistry: General Aspects and Mammalian Biochemistry." New York: McGraw-Hill (1983).

35. Fernández-Varea, J. M., X. Llovet, and F. Salvat. "Cross sections for electron interactions in condensed matter." Surface and Interface Analysis 37.11 (2005): 824-832.

36. Kollias, Nikiforos, and Georgios N. Stamatas. "Optical non-invasive approaches to diagnosis of skin diseases." Journal of Investigative Dermatology Symposium Proceedings 7.1 (2002): 64-75.

Biographical Information

Sunil Yadav is a master's student of Materials Science and Engineering at the University of Texas at Arlington. He completed his bachelor's from the University of Pune, India, in Mechanical Engineering. He is a co-author of two publications on vortex tubes, which are based on his studies during his bachelor's. Projects he worked on cover topics such as characterization, failure analysis and reliability engineering. During his master's tenure, he was a Treasurer of American Society of Materials at the UTA Chapter, and he wants to join the industry upon completion of his master's.